UC Berkeley
UC Berkeley Electronic Theses and Dissertations

Title
Noise sensing and quantum simulation with trapped atomic ions

Permalink
https://escholarship.org/uc/item/2tj4v94m

Author
Gorman, Dylan J

Publication Date
2017

Peer reviewed|Thesis/dissertation

Noise sensing and quantum simulation with trapped atomic ions

by

Dylan J Gorman

A dissertation submitted in partial satisfaction of the

requirements for the degree of

Doctor of Philosophy

in

Physics

in the

Graduate Division

of the

University of California, Berkeley

Committee in charge:

Professor Hartmut Häffner, Chair
Professor K. Birgitta Whaley
Professor Irfan Siddiqi

Spring 2017

Noise sensing and quantum simulation with trapped atomic ions

Abstract

Noise sensing and quantum simulation with trapped atomic ions

by

Dylan J Gorman

Doctor of Philosophy in Physics

University of California, Berkeley

Professor Hartmut Häffner, Chair

In this work, we present a novel method to couple any two vibrational modes of a single trapped ion, allowing energy to be swapped between the two modes. We use the scheme to perform ground state cooling and heating rate measurements of vibrational modes without direct optical access. This lessens experimental design constraints in trapped ion experiments, particularly in surface trap apparatus where optical access can be difficult.

We use a single ion as an electric-field noise sensor to study noise processes originating on the metallic surfaces of microfabricated ion traps. We show that realistic models of surface noise predict a specific polarization of the electric-field fluctuations relative to the trap geometry. In contrast, technical noise sources predict a different polarization direction and magnitude which can be inferred by electrostatic simulation of the trapping electrodes. We show that, by comparing heating rates of the two radial modes of a single trapped ion, one can determine whether technical noise sources are a significant contribution to heating. This is an important test for experiments aimed at studying surface noise effects. We also study dephasing due to surface noise, in which the electric potential curvature due to surface noise sources disturbs the phase of the ion motion. We measure the dephasing time for trapped ion motion. Using a noise model featuring dipolar noise sources, we probe the power spectrum of surface noise effects. These measurements, especially if repeated in a trap with smaller ion-electrode distances, may yield new insights as to the physical origin of surface noise effects.

We demonstrate a two-ion quantum simulation of vibrationally-assisted energy transfer, an important phenomenon in biochemical energy transfer. We show that the quantum simulator performs well when benchmarked against exact numerical simulation. We believe that our approach can be scaled to more complicated systems beyond the reach of classical simulation, and discuss several methods for extending the simulation.

To my parents, who taught me to always be curious.
And to Nikko, who taught me to always chew on the furniture.

Acknowledgments

Successfully completing my seven-year graduate career would not have been possible without a lot of help from a lot of people. Firstly, I need to thank my parents, whose unfailing support helped me through community college, my undergrad years at Berkeley, and finally through grad school. I am also immensely grateful to Amanda Kay, who was a constant source of encouragement through all of the struggles and successes over these past years.

I am particularly indebted to my advisor, Hartmut Häffner, who taught me how to be a physicist. He listened patiently to my crazy ideas about physics, and gave me the freedom to pursue the experimental paths I wanted.

During my undergrad time, I was part of the UC LEADS program, which funded my research for two summers. A special thanks is due to Diana Lizarraga, who ran the program and helped me immensely when applying to graduate school. In this research, I worked with Kevin Young, who taught me a lot about how to do research.

I was fortunate to be surrounded by an incredibly talented team of students and postdocs throughout my time in the lab. I learned my first lab skills from Sankar Narayanan and Soenke Moeller, who both helped me anytime I asked. A special thanks is also due to postdocs Nikos Daniilidis and Philipp Schindler, who mentored me. I worked closely with undergraduate students Ross Hutson and Matthew McAllister, who each made important contributions to the experiments. Ross helped develop the dc electronics systems for the surface trap experiments, and Matthew implemented pulse shaping for our frequency sources. More recently, I have worked directly with Boerge Hemmerling, Eli Megidish, and Joe Broz, who have been great lab partners and friends. I also thank the many other lab members who helped me in countless ways– Erik, Crystal, Ahmed, Hong, Mike, Omid, Maya, Clemens, and Chi Chi.

Thanks for everything to Jon Ouellet, who was a great friend, roommate, and co-GSI during the first few years of my program. Finally, thanks to Anthony Ransford, for the many adventures, and for helping me stay somewhat sane.

Contents

List of Figures

List of Tables

Chapter 1

Introduction

In many respects, trapped-ion experiments are a unique playground for exploring nearly idealized quantum experiments. As we shall see throughout this work, a single trapped ion can often be thought of as a two-level spin attached to a three-dimensional harmonic oscillator. In this description, the two-level system models the electronic structure of the ion, and the harmonic oscillator describes the motion.

As is often the case in research, my experimental work did not follow a precisely linear path. Results from three different experimental setups are presented in this thesis.

My research began as an effort to build so-called "hybrid quantum systems" with trapped ions. In 1990, Heinzen and Wineland [26] pointed out that a trapped, oscillating charged particle ought to induce electrical currents in nearby electrodes. Those ideas lead rather directly to the experimental proposal by Daniilidis and co-authors [14] to use the induced currents as an ion-ion coupling mechanism. The idea behind this experiment is to trap an ion at each end of a metal wire. As one trapped ion oscillates, it should induce a current in the wire which can in principle be detected by an ion at the other end. This can lead, for instance, to exchanging single vibrational quanta between the two trapped-ion oscillators. This ion-wire-ion system would be a first step towards building hybrid quantum devices such as ions coupled to superconducting qubits. Such hybrid devices may be useful in the quest for scalable quantum computing. The experiment is quite technically challenging, however, as it requires ions to trapped within 50 μm of the wire in order to for state exchange to occur with a few milliseconds. The first results in this thesis were inspired by thinking about these technical challenges.

In the first iteration of that experiment, the ions were trapped in a fairly standard surface electrode RF Paul trap. A small 1 mm length wire was glued to an aluminum frame. The frame itself was attached to a set of piezo stages so that it could positioned near two ions to perform an ion-ion coupling exepriment. While working with that setup, the wire broke off the holder inside the vacuum chamber. We decided at that point to re-design the experiment in a more robust way. We formulated a new microfabricated trap design in which the coupling wire was actually fabricated onto the surface of the trap. This re-design has been completed, and initial trapping was recently successful.

While re-designing the wire experiment, we started thinking about using chains of trapped ions to study the quantum mechanics of energy transfer. Through a conversation with a theory collaborator, Mohan Sarovar, we came up with the idea to implement vibrationally assisted energy transfer (VAET) in a two-ion system. VAET is a phenomenon believed to be important in biochemical processes such as photosynthesis, in which the transfer of electronic excitation is enhanced by the presence of a bosonic environment provided by molecular vibrations. In a trapped ion system, we emulated a model of this process. In our emulation, the electronic state of the two-ion system corresponds to chemical energy, and vibrational modes of the ion chain serve as the environment. We believe that this is the first direct, isolated observation of vibrationally assisted energy transfer.

This thesis is organized as follows. In **Chapter 2**, I discuss the basics of the radio-frequency Paul trap, the workhorse tool of ion trapping experiments. In **Chapter 3**, I give an overview of the light-matter interactions which are necessary to undersatand the experiments in this thesis. **Chapter 4** discusses the experimental setup of the wire coupling experiment.

In **Chapter 5**, I present the first experimental results of this thesis. In this Chapter, I discuss a novel parametric method for swapping energy between any two vibrational modes of a single-ion oscillator. This idea was originally developed to ease experimental design constraints in the wire coupling experiment. Briefly, the vibrational modes of the trapped ions which couple most strongly to the wire tend to be the hardest to interrogate via standard laser-ion methods. This is because the vibrational mode which couples most strongly to the wire is one which involves the ion moving normally to the surface the wire. The wire then tends to block a laser beam which would have a wave-vector projection onto the ion's motion along this axis. However, in order to verify that coupling is in fact occuring, one must monitor the energy flow into the oscillator modes. Therefore, we developed a scheme to swap the energy between oscillator modes, so that the wire coupling can be detected by interrogating a mode with better optical access. We also showed that this technique can be used to laser-cool vibrational modes which have no overlap to the cooling laser wave-vector. This method could then be used to cool all three vibrational modes of a trapped ion given any laser orientation, lessening experimental design constraints considerably.

In **Chapter 6**, two experiments pertaining to surface noise are covered. I give a brief overview of how noisy electric fields disturb the motional state of trapped ions. It has been known for some time that noise arising from the metal surfaces of ion traps can be a dominant decoherence source when ions are trapped of order 100 μm from the surface. This effect must therefore be properly accounted for when performing the wire-coupling experiment. While the specific mechanism of this noise is unknown and may vary from experiment to experiment, I present a simple phenomenological model which should hold in many cases. We study the directional dependence of electric field noise in ion traps and point out that the electric field fluctuations can be larger in the direction normal to the trap surface than parallel to it. By using a single ion as direction-sensitive noise sensor, we are able to measure the direction in which the noise is the largest and moreover we use this effect to determine whether the noise originates from material properties on the trap surface or from

technical sources such as noisy voltage supplies. Finally, in this Chapter, I discuss another experiment in which we measured the degree to which surface noise effects perturb the phase coherence of the ion motion. This arises from the curvature of the potential induced by the noise sources, perturbing the ion motional frequencies. We point out that this effect will become important as ion traps are further miniaturized. We also use this effect to try to determine the frequency spectrum of the surface noise sources which may give hints about their physical origin.

Finally, **Chapter 7** discusses our work on quantum-scale energy transfer. We engineer vibrationally assisted energy transfer in an analog quantum simulator, and the transfer dynamics in different regimes of the model. I also discuss prospects for scaling the simulation to more complicated models, potentially to a regime which cannot be accessed by classical simulation resources.

Chapter 2

Ion traps

The experiments described in this document take place in different traps. Most of the results are obtained using a micro-fabricated surface electrode Paul trap. The final chapter of results are obtained in a more classic three-dimensional rf Paul trap. Nevertheless, the underlying principle of operation is exactly the same in both cases.

2.1   Radio-frequency Paul traps

The first radio-frequency (rf) Paul trap for charged particles was realized in 1954 [48]. The mechanism relies on the creation of a rapidly oscillating electric potential with a saddle point somewhere in space. For a concrete picture, see Fig. 2.1. At the location of the saddle, the instantaneous electric field is always zero since the potential gradient is zero. However, away from the saddle point, the electric field amplitude increases as the distance from the saddle. Under certain conditions discussed below, this situation can give rise to stable trapping of a charged particle, in which the particle is drawn to the saddle. Given these conditions, the oscillating potential can be modeled as a time-independent harmonic pseudo-potential–an approximation we will use throughout this work. In what follows, I will develop the classical equations of motion for a charged particle near such a potential saddle point. It is in fact possible to solve the dynamics in a fully quantum-mechanical way [43], but this treatment is considerably more complicated and does not seem to yield any new intuition.

To obtain the classical equation of motion for a charged particle of mass m and charge Q in an rf Paul trap, we will follow the treatment given by [6]. First, we will assume an electrode geometry such as that sketched in Fig. 2.1, where the electrodes labeled V_{RF} have the time-varying voltage $V_0 \cos(\Omega_{\mathrm{rf}} t)$. In addition we will allow for some additional electrodes which can apply any dc potential satisfying Laplace's equation. We will take the $\hat{z}$ direction to be into the page and assume the rf electrodes extend far enough in this direction that the electric field due to these electrodes is only in the xy-plane. We will call the $\hat{z}$ direction the "trap axis." Finally, we will assume that the potential oscillates much more slowly than the light travel time between electrodes, so that we can solve the problem quasi-statically (i.e.

(a)   (b)
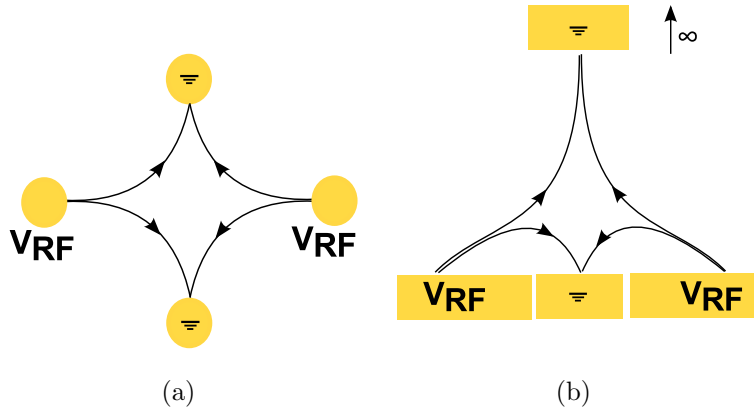
Figure 2.1: Schematic cross-sections of typical rf Paul trap designs. Gold sections represent electrodes which are assumed to extend into the page. (a) Classic 3D Paul trap. (b) Surface-electrode trap. V_{RF} represents a sinusoidally oscillating voltage at radio-frequency $(30 - 50$ MHz, typically). The arrows sketch the electric field lines at the positive phase of the rf cycle. In both cases, there is a point where the electric field is zero, and charged particles may be trapped in this region. In (b), the grounded electrode at infinity does not actually exist, but is used to demonstrate the boundary condition that the electric potential is zero at infinity. Due to symmetry, the rf field provides no confinement in the direction normal to the page. To achieve confinement in this direction, additional dc electrodes are introduced which create a confinement in this direction.

by neglecting radiation). Then for some orientation of the $\hat{x}$ and $\hat{y}$ axes, the instantaneous electric potential near the saddle point due to the rf electrodes is

$$\Phi_{\mathrm{rf}} = \frac{V_0}{2}\left(1 + \frac{x^2 - y^2}{\ell^2}\right)\cos(\Omega_{\mathrm{rf}}t), \tag{2.1}$$

where ℓ is a characteristic length scale of the trap geometry and we have taken the point $(0,0,0)$ to be the location of the saddle point. In addition, we allow for some dc potential $U(x, y, z)$, such that the total electric potential is

$$\Phi(x, y, z, t) = U(x, y, z) + \frac{V_0}{2}\left(1 + \frac{x^2 - y^2}{\ell^2}\right)\cos(\Omega_{\mathrm{rf}}t). \tag{2.2}$$

This potential creates the field

$$\mathbf{E}(x, y, z, t) = -V_0\left(\frac{x\hat{x} - y\hat{y}}{\ell^2}\right)\cos(\Omega_{\mathrm{rf}}t) + \mathbf{E}_{\mathrm{dc}}. \tag{2.3}$$

Since we have already supposed that we can create arbitrary dc potentials, we will choose $\mathbf{E}_{\mathrm{dc}}(0,0,0) = 0$. i.e. we will assume that the saddle points of the rf and dc potentials coincide.

If this is the case, then to lowest order, $\mathbf{E}_{dc}$ varies quadratically around $(0,0,0)$. It will be convenient then to write ($\mathbf{u} = u_x\hat{x} + u_y\hat{y} + u_z\hat{z}$):

$$E_{dc,i} = \frac{m}{Q}(\omega_i^{dc})^2 u_i. \tag{2.4}$$

Here we have just re-written the dc electric field in terms of the frequency a charge would oscillate in a potential of that curvature.

The equation of motion for the charged particle is then:

$$m\ddot{u}_i = QE_i, \tag{2.5}$$

$$\ddot{u}_i + (a_i + 2q_i\cos(\Omega_{rf}t))\frac{\Omega_{rf}^2}{4}u_i = 0. \tag{2.6}$$

The last line is the canonical form of the Mathieu equation, with

$$a_i = \frac{4(\omega_i^{dc})^2}{\Omega_{rf}^2}$$

$$q_x = -q_y = \frac{2QV_0}{m\ell^2\Omega_{rf}^2}$$

$$q_z = 0.$$

If $|q_i|$ and $|a_i|$ are both $\ll 1$, the solution to the Mathieu equation takes the form:

$$u_i(t) \approx A_i\cos(\omega_i t + \phi_i)\left(1 + \frac{q_i}{2}\cos(\Omega_{rf}^2)\right), \tag{2.7}$$

with $\omega_i \approx \frac{1}{2}\Omega_{rf}\sqrt{a_i + \frac{1}{2}q_i^2}$.

It is worth considering what this equation is telling us. The first thing this is telling us is that the equation of motion is the same as that of a particle harmonically trapped with secular frequency ω_i. On top of that harmonic motion, there is a small amplitude of driven motion at the frequency of the rf drive. This driven motion is called "micromotion" throughout the literature. This micromotion results from the charge's oscillations around the potential minimum, during which it experiences regions of non-zero rf field. The rf field generates a periodic force with frequency Ω_{rf}, imposing micromotion on top of slower secular trajectory.

The second thing to notice is the form of ω_i. If we take, for instance, the x direction, and write it out explicitly, we find

$$\omega_i \approx \sqrt{(\omega_x^{dc})^2 + \frac{\Omega_{rf}^2}{8}q_x^2}. \tag{2.8}$$

We therefore find that the equation of motion is approximately equal to the equation of motion if a charge is placed in a dc field with frequency ω_i^{dc}, and the rf field is replaced with

a harmonic pseudopotential of frequency $\Omega_{\mathrm{rf}} q_x / \sqrt{8}$. This is known as the pseudopotential approximation, and throughout most of the rest of this work we will treat the effect of the rf potential as a static pseudopotential.

A single trapped ion will have three normal modes of oscillation. In a linear trap geometry (shown in Fig. 2.1), two modes will lie in the plane of the rf confinement, and it is standard to refer to these modes as "radial modes." The third direction is called the "axial mode."

2.2 Static potential control

For several reasons, it is important to control the dc fields near the trapping location. One reason is that, since the trap geometries we consider will have no rf confinement along the $\hat{z}$ direction, we need to apply a dc potential which confines a charge in this direction. Laplace's equation requires that if the dc field is confining along $\hat{z}$ it must be anti-confining along at least one other axis. However, the combination of dc potential plus rf pseudopotential can still be confining in all three spatial axes as long as the pseudopotential curvature is strong enough in the anti-confining directions.

It is also important to cancel stray dc fields which may exist in the trapping region due, for instance, to nearby charged dielectric materials. If the dc field is not zero at precisely the same location as the saddle point of the rf field, the combination of dc potential and pseudopotential will move the trapping location out of the zero point of the rf field. While this is tolerable to some degree (and in fact unavoidable at some level), this means that the trapped charge experiences a driving force due to the rf field, modulating the ion's motion at the driving rf frequency. This effect is called "excess micromotion"–micromotion in excess of the unavoidable modulation experienced if the rf and dc fields are perfectly aligned. Among other problems, such driven motion can create difficulties in laser cooling if the modulation amplitude becomes comparable to the laser wavelength.

In addition, it can also be useful to use dc potentials to tune the orientation of the trapped charge's harmonic oscillator modes with respect to the trap structure. We applied such control in Sec. 6.3 to study electric field noise originating from trap electrode surfaces.

By placing and biasing electrodes near the trapping region, the dc potential near the trapping region can be manipulated. However, it is not immediately clear how to generate a particular potential landscape given some configuration of controllable electrodes. We need a means to deterministically modify the potential in the trapping region. A thorough formal treatment of dc potential control in ion traps is found in [44]. Here, I will give an overview of the topic in less formal terms.

We need only to control the potential in a very small region around the rf saddle point, and therefore we will therefore attempt to control the coefficients of a series expansion around this point. Neglecting a constant offset, a general function defined in three dimensions will have 9 independent parameters up to second order in spatial variation. An electric potential, however, must obey Laplace's equation ($\nabla^2 \Phi = 0$), and so we expect 8 independent degrees of freedom.

The independent degrees of freedom will be the projections of the potential along some set of basis functions (which are up to second order in space). The basis elements we seek are functions $f(x, y, z)$ satisfying $\nabla^2 f = 0$–i.e. eigenfunctions of the Laplacian with eigenvalue zero. This guarantees that superpositions of the basis functions also satisfy the Laplace equation. One convenient set of basis functions satisfying this constraint is the real spherical harmonics [44] (real because electric potentials must be real). For our experiments, we will define basis functions as:

$$
\begin{aligned}
E_x &= & x \\
E_y &= & y \\
E_z &= & z \\
U_1 &= & \frac{x^2 - y^2}{2} \\
U_2 &= & \frac{2z^2 - x^2 - y^2}{2} \\
U_3 &= & \frac{xy}{2} \\
U_4 &= & \frac{xz}{2} \\
U_5 &= & \frac{yz}{2}
\end{aligned}
\tag{2.9}
$$

These basis functions are called "multipoles." The E_i terms are of linear order in space and therefore represent homogeneous electric fields. The U_i terms are electric quadrupoles, modifying the curvature of the potential in the trapping region. To the current order of approximation, any potential landscape can be expressed as a linear combination of these multipoles. With complete control over these multipoles, it is possible to completely control the electric field and potential curvature in the trapping region (subject to the stability of the Mathieu equation, but this is not typically a problem).

In order to control the potential using some set of electrodes E^i, one needs to know the potential due to each electrode, with all other electrodes grounded. This can be obtained either by electrostatic simulation or some analytic approximation [63, 70]. The potential Φ^i due to biasing E^i to voltage V^i can be written

$$
\Phi^i(x, y, z) = V^i \left(\frac{e_x^i}{r_0} E_x + \frac{e_y^i}{r_0} E_y + \frac{e_z^i}{r_0} E_z + \frac{u_1^i}{r_0^2} U_1 + \dots \right).
\tag{2.10}
$$

r_0 is a constant with dimensions of length. The choice of r_0 corresponds to the setting the units of the coefficients $e_{x,y,z}^i$ and u_j^i. We typically set $r_0 = 1$ mm. Due to the superposition
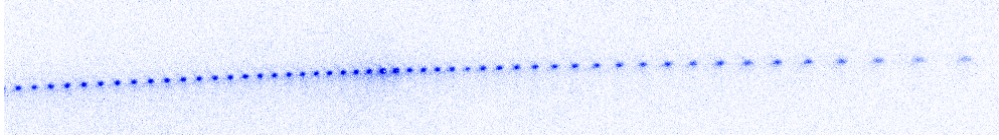
Figure 2.2: CCD image of ~ 60 ions trapped in one of the traps discussed in this work.

principle [32], given a set of voltages on all electrodes, the total potential Φ will be the sum

$$
\begin{aligned}
\Phi(x, y, z) &= \frac{e_x}{r_0} E_x + \frac{e_y}{r_0} E_y \frac{e_z}{r_0} E_z + \frac{u_1}{r_0^2} U_1 + \dots \\
&= \sum_i \Phi^i(x, y, z) \\
&= \sum_i V^i \left(\frac{e_x^i}{r_0} E_x + \frac{e_y^i}{r_0} + E_y \frac{e_z^i}{r_0} E_z + \frac{u_1^i}{r_0^2} U_1 + \dots \right).
\end{aligned}
\tag{2.11}
$$

Provided that there are enough (i.e. ≥ 8) electrodes which generate linearly independent fields, the potential can be completely controlled by choosing the set V^i of bias voltages to achieve the desired total potential. This can be done, e.g., by a matrix inversion or a least-squares solution.

2.3 Multiple ions

The picture is somewhat more complicated if multiple ions are contained in a single trap (Fig. 2.2). In this section, I will summarize the treatment of D. F. James [33]. The extra complication arises from the Coulomb interaction between ions. This interaction leads to coupling between the motion of the individual ions. In this case, the equations of motion can be diagonalized, leading to a set of harmonic modes.

Under the typical assumption that the radial confinement is sufficiently strong, the most energetically favorable condition is for the ions to form a line. It is helpful to define the the system potential energy as V:

$$
V = \sum_i \frac{1}{2} m \left(\omega_x^2 x_i^2 + \omega_y^2 y_i^2 + \omega_z^2 z_i^2 \right) + \sum_{i,j} \frac{Q^2}{8\pi\epsilon_0} \frac{1}{|\mathbf{r}_i - \mathbf{r}_j|}.
\tag{2.12}
$$

Here $\mathbf{r}_i = (x_i, y_i, z_i)$ is the (in general quantum) position of the ith ion. m and Q are the ion mass and charge respectively. ω_x, ω_y, and ω_z are the frequency of the external potential (dc + pseudopotential) in the x, y, and z directions. It is in general possible for these frequencies to vary as a function of position. The sum is taken over the ions. The normal modes of the ion chain are calculated by assuming the ion positions are given by small excursions around the equilibrium points, i.e. $\mathbf{r}_i = \mathbf{r}_i^{\text{eq}} + \vec{\delta}_i$.
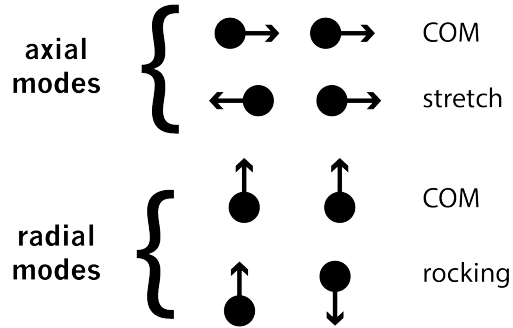
Figure 2.3: Schematic drawings of the normal modes for a two ion chain. Arrows indicate the displacements each ion undergoes in the corresponding normal mode. The abbreviation "COM" stands for center-of-mass. In an ion chain, there are two radial COM and two radial rocking modes-one for each radial direction of motion.

When discussing collective modes of an ion chain, we typically differentiate between "axial" modes and "radial" modes. The axial modes refer to excitations along the trap axis $\hat{z}$. The radial modes are modes in which the ions are displaced in the radial $\hat{x}$ and $\hat{y}$ directions. The frequencies of the radial modes of the ion chain tend to be more closely spaced as compared to the axial modes. This can be most easily understood by considering the case of 2 ions in a line along the $\hat{z}$ axis, separated by a distance d. If one of the ions is displaced by δ_z, the distance between the ions changed by δ_z, and the change in the energy of the configuration is $\frac{\delta_z}{d}$. This is the coupling energy of the axial motion, and also the splitting between the two axial modes. By contrast, if an ion is displaced radially by δ_x, the distance between ions is only changed by $\approx \frac{\delta_x}{2d}$, and thus the energy change is much smaller than the axial case.

For the results in this thesis, it is only necessary to understand ion chains of up to two ions, and therefore a total of six harmonic modes, summarized in Fig. 2.3. When the total confinement is harmonic, the axial COM mode has frequency ω_z, and the axial stretch mode has frequency $\sqrt{3}\omega_z$. We typically work with $\omega_z \approx 2\pi \times 1$ MHz, and therefore the stretch mode would have the higher frequency $2\pi \times 1.7$ MHz. There are two radial COM modes, with frequencies ω_x and ω_y, both typically in the range of $2\pi \times (2-3)$ MHz. The x and y radial rocking modes have frequencies $\sqrt{\omega_x^2 - \omega_z^2}$ and $\sqrt{\omega_y^2 - \omega_z^2}$, respectively [56].

Chapter 3

Light-matter interactions

Our primary means of interacting with trapped ions is through laser light. Lasers facilitate our ability to cool ions' motion, as well as measure and manipulate their internal states.

3.1   Ca$^+$ internal structure

In our experiments, we work with the ion species ^{40}Ca$^+$. Since neutral ^{40}Ca has two valence electrons, the singly ionized species ^{40}Ca$^+$ has a single valence electron and therefore has a hydrogenic level structure. It has no nuclear spin and therefore no hyperfine structure.

The ground state of ^{40}Ca$^+$ is a ^{2}S$_{1/2}$ level, which couples via an electric dipole transition to the ^{2}P$_{1/2}$ level (Fig. 3.1. This ^{2}S$_{1/2}$ $\leftrightarrow^2$P$_{1/2}$ transition is addressed with 397 nm light. This transition enables Doppler cooling (Sec. 3.2) and state detection (Sec. 3.2). The excited state spontaneously decays to either the ^{2}S$_{1/2}$ level (with probability 93.5%) or the ^{2}D$_{3/2}$
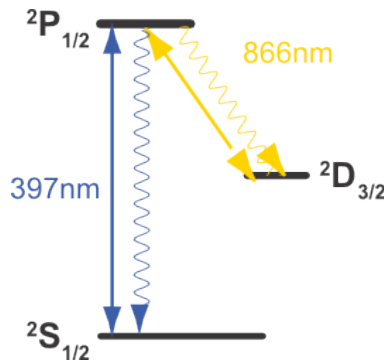
Figure 3.1: The ^{2}S$_{1/2}$ $\leftrightarrow^2$P$_{1/2}$ and ^{2}P$_{1/2}$ $\leftrightarrow^2$D$_{3/2}$ transitions. Double-headed arrows indicate atomic transitions. Squiggly lines indicate spontaneous emission decay paths. As noted in the main text, the P level decays about 6.5% of the time to the D level. Image used with permission from P. Schindler.
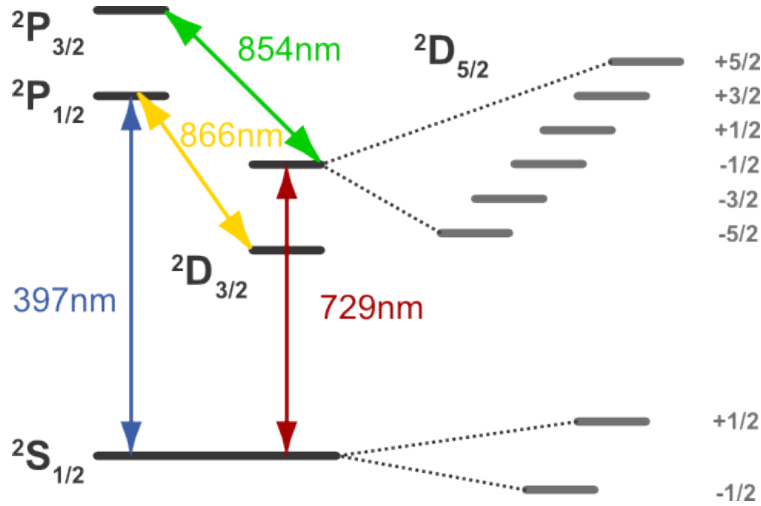
Figure 3.2: Internal structure of ^{40}Ca$^+$ displaying relevant energy levels. Arrows indicate lasers used in the experiment to address the transitions. The light grey lines represent Zeeman sublevels. Image used with permission from P. Schindler.

level (with probability 6.5%) [53]. In the case that the ion has decayed to the ^{2}D$_{3/2}$ state, it may be repumped back to ^{2}P$_{1/2}$ with 866 nm laser light.

The experiments presented in this work also make use of additional internal levels (see Fig. 3.2 for a summary). In addition to the dipole transition, we also make use of the ^{2}S$_{1/2}$ $\leftrightarrow$^{2}D$_{5/2}$ electric quadrupole transition, with an excited state lifetime of 1.2 s [41], with a sub-Hz natural linewidth. The long lifetime of this state permits the creation and manipulation of coherent superpositions of sublevels of the S and D manifolds. For instance, pairs of S and D sublevels have been used as qubits in quantum information processing experiments with ^{40}Ca$^+$ [61]. Owing to technical sources of line broadening in our experiments, we do not achieve this fundamental limit in practice. We experimentally observe the linewidth to be of order 1 kHz. This narrow line allows the Zeeman structure of the ^{2}S$_{1/2}$ $\leftrightarrow$ ^{2}D$_{5/2}$ transition to become resolved at even quite small magnetic fields (we work, for example, at about 3 G magnetic fields, where the sublevels are several MHz apart).

Since the lifetime of the ^{2}D$_{5/2}$ state is so long, it is not feasible to wait for spontaneous emission to "reset" the ion back to the ^{2}S$_{1/2}$ state on demand. However, the ^{2}D$_{5/2}$ $\leftrightarrow$ ^{2}P$_{3/2}$ transition may be addressed via a laser at 854 nm. Repumping the ion from the D state back to the P state allows the ion to be reset into the ground state through spontaneous emission from the P level.

3.2 Doppler cooling

In our experimental system, Doppler cooling is effected through a combination of 397 nm and 866 nm laser light, as indicated in Fig. 3.1. The excited state lifetime of the ^{2}P$_{1/2}$ level

is about 7 ns [35], significantly faster than the ion motional oscillation period (on the order of 0.5-2 μs). Thus, during an absorption-emission cycle on this transition, the ion velocity is approximately constant. This justifies a semi-classical treatment such as that presented in [43] or [56], in which the effect of the 397 nm laser is treated as a radiation pressure force depending on the ion's velocity.

Although a single ion has three normal modes of motion, the radiation pressure force can be understood as acting on each mode independently. Therefore it is sufficient to consider interactions with only a single mode Consider an ion irradiated with a single 397 nm cooling beam with wave-vector $\mathbf{k}$. Assume that the cooling beam is oriented along a particular normal mode of motion. In this approximation, we assume that the ion receives an impulse $\Delta p = \hbar k$ into the mode each time it absorbs a 397 nm photon. Meanwhile, each decay event is followed by spontaneous emission which transfers momentum into a random direction, with an average value of zero momentum transfer on emission. Most decay events will return the ion to the ^{2}S$_{1/2}$ level, but will occasionally leave the ion in the ^{2}D$_{3/2}$ state, in which it will no longer interact with the cooling beam. In order to continue interacting with the cooling beam, the ion must then be repumped to the ^{2}P$_{1/2}$ with an 866 nm laser. The average force is equal to the average rate of momentum change, i.e.

$$F = \left\langle \frac{dp}{dt} \right\rangle = \hbar k \Gamma \rho_{ee}, \tag{3.1}$$

where Γ is the decay rate out of the excited state and ρ_{ee} is the time-independent probability to find the ion in the excited state. The excited state population depends on the laser detuning Δ from the atomic resonance in the laboratory frame, the velocity-dependent Doppler shift of the resonance frequency (kv, with v the ion velocity), strongly the atomic resonance is driven. It is common to quantify how strongly a laser is driving an atomic transition in terms of the saturation parameter $s = 2|\Omega|^2/\Gamma^2$, where Ω is the on-resonance Rabi frequency. In the weak excitation ($s \to 0$) limit, ρ_{ee} takes the Lorentzian lineshape [43]:

$$\rho_{ee} = \frac{s/2}{1 + \left(\frac{2(\Delta - kv)}{\Gamma} \right)^2}. \tag{3.2}$$

$\Delta - \mathbf{k} \cdot \mathbf{v}$ appears in the line above because it is the laser detuning in the ion's reference frame. We can calculate the cooling rate $\dot{E}_c$ (the rate heat is removed from the ion's motion) by linearizing the force about small velocities:

$$F = \hbar k \Gamma \frac{s/2}{1 + \left(\frac{2(\Delta - kv)}{\Gamma} \right)^2} \tag{3.3}$$

$$= F_0 + \frac{dF}{dv} v \tag{3.4}$$

$$= F_0 \left(1 + \frac{8k\Delta}{\Gamma^2 + 4\Delta^2} v \right), \tag{3.5}$$

with $F_0 = \hbar k \Gamma \frac{s/2}{2+8\Delta^2/\Gamma^2}$.

The work done on the ion by the radiation pressure force is $F dx$ through an infinitesimal displacement of the ion, and therefore the cooling rate is

$$\dot{E}_c = \langle F v \rangle \tag{3.6}$$

$$= \left\langle F_0 \left(1 + \frac{8k\Delta}{\Gamma^2 + 4\Delta^2} v\right) v \right\rangle \tag{3.7}$$

$$= F_0 \frac{8k\Delta}{\Gamma^2 + 4\Delta^2} \langle v^2 \rangle. \tag{3.8}$$

As with any cooling process, the cooling limit is reached when the cooling rate is equal to the heating rate. We claimed earlier that each absorption/emission cycle has $\langle \Delta p \rangle = 0$, i.e. that no momentum is transferred on average. However, it is not true that $\langle (\Delta p)^2 \rangle = 0$– multiple iterations of the absorption/emission cycle cause the ion's momentum distribution to diffuse as a random walk. This happens both during absorption and during emission. Although the momentum kicks during absorption are all in the same direction, they occur at random times with respect to the ion's trajectory, leading to diffusion. Also, the emission events occur in random directions, also causing the momentum distribution to diffuse. Since the process is a random walk, $\langle (\Delta p)^2 \rangle \sim (\hbar k)^2 N$, where N is the number of photon scattering events.

Following [43], the effect of all of this can be incorporated by taking

$$\dot{E}_h = \frac{1}{2m} \frac{d}{dt} \langle p^2 \rangle \tag{3.9}$$

$$= \frac{1}{2m} (\hbar k)^2 \Gamma \rho_{ee}(v=0)(1+\xi), \tag{3.10}$$

where ξ is a geometrical factor taking the value 2/5.

Setting $\dot{E}_h = \dot{E}_c$ and making the thermodynamic association $m\langle v^2 \rangle = k_B T$, we find a minimum temperature $T = \frac{\hbar \Gamma}{4k_B}(1 + \xi)$, achieved for $\Delta = \Gamma/2$. For a $^{40}\text{Ca}^+$ ion, taking $\Gamma = 1/(7 \text{ ns})$, this corresponds to an average motional occupation of about 6 quanta at a $2\pi \times 1$ MHz oscillation frequency.

The interpretation of temperature

It is worth discussing what it meant by "temperature" in the case of trapped ion experiments, as we deal only with one or a very small number of individual trapped ions. Since we prepare the motional state of ions via an incoherent process (e.g. Doppler cooling), one might expect that after state preparation, the vibrational modes of the ions are left in a set of well-defined quantum states, i.e. $\{n_1, n_2, n_3, \} = \{3, 8, 1\}$.

Indeed, this is the view we typically take in experiments–that after cooling, the motional state of the ions is prepared to some particular quantum state in the energy eigen-basis. However, we usually repeat our measurements 100-1000 times in order to obtain measurement statistics. The interpretation of temperature that I will take throughout this work is
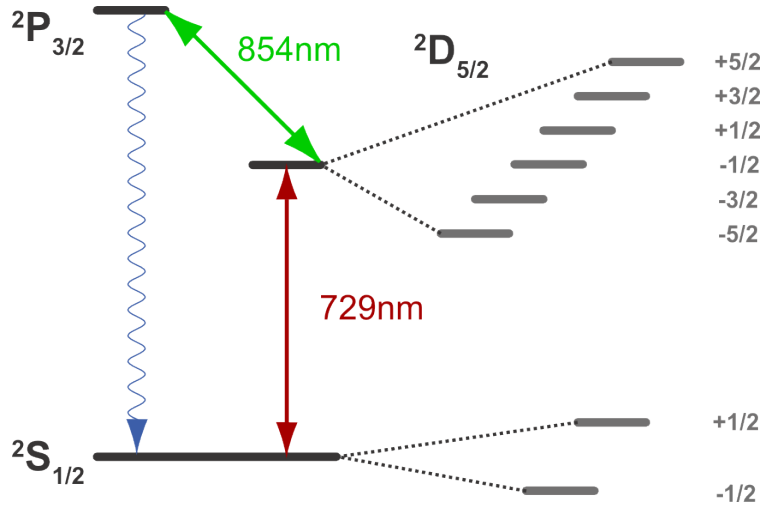
Figure 3.3: Electronic energy levels of ^{40}Ca$^+$ relevant to coherent operations with the 729 nm laser. The light grey lines represent Zeeman sublevels. Squiggly line is a spontaneous emission decay path. Image used with permission from P. Schindler.

to consider that the motional state of the ions is prepared to a random initial state in each iteration of the experiment, but that the random initial state follows a Boltzmann distribution characterized by some temperature, or equivalently, some average motional occupation number.

3.3 Coherent operations and resolved sidebands

Coherent operations in our system take place on the ^{2}S$_{1/2} \leftrightarrow {}^2D_{5/2}$ transition. This transition is dipole-forbidden, but allowed via an electric quadrupole interaction whereby the orbital angular momentum of a laser light field allows the atom to undergo angular momentum change of $\Delta \ell = 2$. While these transitions are on the order of 10^6 times slower than dipole allowed transitions (for the same laser intensity), nevertheless the line can be driven with Rabi frequencies exceeding 1 MHz for ~ 1 mW of laser power focused to 20 μm.

The relevant electronic energy levels are shown in Fig. 3.3. In a magnetic field, the ^{2}S$_{1/2}$ level is Zeeman split into two sublevels, and the ^{2}D$_{5/2}$ level is split into 6 sublevels. In practice these sublevels are separated by about 1 MHz, with a magnetic field of about 3 G.

The magnetic quantum number change allowed by an electric quadrupole transition is $|\Delta m_j| \leq 2$. This means a total of 10 lines can appear in optical spectroscopy of the $S \leftrightarrow D$ transition.

Optical pumping is done via illuminating the ion with both the 854 nm laser and tuning the 729 nm laser resonant with the $|S, m_j = +1/2\rangle \rightarrow |D, m_j = -3/2\rangle$ transition. The 854 nm laser repumps the ion out of the D state back into the S state via spontaneous emission out of the P state, whereupon it can decay to either $m_j = \pm 1/2$. However, once

the $|S, +1/2\rangle$ state is no longer populated, the ion becomes dark to the 729 nm laser light, at which point the ion is optically pumped into the pure state $|S, -1/2\rangle$.

In order to analyze the laser-ion interaction, it is helpful to write down a Hamiltonian describing the system. We will roughly follow the derivation of [43]. For coherent operations on single ions, we typically consider only one set of Zeeman sublevels, for instance the set consisting of $\{|S, -1/2\rangle, |D, -1/2\rangle\}$, which we shorten to $\{|S\rangle, |D\rangle\}$. This is the two level atom approximation. The states $|S\rangle$ and $|D\rangle$ can form a qubit, due to the long lifetime of superpositions of these levels. If we restrict our analysis to these two states, the Hamiltonian for the qubit plus the motion of the ion can be written

$$H_0 = \frac{\hbar\Delta}{2}\sigma_z + \sum_i \hbar\nu_i a_i a_i^\dagger. \tag{3.11}$$

Here, Δ is the energy splitting of the states $|S\rangle$ and $|D\rangle$, and σ_z is the Pauli spin operator. The sum is taken over the vibrational degrees of freedom of the ion (i.e., in the pseudopotential approximation), and ν_i are the vibrational frequencies (typically on the order of hundreds of kHz to a few MHz). The most basic form of the laser-ion interaction is

$$H_{LI} = \frac{\hbar\Omega}{2}e^{i(kx_i\cos(\theta)-\omega_L t+\phi)}\sigma^+ + \text{ h.c.}, \tag{3.12}$$

where $k = 2\pi/\lambda$ is the length of the laser wave-vector, x_i is the displacement of the ion's i^{th} vibrational mode, θ is the angle between the laser wave-vector and the x_i direction, ω_L is the laser frequency, and ϕ is the phase of the laser light field. Ω is the coupling strength of the laser to the electronic transition, proportional to the laser field intensity and σ^+ is the Pauli spin raising operator. h.c. denotes Hermitian conjugation.

Under the assumption that the ion is sufficiently cold that its wavefunction extent is much smaller than the laser wavelength, we can treat kx as a small parameter and expand the exponential as

$$e^{i(kx_i\cos(\theta)-\omega_L t+\phi)} \approx (1 + ikx_i\cos(\theta))e^{i(-\omega_L t+\phi)} \tag{3.13}$$

$$= \left(1 + ik\cos(\theta)\sqrt{\frac{\hbar}{2m\nu_i}}(a_i + a_i^\dagger)\right)e^{-i(\omega_L t-\phi)}, \tag{3.14}$$

where m is the ion mass. When $kx\cos(\theta)$ can be treated as a small parameter, the ion is said to be in the *Lamb-Dicke regime*. The quantity $k\cos(\theta)\sqrt{\frac{\hbar}{2m\nu_i}} \equiv \eta_i$, and η_i is called the *Lamb-Dicke parameter*. We typically work well within this regime: A Ca$^+$ ion with 1 MHz oscillation frequency has a spatial wavefunction extent of about 9 nm, much smaller than the 729 nm wavelength, justifying the Lamb-Dicke approximation throughout most of this work.

We can plug our simplified exponential back into Equation 3.12 to obtain

$$H_{LI} \approx \frac{\hbar\Omega}{2}\sigma^+ \left(1 + i\eta_i(a_i + a_i^\dagger)\right)e^{-i(\omega_L t-\phi)} + \text{ h.c.} \tag{3.15}$$

At this point we transform into the interaction picture, using Equation 3.11 as the free Hamiltonian. We obtain:

$$H_{LI}^{(i)} = \frac{\hbar\Omega}{2}\sigma^+ e^{i\Delta t}\left(1 + i\eta(a_i e^{-i\nu_i t} + a_i^\dagger e^{i\nu_i t})\right)e^{-i(\omega_L t - \phi)} + \text{ h.c.} \tag{3.16}$$

This is the laser ion interaction to first order in η_i. By tuning the laser frequency ω_L, certain parts of this Hamiltonian may be selected via the rotating wave approximation (RWA):

$$H_{LI}^{(i)}/\hbar \approx \begin{cases} \frac{\Omega}{2}e^{i\phi}\sigma^+ + \text{ h.c} & \text{if } \omega_L = \Delta \\ i\frac{\eta_i\Omega}{2}e^{i\phi}\sigma^+ a_i + \text{ h.c.} & \text{if } \omega_L = \Delta - \nu_i \\ i\frac{\eta_i\Omega}{2}e^{i\phi}\sigma^+ a_i^\dagger + \text{ h.c.} & \text{if } \omega_L = \Delta + \nu_i \end{cases} \tag{3.17}$$

The first piece of Equation 3.17 occurs when the laser frequency is resonant to the splitting between states $|S\rangle$ and $|D\rangle$. This term causes population to oscillate between the $|S\rangle$ and $|D\rangle$ with Rabi frequency Ω.

In the Bloch sphere picture, with the south pole being state $|S\rangle$ and the north pole $|D\rangle$, this interaction causes the ion's Bloch vector to rotate about a vector in the xy plane. The particular vector is defined by the choice of laser phase ϕ, and given by $\hat{n} = \cos(\phi)\hat{x} + \sin(\phi)\hat{y}$. We often call such a transition a "carrier" transition, in contrast to the "sideband" transitions discussed below.

The second and third lines of Eq. 3.17 are often called "sideband" transitions. They occur when the laser is either red or blue of the electronic transition by the frequency corresponding to one motional quantum. These transitions flip the ion's electronic state while also adding or removing a motional quantum. Tuning the laser to the "red sideband" generates the interaction $\hbar\eta_i\frac{\Omega}{2}(\sigma^+ a_i + \sigma^- a^\dagger)$ (setting the laser phase to zero). On the "blue sideband", the interaction is $\hbar\eta_i\frac{\Omega}{2}(\sigma^+ a_i^\dagger + \sigma^- a_i)$. Since the matrix elements of a_i scale with $\sqrt{n}$, where n is the vibrational quantum number, the Rabi frequency of these transitions is $\sqrt{n}\eta_i\Omega$ on the red sideband and $\sqrt{n+1}\eta_i\Omega$ on the blue sideband.

In general, there exist sideband transitions for every vibrational mode of an ion crystal, e.g. each carrier transition in a single trapped ion has three red and three blue sidebands to first order in η. There are also second and higher order sidebands in which, for instance, two vibrational quanta are added or removed. See Fig. 3.4 for a summary of the first order transitions.

3.4 Sideband cooling

Doppler cooling is capable of preparing trapped ions into the Lamb-Dicke regime, with average motional occupations of less than 10 quanta for typical trap frequencies of 1-2 MHz. However, this process is fundamentally limited by the linewidth of the cooling transition. A second stage of cooling, called "sideband cooling", can cool ions into the ground motional

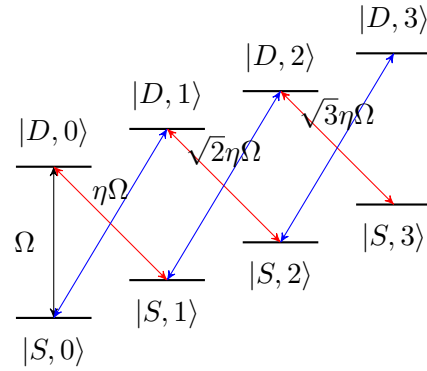Figure 3.4: Carrier and first order sideband transitions in the two level atom (plus harmonic motion) approximation. Energy levels are in the basis $\{|S\rangle, |D\rangle\} \otimes \{|n_i\rangle\}$ where n_i is the motional quantum number of oscillator mode i. In general there is one level for each combination of oscillator states.
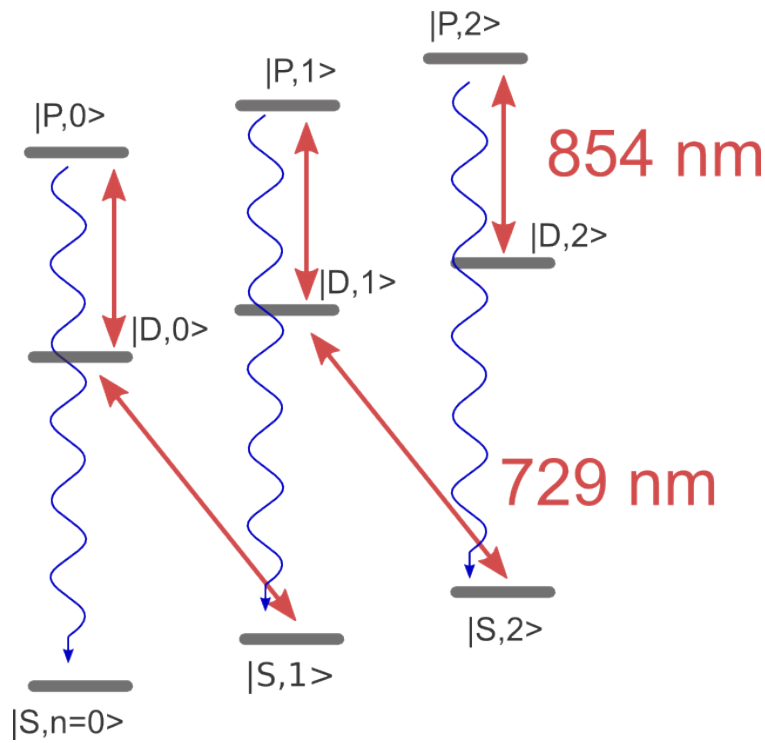

Figure 3.5: Schematic drawing of the sideband cooling process.

state with high probability by taking advantage of the significantly smaller linewidth of the quadrupole $S_{1/2} \leftrightarrow D_{5/2}$ transition.

In the sideband cooling process, the ion is illuminated with laser light at 854 nm and 729 nm. The 729 nm light is resonant to the red sideband. This is shown schematically in Fig. 3.5. The red sideband transition causes the ion to undergo an $|S, n\rangle \rightarrow |D, n-1\rangle$ transition. The 854 nm repumper "resets" the electronic state of the ion back to $|S\rangle$ by promoting the electron to the $P_{3/2}$ state, from which it spontaneously decays back into $|S\rangle$. In the Lamb-Dicke regime, most of the spontaneous decays do not cause heating (see below). Crucially, the ion stops absorbing photons when it reaches the ground ($|S, 0\rangle$) state– this can be seen in the second line of Eq. 3.17. If the motional state of the ion ion is $|0\rangle$, $H_{LI} = 0$ because $a_i|0\rangle = 0$. The presence of the repump laser couples the $|D\rangle$ and $|P\rangle$ states, artificially broadening the linewidth of the carrier and sideband transitions.

As in Doppler cooling, the linewidth of the cooling transition poses the fundamental limit to the lowest achievable temperature [56]. If the ion reaches the ground state, it may still absorb photons due to the finite, however small, linewidth of the carrier transition. Such an absorption event would take the ion from $|S, 0\rangle \rightarrow |D, 0\rangle$. From $|D, 0\rangle$, the ion will be pumped to the P level and spontaneously decay to the S state by emitting a 393 nm photon. The chance that this decay process causes heating may be analyzed with Fermi's golden rule, in which the transition probability is proportional to the Hamiltonian matrix element connecting the states [8].

Spontaneous emission is caused by an electric dipole interaction between the ion and the background electromagnetic field, H_{AF}. In order to compare the fraction R of spontaneous decays which heat the ion as compared to those which do not, we do not need to fully derive the theory of spontaneous emission; we need only work out the ratio of matrix elements:

$$R = \frac{|\langle P, 0|H_{AF}|S, 1\rangle|^2}{|\langle P, 0|H_{AF}|S, 0\rangle|^2} \sim \frac{|\langle P, 0|e^{i\tilde{\eta}(a+a^\dagger)}|S, 1\rangle|^2}{|\langle P, 0|e^{i\tilde{\eta}(a+a^\dagger)}|S, 0\rangle|^2} = \tilde{\eta}^2, \tag{3.18}$$

where $\tilde{\eta}$ is the Lamb-Dicke parameter for the 393 nm photon emitted during spontaneous emission, numerically about 0.17 for a 1 MHz oscillation frequency. Heating occurs when the carrier transition is driven off-resonantly by the 729 nm light resonant to the red sideband transition, and occurs at a rate proportional to Γ^2. The heating rate is then the rate of carrier scattering times R. The limit for sideband cooling may then be analyzed using rate equations [56], arriving at the result

$$\bar{n}_i = \frac{\Gamma^2}{4\nu_i^2}\left(\left(\frac{\tilde{\eta}}{\eta_i}\right)^2 + \frac{1}{4}\right), \tag{3.19}$$

with $\bar{n}_i$ the average occupation number of mode i, and Γ the linewidth of the cooling transition. Γ here should not be taken to be the natural linewidth (i.e. 1 Hz), but rather the linewidth of the transition with the repump light applied. By choosing the cooling linewidth much smaller than the trap frequency, the ion can be prepared in the ground state with

high probability. With $\Gamma = 100$ kHz and $\nu_i = 1$ MHz, this would give a temperature limit of $\bar{n} = 0.01$. However, this idealized derivation does not take into account other heating sources such as noisy electric fields from the trap electrodes. In the experiments discussed in this work, these sources heat the ion at rates between 10 and 200 quanta/s. At the high end, this limits the practically achievable minimum temperature to $\bar{n} \approx 0.2$.

Temperature measurement

The average motional occupation may be determined by spectroscopy of the sidebands [43]. The difference between red and blue sideband excitation at constant time encodes the desired information.

Consider the following procedure. First, prepare via some cooling mechanism the vibrational modes of the ion to some thermal distribution. Suppose that the vibrational mode of interest has mean thermal occupation $\bar{n}$. Then, illuminate the ion with light resonant to the red sideband for some fixed time t and measure the probability to find the ion in the D state, $P_{D,r}$. Then, repeat the preparation process, and illuminate the ion on the blue sideband for time t, and again measure the D state probability, $P_{D,b}$.

Illuminating the ion on one of the sidebands drives a family of transitions $|n\rangle \to |n \pm 1\rangle$ at the same time, with an n dependent Rabi frequency. Population is assumed to be incoherently distributed along the motional ladder according to Boltzmann statistics. Therefore the D state probability is the incoherent sum of all of these processes, weighted by the population in the initial states. When the 729 nm laser is resonant to the red sideband, we know from Eq. 3.17 that each transition $|S, n\rangle \to |D, n-1\rangle$ occurs with the Rabi frequency $\sqrt{n}\eta_i\Omega$, and therefore:

$$P_{D,r} = \sum_{n=1}^{\infty} P_n \sin^2\left(\sqrt{n}\eta_i\Omega t\right) \tag{3.20}$$

$$= \sum_{n=1}^{\infty} \left(\frac{\bar{n}}{\bar{n}+1}\right)^n \sin^2\left(\sqrt{n}\eta_i\Omega t\right) \tag{3.21}$$

$$= \frac{\bar{n}}{\bar{n}+1} \sum_{n=0}^{\infty} \left(\frac{\bar{n}}{\bar{n}+1}\right)^n \sin^2\left(\sqrt{n+1}\eta_i\Omega t\right). \tag{3.22}$$

Meanwhile, with the laser resonant to the blue sideband (assuming the same laser intensity as above), we can use Eq. 3.17 to obtain the D-state probability in this case as well:

$$P_{D,b} = \sum_{n=0}^{\infty} P_n \sin^2\left(\sqrt{n+1}\eta_i\Omega t\right) \tag{3.23}$$

$$= \sum_{n=1}^{\infty} \left(\frac{\bar{n}}{\bar{n}+1}\right)^n \sin^2\left(\sqrt{n+1}\eta_i\Omega t\right). \tag{3.24}$$

In Eq. 3.21 we use the fact that for a harmonic oscillator with average thermal occupation $\bar{n}$, the occupation probability for the state n is $P_n = \left(\frac{\bar{n}}{\bar{n}+1}\right)^n$ [21]. For fixed excitation time t, the ratio of red to blue sideband heights takes a simple form which depends only on the mean thermal occupation $\bar{n}$:

$$\frac{P_{D,r}}{P_{D,b}} = \frac{\bar{n}}{\bar{n}+1}. \tag{3.25}$$

Thus, the thermal occupation can be extracted by comparing the red and blue sideband heights. This method works as long as the sideband heights are experimentally distinguishable. An estimate of this maximum measurable temperature can be extracted by assuming the blue sideband height is of order $P_{D,b} = 0.5$. With 100 experimental repetitions (a typical value), the statistical error on this parameter will be $\delta P_b = 0.5/\sqrt{100} = 0.05$. At the highest measurable temperatures, the red sideband height $P_{D,r}$ is also of order 0.5 and therefore $\delta P_r \approx \delta P_b = 0.05$. To fully resolve the peak height, we should require $P_{D,b} - P_{D,r} \approx 2\delta P_b$, so that statistical fluctuations in the red and blue sideband heights do not overlap. Using this condition, we get $P_{D,r} = 0.4$, implying that $\bar{n}_{\max} = 4$ is the highest measurable thermal occupation by this method.

3.5 Electron shelving

We have until now ignored how to measure the ion in the $\{|S\rangle, |D\rangle\}$ basis. For this process we use a technique called electron shelving [16]. The ion is illuminated with both 397 nm and 866 nm light. If the ion is in the $|S\rangle$ state, it will scatter photons and emit 397 nm photons from the dipole transition. Within 5 ms, we can typically detect up to 30 photons from a single ion on a photomultiplier tube (PMT). On the other hand, if the ion is in the $|D\rangle$ state, it will not interact with either 397 nm or 866 nm light, and therefore will not fluoresce. Thus, by applying the laser light and counting detected photons from a PMT for several milliseconds, the ion can be projectively measured to be in either the $|S\rangle$ or $|D\rangle$ state. The process also works for multiple ions if a charge-coupled device (CCD) camera is used for the readout. In that case, the camera is exposed for several ms, and the state of each ion in the chain is determined by analyzing the resulting image.

3.6 Engineered interactions

In the remainder of this chapter, I will discuss a few more light-matter interactions which are used in the experiments described in this thesis. These interactions are more complicated than the interactions discussed above, in the sense that the form of their interaction with the ion is not immediately obvious from the basic laser-ion Hamiltonian. For instance, they often involve illumination of the ion with bichromatic laser light.

Here, we will mostly concern ourselves with obtaining "effective Hamiltonians." An effective Hamiltonian is a Hamiltonian operator which faithfully describes the dynamics of the laser-ion interaction.

Coherent motional displacement

One such interaction is coherent displacement of the motional state via the 397 nm dipole transition. This method is discussed in [52]. Using the same notation as Section 3.2, illuminating the ion with 397 nm light at saturation produces the radiation pressure force

$$F = \hbar k \Gamma \rho_{ee} \tag{3.26}$$
$$= \hbar k \Gamma / 2 \tag{3.27}$$

This force may be modulated, for instance, by switching an acousto-optic modulator (AOM) on and off at a certain frequency ω_m. If $\omega_m \approx \nu_i$, where ν_i is one of the vibrational frequencies of the trapped ion, this force can affect a coherent displacement of the motional state. If the laser is operated at saturation, this method can achieve a displacement amplitude $|\alpha|^2 = 100$ in less than 10 μs [52]. This is useful, among other things, for probing the trap frequency to high precision.

ac Stark shift

In the two level atom picture with states $|S\rangle$, and $|D\rangle$, the energy splitting between the states can be modified by applying a 729 laser beam with coupling strength Ω off-resonant to all carrier and sideband transitions. In the two level atom picture, if the beam is detuned by Δ from the carrier transition, the presence of such a beam may be described by the interaction Hamltonian term [18]:

$$H_I = \frac{\hbar \Omega^2}{4\Delta} \sigma_z. \tag{3.28}$$

In a real atom, the ac Stark shift has a more complicated form, including contributions from all carrier and sideband transitions as well as the far off-resonant dipole transitions which are roughly of the same order as the contribution above. However, the energy shift may be determined experimentally [24].

Mølmer-Sørensen interaction

Two ions in the same trap have an effectively negligible interaction between their electronic state owing to the several micron distance between the ions. However, an interaction between the ions' electronic states may be engineered using the Mølmer-Sørensen technique [65, 57]. This method has been used as an entangling gate in quantum information processing experiments [61], and is referred to as a "Mølmer-Sørensen gate" in this context.
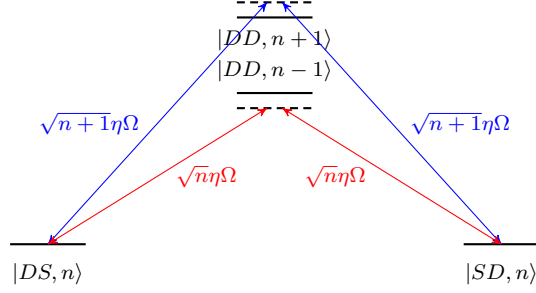
Figure 3.6: Simplified sketch of the Mølmer-Sørensen interaction. As drawn here, the system is initialized into some combination of $|SD, n\rangle$ and $|DS.n\rangle$. Take the initial state to be $|DS, n\rangle$. From the bluer of the two laser tones at frequency ω_+, the system may undergo a two photon Raman transition from $|DS, n\rangle \rightarrow |SD, n\rangle$, following the blue path in the sketch. Similarly, the system can follow the red path. Due to a quantum interference between the two paths, there is no n dependence on the transition rate. Transitions to $|SS\rangle$ state also occur but are left off for clarity.

In the simplest picture, consider two ions in the same trap. Both ions participate in some common vibrational mode with frequency ν (the "bus mode"), and both have the same qubit splitting Δ. The bare Hamiltonian is then

$$H_0 = \frac{\hbar\Delta}{2}\left(\sigma_z^{(1)} + \sigma_z^{(2)}\right) + \hbar\nu a^\dagger a. \tag{3.29}$$

Now suppose both ions are equally illuminated with a bichromatic 729 nm laser beam. The laser beam has two tones with frequencies $\omega_\pm = \Delta \pm (\delta + \nu)$ (see Fig. 3.6), i.e., these tones are nearly resonant with the red and blue sidebands of the ion crystal, but are detuned by $\delta \ll \nu$. Each tone has coupling strength Ω. In the experiments described here, we will always work in the regime $\eta\Omega \ll \delta$–that is, in the limit where the laser tones cannot directly excite the sideband transitions. We call this the "adiabatic regime." In this regime, the process may be described as a Raman transition.

In this limit, the effective Hamiltonian takes the form [57]

$$H_I = \frac{\hbar\eta\Omega^2}{2(\nu - \delta)}\sigma_x^{(1)} \otimes \sigma_x^{(2)}. \tag{3.30}$$

This is a Hamiltonian which drives collective flips between $|SD\rangle \leftrightarrow |DS\rangle$, or $|SS\rangle \leftrightarrow |DD\rangle$, where $|xy\rangle$ means that ion one is in state $|x\rangle$ and ion two is in state $|y\rangle$. Surprisingly, the effective Hamiltonian contains no n dependence. This is due to a quantum interference between the two paths shown in Fig. 3.6 [65]. Each of the two paths can be thought of as a two-photon Raman transition. The effective two-photon Rabi frequency on the blue path is proportional to $\eta\Omega^2(n + 1)$, and on the red path is proportional to $\eta\Omega^2(n)$. However, in the blue path the lasers are blue detuned from the intermediate state $|DD, n + 1\rangle$, and in
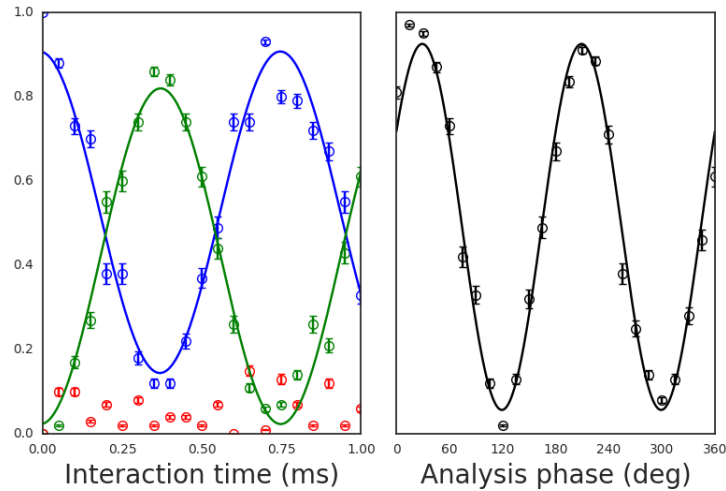
Figure 3.7: **Left**: Populations in the electronic states $|SS\rangle$ (blue curve and points), $|DD\rangle$ (green curve and points), and $|SD\rangle$ or $|DS\rangle$ (red data points). Approximately equal populations are achieved at the gate time $\tau = 0.18$ ms. **Right**: Parity (defined in the main text) of the two qubit state as a function of the analysis phase angle after the Mølmer-Sørensen interaction is applied for 0.18 ms. The oscillation is fit to a sine function yielding a measured contrast of 0.87(3). The parity contrast, taken together with the populations in the left plot, give the fidelity $\mathcal{F} \approx 0.90$ to a Bell state. These data were taken by Eli Megidish.

the red path are red detuned from the intermediate state $|DD, n-1\rangle$, and therefore the two paths interfere destructively. The result is that the n-dependence in the total transition rate drops out. This means that the interaction can entangle the electronic states of two ions even when the mediating mode is in a thermal state [40].

A perfect Mølmer-Sørensen interaction, when applied to the state $|SS\rangle$, causes the two-ion electronic state to oscillate between $|SS\rangle \leftrightarrow |DD\rangle$. When the state is in between $|SS\rangle$ and $|DD\rangle$, the entangled Bell state $|\Phi\rangle = \frac{1}{\sqrt{2}}\left(|SS\rangle + e^{i\phi}|DD\rangle\right)$ is produced.

Fig. 3.7 shows the population dynamics and phase coherence of resulting state when the interaction is implemented in our apparatus. The population dynamics is shown to mostly oscillate between $|SS\rangle$ and $|DD\rangle$ states, with a few percent of leakage out of this subspace, most likely due to unwanted laser phase noise driving spurious electronic state flips.

The phase coherence of the entangled state may be analyzed by applying the bichromatic Mølmer-Sørensen beams until the $|SS\rangle$ and $|DD\rangle$ populations are equal. Then, a global $\pi/2$ rotation is applied with phase θ relative to the entangling interaction. After an electron shelving readout of both ions, the parity is analyzed (defined in this case as $P|SS\rangle = P|DD\rangle = 1$, and $P|SD\rangle = P|DS\rangle = 0$). The parity is recorded as a function of the analysis pulse phase, and contrast c of the parity oscillations probes the phase coherence of the
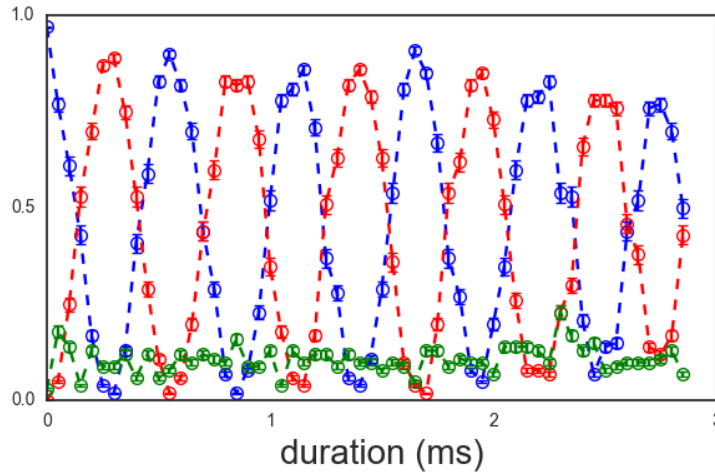
Figure 3.8: Mølmer-Sørensen gate interaction, showing spin flipping between the states $|SD\rangle$ (blue) and $|DS\rangle$ (red). Gate errors-when the system is found in either $|SS\rangle$ or $|DD\rangle$ are shown in green. Each data point is the average of 100 experimental repetitions.

resulting state. The fidelity to the Bell state can be measured as [58]

$$\mathcal{F} = \langle\Phi|\rho|\Phi\rangle \tag{3.31}$$

$$= \frac{1}{2}\left(P_{\text{SS}} + P_{\text{DD}} + c\right), \tag{3.32}$$

where ρ is the (mixed) state produced by the laser-ion interaction.

The interaction also works to induce oscillations between $|SD\rangle \leftrightarrow |DS\rangle$. A typical scan is shown in Fig. 3.8. In that scan, the ion was first prepared into the state $|SD\rangle$ via a local π-pulse on one ion before the bichromatic laser pulse was turned on. The ions were measured in the $\{|SS\rangle, |SD\rangle, |DS\rangle, |DD\rangle\}$ basis on a CCD camera.

Spin-motion entanglement

The final interaction we need to discuss we will call the $\sigma_z x$ interaction, generating entanglement between the electronic state of the ion and the motional state [38].

In a similar flavor to the previous section, this interaction is generated by illuminating an ion with a bichromatic laser field, having frequencies $\omega_+ = \Delta + \nu + \delta$ and $\omega_- = \Delta - \nu$, and $\delta \ll \nu$. ν is the frequency of some vibrational mode.

Since the laser tones are far in frequency from any atomic resonance, this interaction can be considered a Raman transition on the motional state (see Figure 3.9), as the two tones are separated in frequency by $\approx \nu$. Therefore this interaction moves $|n\rangle \to |n \pm 1\rangle$, suggesting that its effective Hamiltonian on the motion is proportional to $x = a + a^\dagger$.
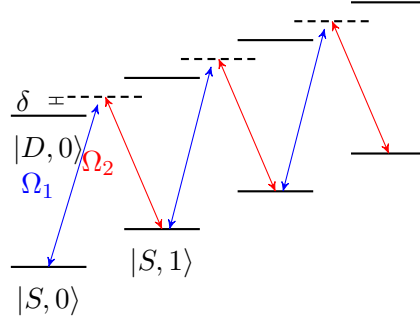
Figure 3.9: Sketch of the $\sigma_z x$ interaction. On resonance (i.e. $\nu = 0$), the interaction moves population in the motional state from $|n\rangle \to |n \pm 1\rangle$, while keeping the electronic population the same.

The basic laser-ion interaction can be determined from applying Eq. 3.12 twice (once for each laser tone). This yields:

$$H/\hbar = \left(\frac{\Omega_1}{2} e^{-i(\nu/2+\delta+\phi_1)t} + \frac{\Omega_2}{2} e^{i(\nu/2-\phi_2)t} \right)$$
$$\times \left(1 + i\eta(ae^{-i\nu t} + a^\dagger e^{i\nu t}) \right) \sigma^+ + \text{h.c.} \tag{3.33}$$

Here, $Omega_1$ (Ω_2) and phi_1 (ϕ_2) are the carrier Rabi frequency and phases of the laser tone with frequency ω_+ (ω_-). The time evolution of the above laser-ion Hamiltonian can be directly integrated, leading to the effective interaction

$$H = \frac{\hbar\eta\Omega_1\Omega_2}{2\nu}\sigma_z \left(ae^{-i\delta t} + a^\dagger e^{i\delta t} \right) \tag{3.34}$$
$$= \frac{\hbar\kappa}{2}\sigma_z \left(ae^{-i\delta t} + a^\dagger e^{i\delta t} \right). \tag{3.35}$$

This Hamiltonian is an interaction-picture Hamiltonian, related to the laboratory reference frame by the transformation matrix

$$U = e^{i\hbar\Delta t/2\sigma_z} e^{i\hbar\nu t a^\dagger a}, \tag{3.36}$$

thus accounting for evolution from the "free" Hamiltonian H_0 (Eq. 3.11). We could instead choose a different interaction picture, in which the free Hamiltonian is

$$H_0' = \frac{\hbar\Delta}{2}\sigma_z + \hbar(\nu - \delta)a^\dagger a). \tag{3.37}$$

With that choice of interaction picture, our effective interaction would be written

$$H = \frac{\hbar\kappa}{2}\sigma_z \left(a + a^\dagger \right) + \hbar\delta a^\dagger a, \tag{3.38}$$

a form we will use in Chapter 7.

This interaction generates a coherent displacement of the ion's motional state dependent on the electronic state, leading to entanglement of the electronic state with the ion motion if the motional state is pure. It is easiest to first understand the case where the motion is prepared in ground state, and $\delta = 0$. Then, under this interaction,

$$|S, 0\rangle \rightarrow |S, \alpha(t)\rangle \tag{3.39}$$

$$|D, 0\rangle \rightarrow |D, -\alpha(t)\rangle, \tag{3.40}$$

where $\alpha(t) = \frac{\kappa t}{2}$.

In general, for all choices of δ, the time evolution operator is (up to an overall phase)

$$U = \mathcal{D}(\alpha(t))|S\rangle\langle S| + \mathcal{D}(-\alpha(t))|D\rangle\langle D|, \tag{3.41}$$

with $\alpha(t) = \frac{\kappa}{2\delta}\left(1 - e^{i\delta t}\right)$. The ion's motional wavepacket is split according to the the electronic state. The two branches of the wavepacket follow different trajectories in phase space but rephase at time $\frac{2\pi}{\delta}$ [38].

The dynamics can be probed with a Ramsey-style experiment on a single ion. First, a $\pi/2$ pulse is applied to the electronic state (perhaps with detuning Δ), generating the superposition state $(|S\rangle + |D\rangle)/\sqrt{(2)}$. Then the bichromatic laser beams are applied generating the Hamiltonian in Equation 3.38 for an interaction time τ. Finally, a second $\pi/2$ pulse is applied to the electronic state, and the D-state probability is measured (i.e. $\langle |D\rangle\langle D| \rangle$).

With the vibrational mode of interest prepared in the ground state of motion, the first $\pi/2$ pulse generates the state $(|S, 0\rangle + |D, 0\rangle)/\sqrt{2}$. With the bichromatic beams turned on, this state evolves to the state $(|S, \alpha(\tau)\rangle + e^{i\Delta t}|D, -\alpha(\tau)\rangle)/\sqrt{2}$. The phase evolution Δ is due to the detuning of the Ramsey pulses from the carrier transition. The second $\pi/2$ pulse yields:

$$\frac{1}{2}\left(|S, \alpha(\tau)\rangle + |D, \alpha(\tau)\rangle + e^{i\Delta\tau}|S, -\alpha(\tau)\rangle - e^{i\Delta\tau}|D, -\alpha(\tau)\rangle\right). \tag{3.42}$$

Measuring the expectation value of the projector $P_D = |D\rangle\langle D|$ gives:

$$\langle P_D \rangle = \frac{1}{4}\left(\langle\alpha(\tau)| - e^{-i\Delta\tau}\langle-\alpha(\tau)|\right)\left(|\alpha(\tau)\rangle - e^{i\Delta\tau}|-\alpha(\tau)\rangle\right) \tag{3.43}$$

$$= \frac{1}{4}\left(2 - e^{-i\Delta\tau}\langle-\alpha(\tau)|\alpha(\tau)\rangle - e^{i\Delta\tau}\langle\alpha(\tau)|-\alpha(\tau)\rangle\right) \tag{3.44}$$

$$= \frac{1}{2}(1 - \cos(\Delta\tau)\langle\alpha(\tau)|-\alpha(\tau)\rangle). \tag{3.45}$$

With the ion initially in the ground state of motion, the experiment is a probe of the overlap between the two branches of the ion's wavefunction with opposite coherent displacements. If the vibrational mode is not initially in the ground state, but rather in a thermal state, the situation is somewhat more complicated. The time evolution operator is still the
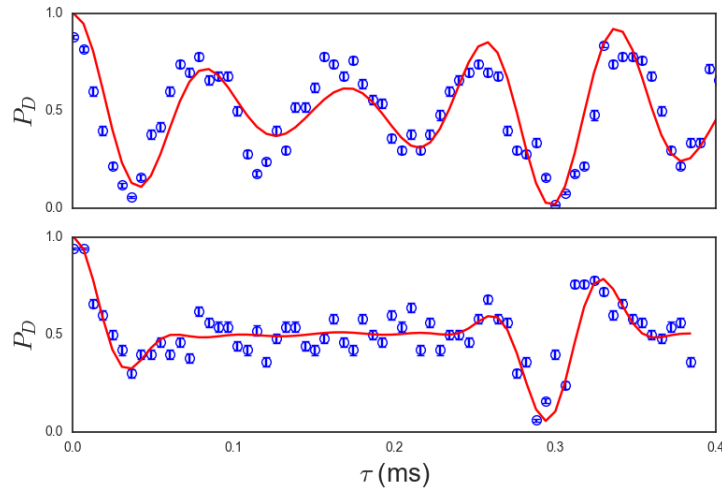
Figure 3.10: D-state probability vs interaction time τ of a Ramsey-style experiment to probe the dynamics of the $\sigma_z x$ interaction (details of the experiment in the main text). Top and bottom plots are for similar experimental parameters, except that the thermal occupation $\bar{n}$ of the ion's vibrational mode is varied. In the top plot, the motion is prepared near the ground state with $\bar{n} = 0.5$. In the bottom graph, the ion is left at the Doppler-cooled value of $\bar{n} = 10$. Solid lines are a fit to a numerical simulation of the experiment where all Hamiltonian parameters are varied. **Top**: $\kappa = 2\pi \times 1.9$ kHz, $\delta = 2\pi \times 3.3$ kHz, $\Delta = 2\pi \times 11.8$ kHz. **Bottom**: $\kappa = 2\pi \times 1.6$ kHz, $\delta = 2\pi \times 3.3$ kHz, $\Delta = 2\pi \times 12.0$ kHz.

one described in Equation 3.41, but the displacement operators act on thermal states. An experimental comparison of these two situations is shown in Fig. 3.10. With the ion prepared near the ground state, the Ramsey signal oscillates at Δ, while slowly losing contrast as the two different paths become more orthogonal. In the second case, the ion's motion is prepared to a mean thermal occupation of $\bar{n} = 10$, and in that case the Ramsey signal is almost immediately dephased. This shows that small coherent displacements of a thermal Harmonic oscillator state yield a nearly orthogonal state. Contrast revivals occur when the motional wavepackets recombine ($\tau = 2\pi/\delta$), at a time independent of the motional state of the oscillator.

Chapter 4

Experimental setup

The experiments described in this thesis took place in different trapping setups. The work in Chapter 5 and Sec. 6.3 took place in a microfabricated surface electrode trap. This experimental setup was built in part by the present author, as well as by Sankaranarayanan Selvarajan and Nikos Daniilidis. The work in Chapter 7 was carried out in a 3D Paul trap, designed and built by Thaned Pruttivarasin and Michael Ramm, and the experimental details for that trap are discussed in their PhD theses.

This Chapter is organized as follows: Secs. 4.1 and 4.2 cover laser and imaging setups which are general to all experiments in the laboratory. Following that are details of the microfabricated trap setup and vacuum chamber (Secs. 4.3 and 4.5). Finally, we discuss experimental improvements to the 3D trap setup, namely the optical layout to implement laser-based quantum gates (Sec. 4.6) and an active feedback loop to stabilize radial trap frequencies (Sec. 4.7).

4.1   Injection locked laser

The performance of high-fidelity quantum operations on an optical qubit requires a narrow-linewidth laser locked to a high-finesse optical cavity. In our case, this is a Toptica DL-Pro laser system, locked to a 10 kHz linewidth cavity from Stable Laser Systems (see [51] for details on this system).

However, the locking process itself generates undesirable features in the frequency spectrum of the laser known as servo bumps. These features result from the laser locking electronics. Essentially, the locking electronics contains contains a low-frequency (less than about 1-2 MHz) control loop with high gain for narrowing the laser linewidth. For noise with low enough frequency, the low frequency control loop operates the laser current and piezo-electric control element in the correct direction to compensate the noise. However, noise around the maximum frequency of the control loop is "corrected" with the wrong phase, in effect amplifying noise. This gives rise to bumps in the laser frequency spectrum, shown in Fig. 4.2.
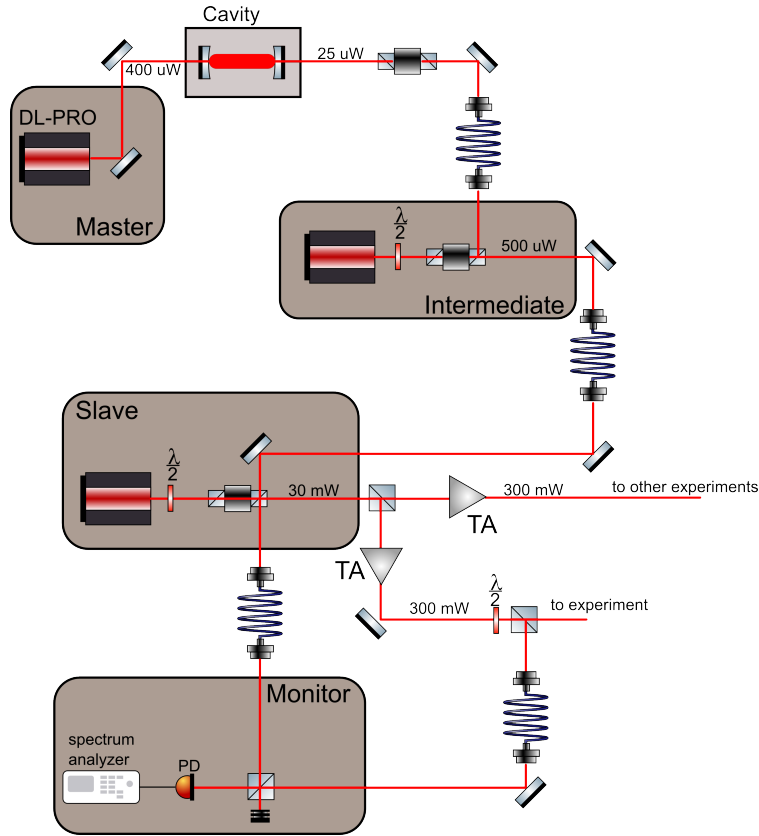
Figure 4.1: Optical layout for the 729 nm laser beams in the laser room. Image made using ComponentLibrary[20].

The servo bumps, around 750 kHz in our case, are located near the motional frequencies of our ions. This means that if the laser is used to address the motional sidebands, the servo bumps will be near the carrier transition, and can cause undesirable spin flips, leading to decoherence.

To put these numbers in context, since our servo bumps are measured to be about 25 dB below the main carrier, the power in each bump is roughly 0.3% of the total laser power. Therefore, if the central peak of the laser will drive carrier Rabi oscillations with frequency Ω, one of the servo bumps will have a Rabi frequency of $\sqrt{0.003}\Omega \approx 0.05\Omega$. For our system, $\eta \approx 0.05$ for all of the modes, and therefore the rate of excitation due to the servo bumps can approach the motional sideband Rabi frequency $\eta\Omega$ if the bump is located directly on the carrier.

In order to remove these bumps, we use a method suggested by the Ozeri group [2]. We use the light *transmitted* through the locking cavity itself as a seed for an injection locked laser diode (Fig. 4.1). This scheme is effective because the locking cavity has a linewidth of about 10 kHz, and therefore the servo bumps should be heavily suppressed in the transmitted

Figure 4.2: Beat signal between laser light from the Toptica DL-PRO, and light transmitted through the locking cavity. The transmitted light is first used to inject a laser diode, amplifying it to 30 mW. The transmitted light is sent through an 80 MHz AOM, and then combined on a beamsplitter with the beam from the DL-PRO, and directed 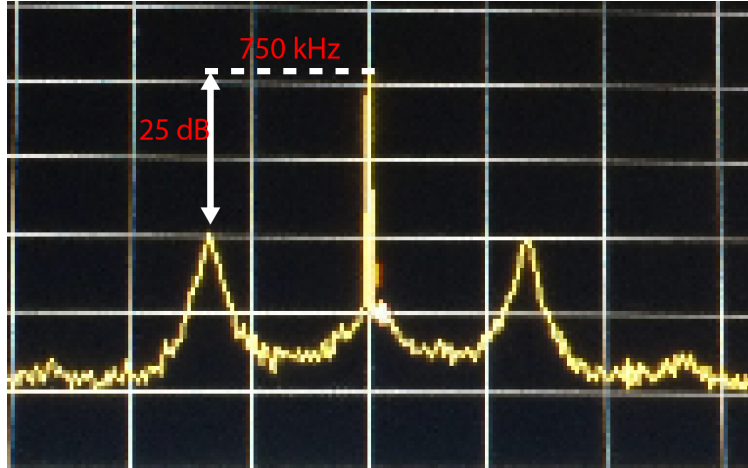on a photodiode. The output of the photodiode is measured on a spectrum analyzer. A narrow peak is seen at the center of the scan–this is where most of the laser power is concentrated. About 25 dB below the main peak, and 750 kHz away, are the broader servo bumps.

light.

Given sufficient seed power, an injection lock can be quite easy to achieve. Essentially, the process works by injecting a seed laser beam with wavelength λ_s into the laser diode. If the free-running wavelength of the diode is close enough to λ_s, the diode will "lock", and begin lasing at λ_s with the full output power of the diode. In practice, this is accomplished by combining the seed beam with the output of the laser diode on the rejected port of an optical isolator. A cylindrical telescope is also used to match the spatial mode of the seed light to the laser diode. The current and temperature of the laser diode is adjusted to make its free-running output as close as possible to the desired frequency.

With about 250 μW of incoming power to the locking cavity, we obtain about 30 μW of transmitted power. At these low seed powers, we found it quite difficult to maintain an injection lock with high output power (30 mW)–we speculate that for high output powers, the injection interval– the current interval $(I_\mathrm{min}, I_\mathrm{max})$ in which the diode will lock to the seed–is quite narrow and small changes in the operating temperature or seed power will cause the diode to fall out of lock. We found it much easier to implement the scheme in two stages: first, the output of the cavity seeds an "intermediate" diode with about 1 mW of output power. This lock is found to be quite stable, and typically does not require adjustment throughout the day.

The output of the "intermediate" diode is then used to seed the slave diode, which produces an output power of about 30 mW. When seeded with the larger power from the

intermediate diode, this lock is also maintained throughout the day.

We have found the most reliable way to monitor the status of both the intermediate and slave injection-locked diodes is to perform a beat measurement. Part of the output of the intermediate diode is sent through an AOM at 80 MHz. The AOM output is then combined on a beamsplitter with the output of the slave diode, and the combined beam is measured on a photodiode. Since the two beams are offset in frequency by 80 MHz, an 80 MHz beat note is measured on a spectrum analyzer. Any additional frequencies in either beam are detected as sidebands around this beat frequency, and the spectral purity of this signal is a good test for whether the injection lock current in either the intermediate or slave diodes needs adjustment.

4.2   Lasers and imaging

All lasers used in the experiments are operated in a separate room (the Laser Room), from the room in which the experiment is running. The light is brought to the experimental optical table by 20 meter optical fibers. This strategy has the strong advantage that the lasers are considerably more stable than if they were in a more highly trafficked location.

The lasers in use in this experiment are all diode lasers. The 397 nm, 866 nm, and 854 nm lasers are locked to temperature controlled reference cavities. The cavity length can be controlled by biasing a piezo attached to one of the cavity mirrors, thereby controlling the laser frequency. The photoionization lasers are free-running. The 729 nm laser is locked to a high finesse optical cavity (linewidth on the order of 10 kHz) provided by Stable Laser Systems. The entire system is discussed in more detail in [51].

The photoionization laser light arrives on the optical table from the laser room and are then overlapped with the 397 nm laser for Doppler cooling before being delivered to the ion trap over a short fiber.

The Doppler cooling and repump light are amplitude and frequency controlled by double pass AOMs. These are driven by DDS frequency sources, which are operated by an FPGA (the "pulser"). This system allows both manual control of the laser frequencies as well as the operation during a pulse sequence. This system was developed by Thaned Pruttivarasin, and discussed in his thesis [51].

The imaging setup is shown in Figure 4.3. The ion fluorescence (397 nm) is collected with an objective lens and focused onto a photomultiplier tube and a CCD camera for ion state detection.

An elegant feature of this imaging setup is the insertion of a dichroic mirror in the optical path which transmits blue light and reflects red light. This allows the 729 nm to be addressed to individual ions by overlapping the laser light with the imaging path.
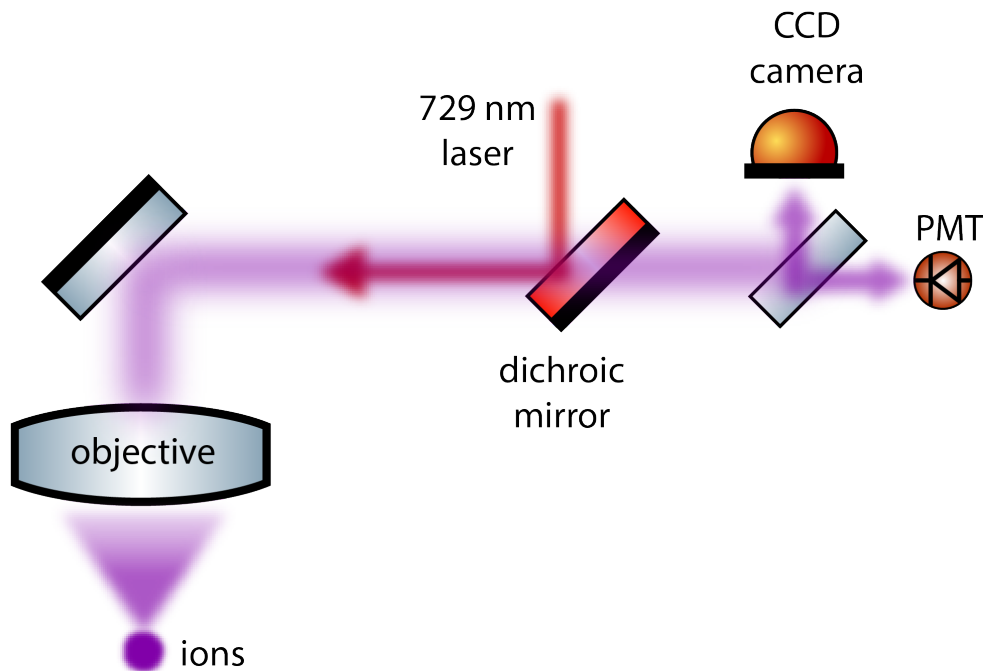
Figure 4.3: Sketch of the imaging system. Image made using ComponentLibrary [20].

4.3 Vacuum system and trap

The experimental system discussed in this chapter centers around microfabricated surface-electrode Paul trap. The trap is mounted in a vacuum chamber[1] which is held at the ultra-high vacuum (UHV) pressure of around 10^{-11} torr. The vacuum apparatus is sketched in Figure 4.4.

Low vacuum pressure is achieved via a combination of methods. All components in the vacuum chamber are meticulously cleaned using isopropanol, acetone, and de-ionized water. The materials are also carefully chosen to have low outgassing rates. After assembly, the chamber is first pumped down to a pressure around 10^{-8} torr via a turbo pump. It is then baked at 150°C for about 2 weeks while connected to the turbo pump. This baking process removes water as well as heavy hydrocarbons such as hand oils from the chamber and continues until the pressure no longer improves as measured on a residual gas analyzer (RGA). After baking, a titanium-sublimation pump (TiSub) is fired several times, which has the effect of absorbing hydrogen in the chamber, which has a low pumping cross section through the turbo pump. Finally, an ion pump is turned on which brings the vacuum pressure down to the final value.

---

[1]Kimball 8" octagon
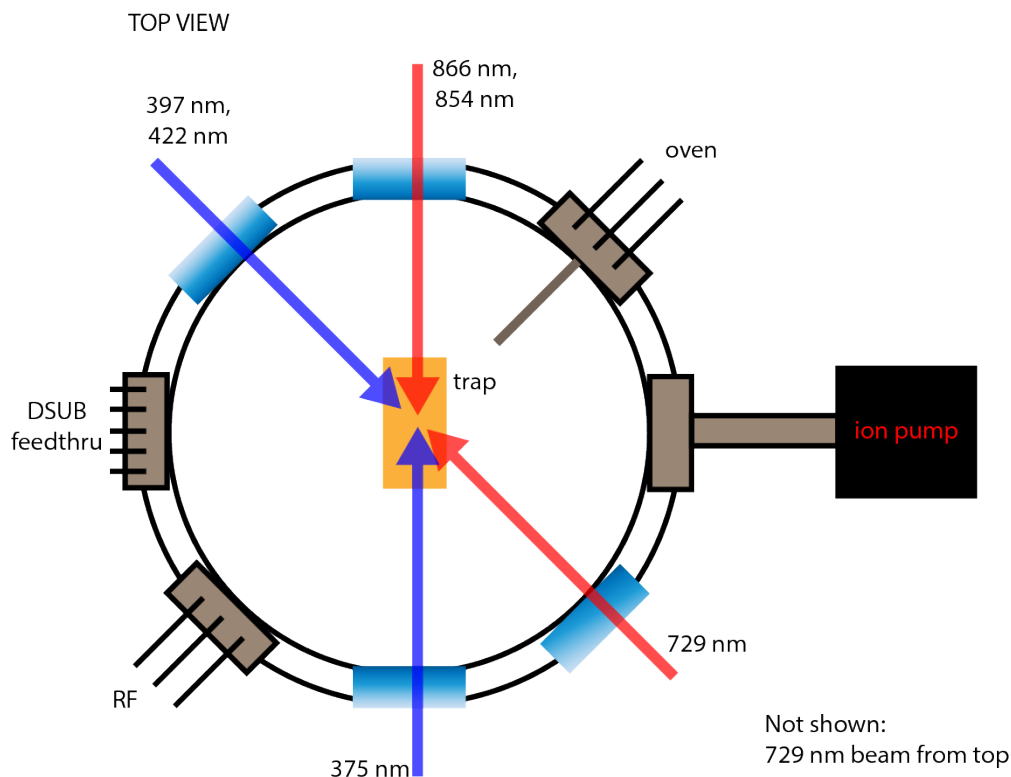
Figure 4.4: Top view diagram of the vacuum chamber plus laser beam paths for the surface trap apparatus. A titanium sublimation pump is not shown because it would appear below the ion pump. The 375 and 422 nm laser beams are for photoionizing neutral calcium produced by the oven. An additional 729 nm beam hitting the trap from the top is also not shown. DC voltages are applied to the trap via the DSUB.

The trap itself is epoxied to a ceramic leadless chip carrier (CLCC) (Figure 4.6). The rf and dc electrodes on the trap are wire bonded to bonding pads on the CLCC. The CLCC is mounted in a ceramic socket machined by Qualmax, with electrical connection between the bonding pads on the CLCC and the socket. The socket sits on an in-vacuum filterboard (Figure 4.5), and is electrically connected to the filterboard via Fuzz Buttons, manufactured by Custom Interconnects.

All electrical connections (rf and dc) from outside the chamber to the trap go through the in-vacuum filterboard. These connections are made via copper wires running from electrical feedthroughs to soldering points on the filterboard. The DC lines on the filterboard are filtered with low-pass filters to reduce electrical noise on the trap electrodes [2].

---

[2]AVX X7R 47nF; Part No. W3H15C4738AT1F, with a measured cutoff frequency of 300 kHz
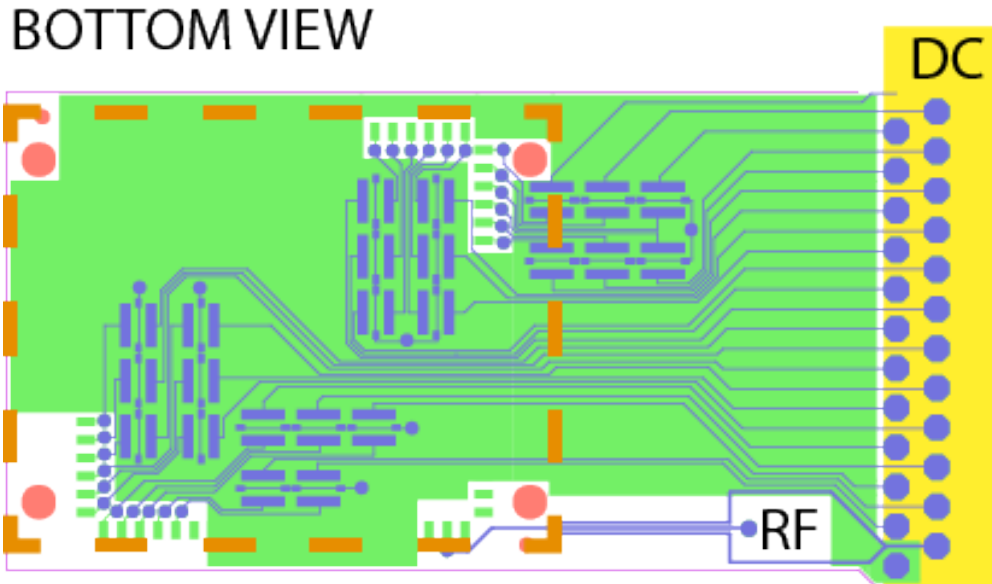
Figure 4.5: Schematic of the in-vacuum filterboard on which the trap is mounted. The dc lines are filtered with monolithic low-pass filters with a low-frequency cutoff of 300 kHz. The socket is mounted on the reverse side of the board, and sits approximately on the orange dashed square. The dc and rf connections from outside the chamber arrive from copper wires soldered onto the filterboard. The board is made from alumina to minimize rf losses in the dielectric. The solder is lead-free and flux-free so as to have favorable outgassing properties and has the chemical composition Sn 96.5%, Ag 3%, Cu 0.5%.

4.4 DC electronics

This section pertains only to Chapter 5 and Sec. 6.3. However, the system described here is currently in use in all the surface-trap experiments in the lab.

For controlling the voltages on the dc electrodes for the trap, we use a multi-stage system sketched in Figure 4.7.

Voltage sets are specified by a computer which communicates via USB to a field-programmable-gate-array (FPGA)[3] called the controller board. The computer writes instructions to the controller board in the form of

```
write (BITSTRING) to DAC (number) in voltage set (number)
```

where `BITSTRING` is a 16-bit binary string encoding the desired output voltage. The voltages on the DAC board will be immediately updated if the voltage set-number is zero, but sets of voltages can also be stored in the DAC board. The DAC board advances through stored voltage sets on a TTL trigger.

---

[3]Opal Kelly XEM3001

socket   CLCC

Figure 4.6:   Trap-holding CLCC and socket.

Figure 4.7: Schematic overview of the dc electrode control system.

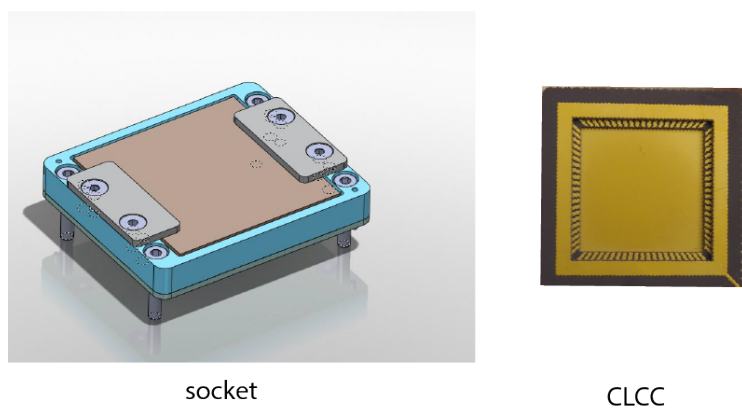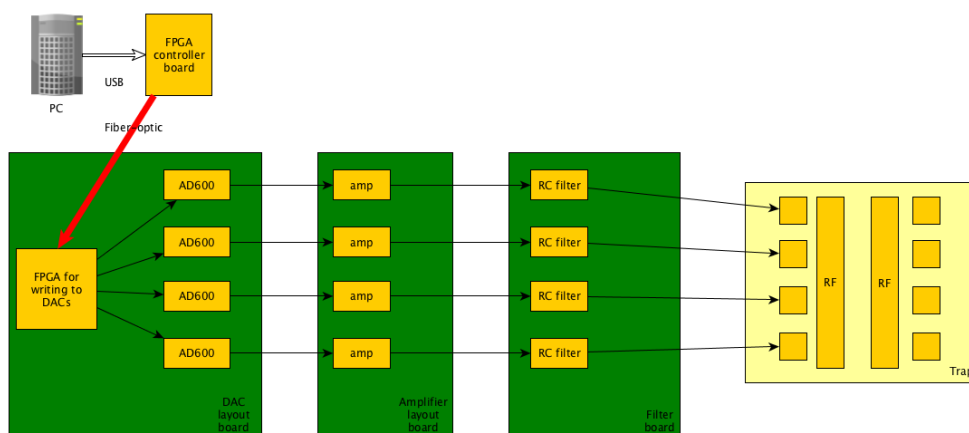In order to prevent ground loops, as well as to electrically isolate the trap voltages from the (electrically noisy) computer, the controller board communicates with the DAC board over fiber optic cables.

The DAC board functionally consists of three main components: power supplies, DAC chips[4], and FPGAs[5] for receiving voltage sets from the controller and writing serial bitstrings to the DAC chips themselves. The on-board FPGA receives instructions from the controller board via the fiber-optic connections.

The DAC voltages are amplified with a gain of 4 by low noise operational amplifiers[6]. Coupled with the amplifiers, each dc electrode is controllable to ± 40 V with 16 bits of precision.

The trap electrodes are electrically connected outside the vacuum chamber through a DSUB feedthrough. Immediately before the feedthrough, each DC channel is filtered with a dual stage RC filter[7] to mitigate electrical noise near the ion motional frequencies.

4.5   Radio-frequency electronics

For reasonable experimental parameters, one needs to apply around 100 V of rf amplitude at a frequency near 30 MHz. The electrical load of the trap and associated circuitry (feedthrough, CLCC, etc.), is primarily capacitive with approximately 30 pF of capacitance. It is infeasible to drive this electrical load directly with a 50Ω output due to both reflections as well as the large power required.

Instead, we use a quarter-wave helical coil resonator to match the impedance between the driving circuit and the trap (Figure 4.8). This resonator consists of a copper coil mounted inside a copper tube, with one end of the coil grounded to the tube. The inductance of the coil, coupled with the self capacitance of the coil, the capacitance of the coil to the tube, and the parallel capacitance of the trap together form an LC resonator. By tuning the number of turns in the coil, the resonance frequency of the circuit can be selected. Using this method, we are able to apply the needed voltage for trapping with less than 1 W of input power.

The rf signal is generated by a Rhode and Schwarz signal generator, and then amplified by a 5W MiniCircuits rf amplifier.

The resonator is excited inductively through the use of an antenna coil, following [64]. This allows the trap ground to be electrically isolated at low frequencies from the amplifier and signal generator, preventing ground loops.

The output of the coil may be dc biased over a capacitor (Fig. 4.8). From the perspective of the ion, this adds a dc potential in addition to the rf pseudopotential. This can be used to increase trap depth, lift the degeneracy between the ion radial frequencies, as well as

---

[4] Analog Devices AD600

[5] Altera Cyclone II

[6] Texas Instruments OPA445

[7] R = 1 kΩ, C = 100 nF, giving a filter cutoff of 1.6 kHz
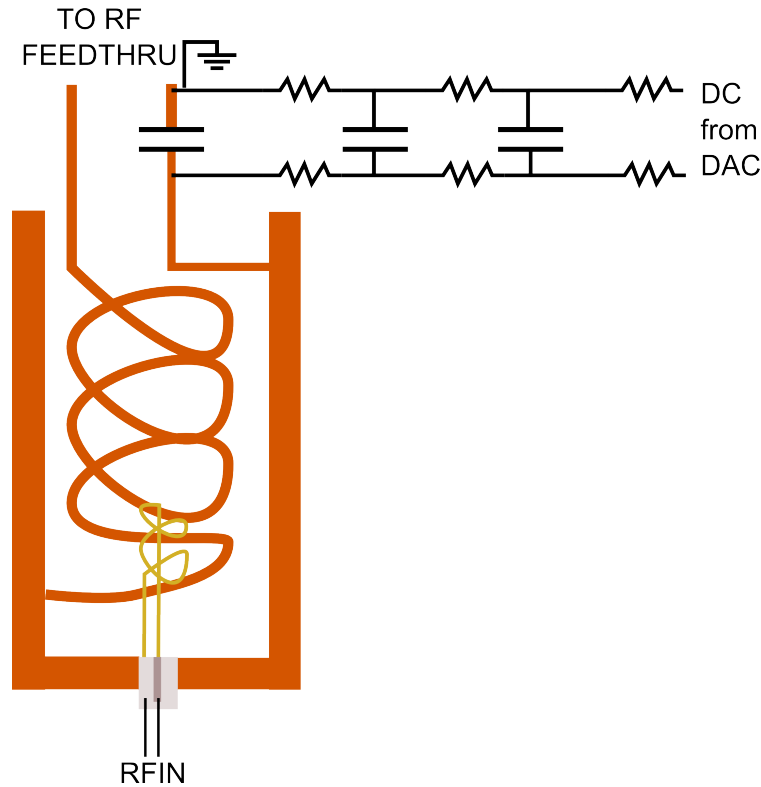
Figure 4.8: Resonator plus dc-biasing circuit. The resonator is inductively excited via the antenna coil (gold), which is connected to the resonator can by a ground-isolated BNC. The antenna coil is driven by a Rhode and Schwarz rf signal generator. The input impedance of the resonator is matched to 50Ω by adjusting the position and number of turns of the antenna. The output of the rf resonator may be dc-biased by applying a dc voltage where indicated. The dc voltage is low-pass filtered both to suppress noise from the voltage source as well as to prevent rf currents from flowing into the voltage source, potentially causing dc voltage instabilities. The resistor and capacitor values are R = 1 kΩ and C = 100 nF giving a cutoff frequency of 1.5 kHz. The output leads of the resonator are soldered directly to the rf feedthrough on the vacuum chamber, which connect to the trap rf electrodes and ground plane.

to rotate the normal mode orientation of the trap into alignment with the rf quadrupole direction.

4.6 Optical layout for laser-based gates

The most complicated optical setup we use is for the 729 nm laser. This setup is designed to accommodate several needs. First, it is useful to have two independently controllable beams
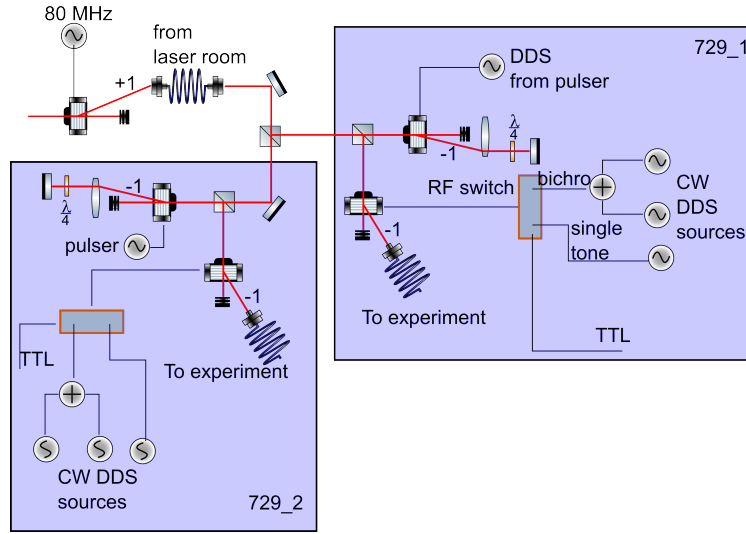
Figure 4.9: Optical layout for the 729 nm laser beams on the experimental table. Image made using ComponentLibrary [20].

(e.g. for addressing different ions in a chain, or the same ion from different directions). Secondly, for generating quantum gates such as those described in Sec. 3.6, it is necessary imprint two frequencies on the laser beam.

In our system, the laser light from laser room is split into two functionally identical paths. In each path, the frequency, phase, and amplitude of the laser beam is set by a double pass AOM (near 220 MHz), controlled by the pulser.

After the double pass, the beam goes through a single pass AOM (center frequency 80 MHz). The single pass is operated in a somewhat complicated way. Each single pass AOM requires three DDS frequency sources which run in a continuous-wave (CW) mode with a pre-programmed frequency (i.e., programmed before the pulse sequence begins). Two of the frequency sources are combined on a power splitter, the output of which is a bichromatic rf signal. The bichromatic signal is combined on a MiniCircuits rf switch with a third frequency source running at 80 MHz. The rf switch is TTL controllable, which switches the AOM between monochromatic and bichromatic operation. However, full rf power is always arriving at the AOM, and therefore in order to turn off the laser beam going to the ion, the double pass must be switched off.

In order to compensate the $\sim$ -80 MHz frequency shift due to the single pass AOMs, an additional AOM is placed in the laser room and driven with a Rhode and Schwarz signal generator at 80 MHz. This AOM is additionally used to dynamically stabilize the power arriving at the laser table, and in the future can also be used for fiber noise cancellation.

Figure 4.10: rf circuit and feedback elements for the 3D trap. The out of phase outputs of the resonator (in orange box) are measured on capacitive dividers labeled mon1 and mon2. The difference voltage between mon1 and mon2 is rectified and subtracted from a setpoint, producing the quasi-DC signal V_{err}. A PID feeds back to the signal generator modulation input to stabilize V_{err} to zero.
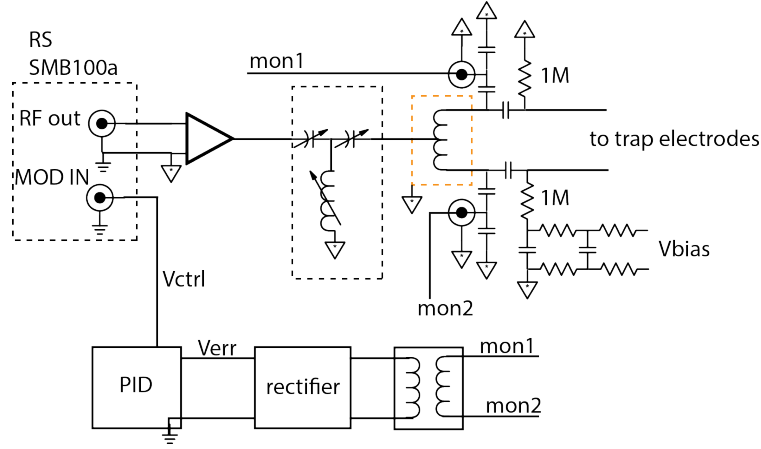
4.7 Radio-frequency amplitude stabilizer

For the quantum simulation experiments discussed in Chapter 7, it was necessary to achieve radial frequency stabilities of better than 500 Hz. As the ion radial frequencies depend on the rf amplitude arriving at the trap, fluctuations in the rf amplitude result in trap frequency fluctuations. With a free-running resonator, the trap frequency has long-term drifts, due in part to temperature changes in the amplifier, and short-term fluctuations due to a number of effects such as mechanical vibrations of the resonator, or changes in the resonator's natural frequency due to people moving around the experimental apparatus. Without active stabilization, the ion's radial frequencies move around by several kHz on both short (seconds to minutes) and long (hours) timescales.

These electronics were developed specifically for the 3D trap, which uses a different kind of resonator than the one discussed in Sec. 4.5. In this case, the resonator is a half wave resonator which is excited in the center of the coil. The rf electrodes on the trap are driven 180° out of phase. See [51] for details. The system, including feedback electronics, is shown schematically in Fig. 4.10.

Our approach is to directly measure the rf amplitude via a rectifier, and use a PID controller to feedback on the input power to the resonator. The rf amplitude is measured on both outputs of the resonator by a capacitive divider which prevents the measurement circuit from excessively loading the resonator. The two capacitive divider outputs are labeled "mon1" and "mon2". The rectifier (box labeled "rectifier" in Fig. 4.10, developed mainly by Eli Megidish and Soenke Moller, actually consists of two functional components. First, the input signal is passively rectified to a DC amplitude with high-frequency diodes. The
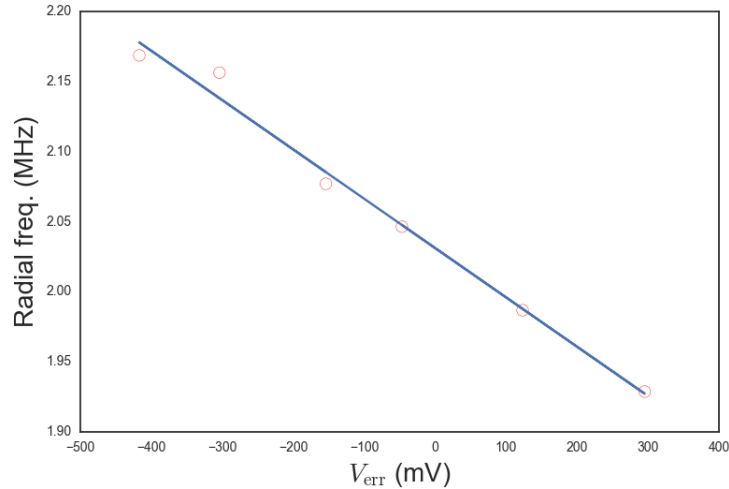
Figure 4.11: Measured radial trap frequency vs. rf detector error signal. Line is a fit showing a sensitivity of 352 Hz/mV.

rectified signal is then subtracted from a setpoint so that the DC output of the rectifier circuit is actually an error signal V_{err}. A PID controller stabilizes V_{err} to zero by feeding back to the amplitude modulation of the signal generator. A similar approach was recently demonstrated by the Monroe group [37].

The sensitivity of the detection circuit is characterized in Fig. 4.11. By disabling the feedback, we varied the rf generator power around the operating point and measured both the radial frequency of a trapped ion as well as the error signal V_{err} produced by the the rectifier circuit. The measured sensitivity is 352 Hz/mV. At the moment, we aim for long-term trap frequency stability on the order of 200 Hz, and therefore the error signal must be stabilized to about 1 mV. Experience suggests that it is probably reasonable to reach error signal stabilities somewhere in the range of 100 μV–roughly suggesting that this method can be expected to achieve trap frequency stabilities on the order of 35 Hz out of 2 MHz. Of course, achieving this level of stability on very long (hours) timescales would be quite challenging, due to temperature sensitivity of the capacitive divider and rectifier circuits, as well as long-term drifts of the voltage reference.

The trap frequency stability is measured by a pulsed-excitation experiment, described in Section 3.6. The trap frequency stability is probed in two ways. The first way is spectroscopically (See Fig. 4.12). In such a measurement, the ion is Doppler cooled, and a coherent displacement is applied to the motion. The coherent displacement arises from a train of 397 nm laser pulses with a repetition rate f_{ex} near the trap frequency, producing a modulated radiation pressure force (see Sec. 3.6). After this, a 729 nm laser pulse is applied to the blue motional sideband, followed by electron shelving readout probing the D-state excitation probability. The duration of the 729 nm laser pulse must be significantly shorter than $1/(\eta Omega)$, so that when the oscillator is not displaced, the D-state excitation probability
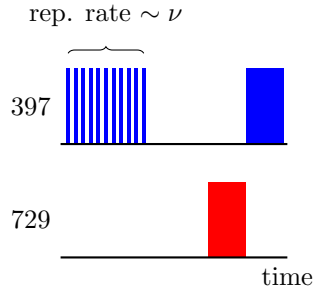
Figure 4.12: Schematic pulse sequence for trap frequency measurement. A pulse train of 397 nm light has a repetition rate near the ion's motional frequency, effecting a coherent displacement of the ion's motion. After the pulse train, a 729 nm pulse is applied to the blue sideband, followed by electron shelving readout. When the repetition rate is resonant to the trap frequency, the sideband Rabi frequency increases dramatically, causing a peak in the D-state population after readout.

is small. When the pulse-train repetition rate is resonant to the motional frequency, however, the sideband Rabi frequency increases, causing the excitation probability to also increase. Repeating this measurement for different values of f_{ex} shows an excitation peak near the motional frequency. Repeating this measurement over the course of tens of minutes monitors long timescale changes in the vibrational frequency. The result of such a measurement is shown in Fig. 4.13.

The second measurement is Ramsey-style probe to measure short-term coherence (See Fig 4.14). This method is similar to the previous spectroscopic measurement except two pulse trains are applied, separated by an interrogation time τ. The repetition rate f_{ex} is detuned slightly (about 2 kHz) from the radial trap frequency ($2\pi \times 2.1$ MHz). As long as the ion's phase evolution is phase-coherent over the time τ, the resulting displacement amplitude will oscillate sinusoidally as the phase between the ion's motion and the repetition rate evolves. However, as the phase of the ion's motion becomes randomized due to trap frequency fluctuations, the oscillations dephase. The damping time of the oscillatory signal (Fig. 4.15) measures the phase coherence time of the ion motion. A theoretical treatment of how trap frequency fluctuations appear in this measurement is given in Sec. 6.1.
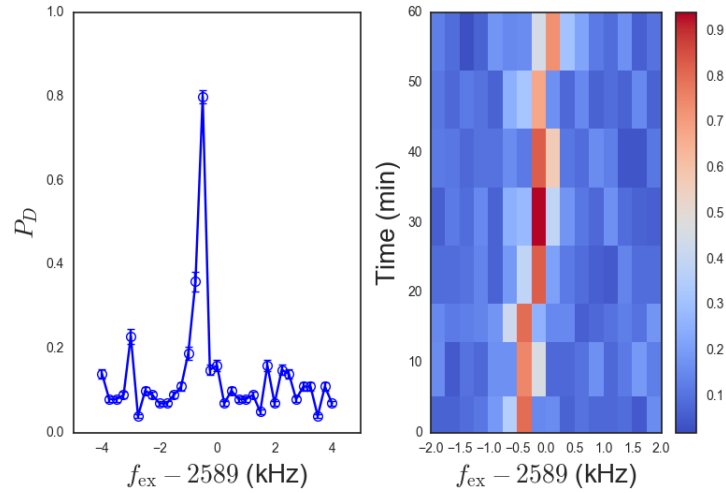
Figure 4.13: **Left**: D-state excitation probability as a function of the coherent excitation frequency. It is strongly peaked when the coherent excitation is resonant. In this case, the radial frequency was about $2\pi \times 2.6$ MHz. **Right**: A compilation of spectral measurements taken over an hour. We see a slow drift of at most 500 Hz in the ion's radial frequency over this period.
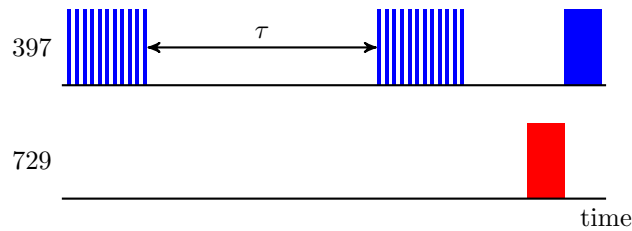
Figure 4.14: Ramsey-style probe for motional coherence. Two pulse trains of 397 nm light, each effecting a coherent motional displacement, are separated by an interrogation time τ. After the two displacement operations, a 729 nm laser pulse is applied to the blue sideband, followed by electron shelving state readout.
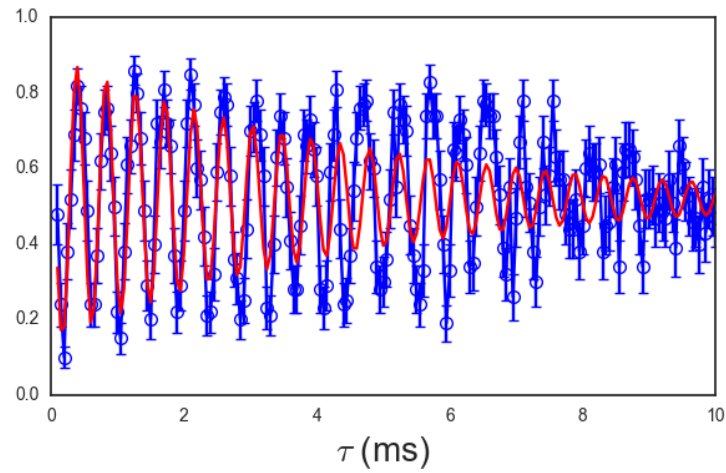
Figure 4.15: Short-term coherence probe of the ion's radial motion. The coherence is measured by a Ramsey-style coherent displacement measurement (described in the main text). The x-axis is the Ramsey interrogation time, in ms. The red line is a fit of the data to a cosine with a decaying exponential, with a decay time constant about 5 ms. This measurement shows that with the stabilizer running, the phase coherence of the ion's motion is preserved on this timescale.

Chapter 5

Parametric coupling

5.1 Introduction

This work describes experimental work first published in Ref. [23] and closely follows that treatment.

A single trapped ion oscillates with three normal vibrational frequencies. Each different mode of oscillation corresponds to a displacement of the ion along a particular vector that I will call the *mode vector*.

In order to do perform many useful operations involving spin-motion coupling–such as sideband cooling, temperature measurement, or even quantum gates, it is necessary for the laser to have substantial projection onto the mode vector. In general, the coupling strength of the laser to the spin-motion transitions is proportional to $\cos(\theta)$, and θ is the angle between the laser wave-vector and the mode vector (see Sec. 3.3). The need for the laser wave-vector to have appreciable projection onto the mode of interest imposes substantial experimental constraints regarding optical access. For instance, in a surface trap, it may be the case that a particular mode vector is oriented nearly vertically with respect to the trap surface. To avoid charging effects [4], it may be desirable to avoid having laser light directly impinge on the trap surface. In order to avoid this, the laser must propagate nearly parallel to the trap and one is then limited to a quite small overlap between the wave vector and the mode vector–making it difficult to interrogate this mode.

This problem may be partially overcome by rotating the normal modes such that the laser has significant projection onto each mode. However, this itself constrains the design of the trap electrodes so that the number and shape of the electrodes is sufficient to perform the desired rotation.

In this Chapter, I describe a parametric coupling scheme which evades these requirements. This scheme allows experimental access to any vibrational mode of a single ion without direct optical interaction. This is done by applying an oscillating voltage to trap electrodes such that the associated field at the trapping position features a spatial variation enabling the coupling. Tuning the oscillation frequency resonant to the frequency difference

between two modes causes the modes to exchange energy. This allows optical interrogation of an inaccessible mode by first coupling it to another, optically accessible mode. A similar technique has been demonstrated in Penning traps[72, 12].

5.2   Theory of interaction

Under consideration is an ion with charge q and mass m, confined in a linear surface electrode rf Paul trap. In such a trap, an oscillating voltage with frequency in the range of $2\pi \times 30$ MHz will be applied to two electrodes (labeled "RF" in Fig.   5.1) providing two-dimensional confinement along the x and y axes with pseudopotential frequencies ω_x and ω_y. In this case the rf pseudopotential generates no confinement in a third direction, z. The confinement in the z direction is the result of a dc potential which is quadratically varying in space, giving the ion a third motional frequency ω_z.
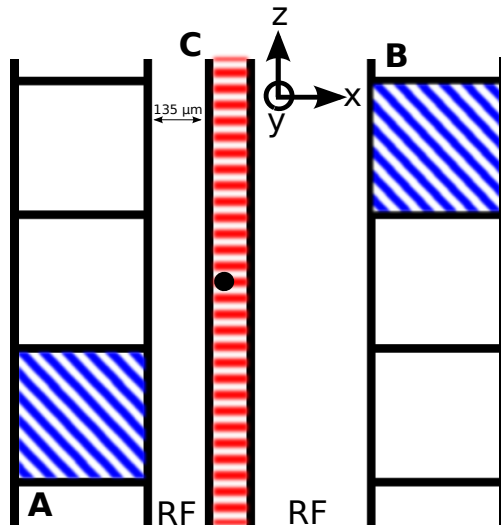
Figure 5.1: Illustration of the surface trap where the ion's position is represented by the black dot. When the experiment is operated in the xz coupling configuration, the rf parametric drive is applied to the electrodes labeled A and B (blue diagonal shading). When operated in the xy coupling configuration, the drive is applied to the electrode labeled C (red horizontal shading). Figure first published in [23].

Working in the aforementioned approximation, we consider a harmonically confined ion with motional frequencies ω_i, $i \in \{x, y, z\}$. The interaction energy created when a voltage u is applied to a nearby coupling electrode is $qphi(\mathbf{r})u$. $\phi(\mathbf{r})$ is the dimensionless spatial profile of the potential at the trapping position due to the coupling electrode. To enable the mode-mode coupling, we modulate the voltage on a set of electrodes whose spatial profile mixes two of the ion's normal vibrational modes.

Then the Hamiltonian governing the motion is $H = H_{\text{osc}} + q\phi(\mathbf{r})u$, with $H_{\text{osc}} = \hbar \sum_i \omega_i a_i^\dagger a_i$ being the harmonic oscillator Hamiltonian and a_i ($a_i^\dagger$) is the annihilation (creation) operator for mode i. To achieve mode-mode coupling, we apply an oscillating radio-frequency (rf) voltage on a judiciously chosen set of coupling electrodes such that $u = u_0 \cos(\omega_p t)$. If $\omega_p = \omega_i - \omega_j$, the difference frequency between modes i and j, a parametric coupling emerges in the Hamiltonian.

To see the coupling explicitly, $\phi(\mathbf{r})$ is expanded to second order as $\phi(\mathbf{r}) = \phi(0) + \sum_i (r_i/D_{1,i}) + (1/2)\sum_{i,j}(\pm)(r_i r_j)/D_{ij}^2$. The D's are the expansion coefficients The linear terms create an electric field at the ion position and present a driving force on the ion which introduces a driven motion analogous to micro-motion. As we will show later, this additional term does not alter the coupling dynamics and thus can be neglected if the set of coupling electrodes are chosen such that the coupling dominates over this driving force.

The terms proportional to r_i^2 modify the motional frequencies of the ion. If the modulation frequency is near the resonance condition $\omega_p \approx 2\omega_i$, these terms effect a parametric amplification of the energy in the ω_i mode [46]. However, if ω_p is far from this condition (as will be the case in our experiments), the modulation of the trap frequency contributes only an overall phase to the ion's spatial wavefunction. Finally, the cross terms proportional to $r_i r_j$ are responsible for the parametric coupling with the drive frequency chosen to be $\omega_i - \omega_j$.

In the interaction picture, the Hamiltonian becomes

$$H_I = qu_0 \cos(\omega_p t) \sum_{i,j} \left(\frac{r_i r_j}{2D_{ij}^2} \right)$$

$$= qu_0 \hbar \cos(\omega_p t) \sum_{ij} \frac{e^{i(\omega_i + \omega_j)t} a_i^\dagger a_j^\dagger + e^{i(\omega_i - \omega_j)t} a_i^\dagger a_j + \text{H.c.}}{4m\sqrt{\omega_i \omega_j} D_{ij}^2}$$

$$= \hbar \cos(\omega_p t) \sum_{ij} g_{ij} \left(e^{i(\omega_i + \omega_j)t} a_i^\dagger a_j^\dagger + e^{i(\omega_i - \omega_j)t} a_i^\dagger a_j + \text{H.c.} \right) \tag{5.1}$$

where H.c. indicates Hermitian conjugation. In the last line we have absorbed all the constants except $\hbar$ into the coupling constant g_{ij}. In general, we expect the rotating wave approximation (RWA) to be valid whenever $g_{ij} \ll \omega_{i,j}$.

If $\omega_p = \omega_i - \omega_j$ and applying the RWA, all the terms in the sum of Eq. 5.1 vanish except the one involving coupling oscillators i and j leading to

$$H_I \approx \hbar g_{ij}(a_i a_j^\dagger + a_i^\dagger a_j) . \tag{5.2}$$

This is precisely the interaction we have sought to create: it will swap the quantum states between oscillator modes i and j at a frequency g_{ij}. By applying the parametric drive for a specific duration, we can controllably induce state swapping between any two modes of the single ion oscillator.

When the parametric drive is operated on resonance, that is, $\omega_p = \omega_i - \omega_j$, the interaction picture Hamiltonian is diagonal in the basis of two modified normal modes given by $\frac{1}{\sqrt{2}}(a_i \pm$

a_j). The modes are split in frequency by $2g_{ij}$. If the drive is detuned by Δ from the parametric resonance, the form of the interaction picture Hamiltonian changes. To treat this problem, it is easiest to transform to a particular interaction picture in which:

$$H_I \approx \hbar \frac{\Delta}{2}(a_i^\dagger a_i - a_j^\dagger a_j) + \hbar g_{ij}(a_i a_j^\dagger + a_i^\dagger a_j) \ . \tag{5.3}$$

The eigenvalue splitting of this Hamiltonian is given by $2\sqrt{g_{ij}^2 + 4\Delta^2}$. Thus, optical spectroscopy of the ion motion will show the bare resonance at ω_i split into two lines as the parametric drive is operated near resonance. Varying both laser frequency and the parametric drive detuning will show a familiar avoided crossing behavior, providing a witness of the parametric interaction.

5.3   Experimental implementation

For the experiments, a single $^{40}\mathrm{Ca}^+$ ion is trapped about 100 μm above the surface of a micro fabricated surface electrode rf Paul trap, where sideband-cooling and analysis of the motional state is performed on the metastable $4^2S_{1/2} \leftrightarrow 3^2D_{5/2}$ transition, as discussed in Sec. 3.4. The ion has three motional modes, with axes nearly parallel to the Cartesian axes defined in Fig. 5.1. The motional frequencies along these three axes are about $(\omega_x, \omega_y, \omega_z) \approx 2\pi \times (2.6, 2.9, 1.0)$ MHz. Sideband cooling and state manipulation is accomplished with a laser in the $x-z$ plane, with about $45°$ projection onto both the x and z axes. The projection of the wave-vector onto the y axis is $9°$, making the Y motional mode difficult to analyze directly. Owing to the small coupling strength of the laser onto the Y mode, sideband cooling close to the ground state can only be performed on the X and Z modes.

Depending on which modes ought to be coupled, the field needs to be applied to a set of electrodes maximizing the coupling term while keeping the linear terms sufficiently small that the associated electric fields do not produce excessive heating of any modes. As discussed later in this Chapter, if the coupling field is applied continuously, the electric fields effect a coherent driving force on the ion motion. However, if the coupling field is applied for a finite time, the driving force will have frequency components resonant to the ion's motion, thereby directly adding energy to the ion's motion.

Throughout this Chapter we use two configurations that couple either the X and Y modes or the X and Z modes. For the first (xy) configuration we simply apply the coupling voltage to the electrode marked C in Fig 5.1. In the case of the xz configuration, driving a single electrode is not sufficient as it would result in excessive driving force on the ion. Therefore, we aim to apply voltages with ratio of 1:4 to electrodes A and B, which constitutes the optimal configuration when being constrained to driving two electrodes in phase.

Each experiment begins with with Doppler cooling on the $4^2S_{1/2} \leftrightarrow 4^2P_{1/2}$ transition and optical pumping into the $m_s = -1/2$ state, followed by a fixed length coherent excitation pulse and electron shelving state readout (Sec. 3.5). The Doppler cooling stage prepares the Z mode to a mean occupation of ≈ 20 vibrational quanta, and the X mode to ≈ 6 quanta.

The spectroscopy is carried out on the $|L, m_J\rangle = |S, -1/2\rangle \rightarrow |D, -1/2\rangle$ transition. The state of the motional mode i is probed by evaluating the strength of the sidebands of this transition detuned by $\pm\omega_i$, as in Sec. 3.4.

The parametric interaction is studied in two ways. It is first characterized by operating it in *continuous-wave* (CW) mode. In this mode, the drive is active throughout the experiments and the spectroscopic signatures of coupling are observed. It is also operated in *pulsed mode* where the coupling field is switched on for a fixed time after the initial state preparation giving access to the time dynamics of the coupling process.

Characterizing the interaction

The experimentally simplest way to investigate the parametric interaction is to first operate it in CW mode near the parametric resonance condition. Then, laser spectroscopy near one of the secular sidebands (indexed by i or j) will show two Lorentzian lineshapes split in frequency space by $2\sqrt{g_{ij}^2 + 4\Delta^2}$, where Δ is the detuning of the parametric drive from the resonance condition.
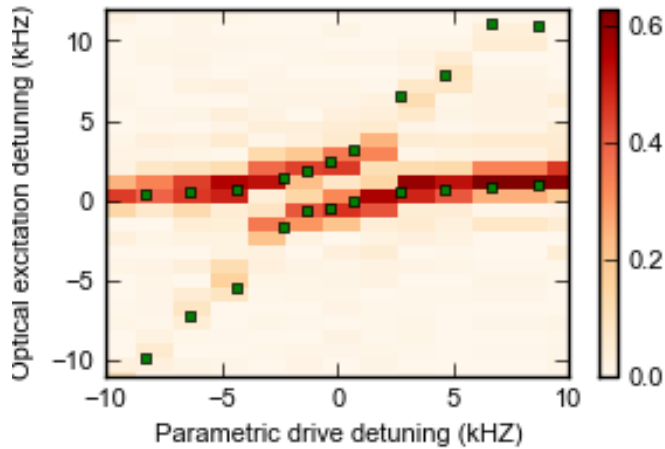
Figure 5.2: Measured energy spectrum of the X radial sideband illustrating the avoided crossing as a function of the detuning of the parametric drive. The green rectangles represent the mean values of Lorentzian fits to determine the frequency splitting. Figure first published in [23].

By measuring the spectrum around the sideband transition for several drive frequencies ω_p, the precise resonance frequency and the coupling strength can be determined from the avoided crossing as shown in Fig. 5.2. At parametric resonance, the line splitting features a minimum, and the coupling strength equals half the on-resonance splitting.

The coupling strength is limited by the maximum voltage that can be applied to the coupling electrodes which are heavily filtered by in-vacuum low-pass filters to suppress heating from technical noise sources. Nevertheless, we have been able to achieve coupling frequencies approaching $2\pi \times 10$ kHz for both xz and xy coupling configurations.

The driven motion amplitude may be quantified by operating the parametric drive in a continuous-wave mode. Then, the oscillating electric field at the ion position results in driven motion, analogous to the well-known micro-motion [73]. This driven motion causes the ion to experience a frequency modulated laser field, redistributing the laser power in frequency space and reducing the laser power at the resonant frequency. This effect gives rise to sidebands around the laser's carrier frequency at integer multiples of the driven motion frequency. For a continuous wave coupling field, the effect is completely analogous to micro-motion leading to a reduced coupling strength on the resonant optical transition which can be observed by a decrease in the Rabi frequency Ω_c. As in the case of micro-motion, the optical transition can be driven by detuning the laser by an integer multiple n of the driving electric field frequency. In that case, the transition strength is given by [6]

$$\Omega_c \to |J_n(kA)|\Omega_c \tag{5.4}$$

for a given oscillation amplitude A along the laser propagation direction $\vec{k}$ and J_n being the n-th order Bessel function of the first kind. We note that if the laser is not detuned, i.e. is on resonance with the optical transition, the coupling strength is reduced by $J_0(kA)$.

To measure this effect, we apply a continuous drive (off resonant from all the motional modes and first order parametric resonances) onto the coupling electrodes and measure the frequency of Rabi oscillations on the $|L, m_J\rangle = |S, -1/2\rangle \to |D, -1/2\rangle$ transition. From this, we can extract the driven motion amplitude as a function of the parametric drive amplitude from Eq. 5.4. Fig. [5.3]. shows the normalized Rabi frequencies on the carrier and the driven motion sideband as a function of the coupling strength for the xz coupling configuration where $\omega_p = 2\pi \times 1.7$ MHz. This allows us to determine the ratio of driven motion amplitude to the coupling strength to be $A/g_{xz} = 497(8)\text{nm}/(2\pi \times 1\text{kHz})$.

In the xy configuration, the drive is applied to an electrode directly beneath the ion so that most of the driven motion is in the direction orthogonal to the laser and therefore does not significantly affect the optical coupling strength.

Pulsed mode operation of the drive

In the remainder of this work, we will investigate parametric coupling in the pulsed mode. If the parametric drive is switched on and off rapidly, the micro-motion analogy of Eq. 5.4 no longer holds, and the unwanted electric field can induce considerable off-resonant excitation in the oscillator modes, disturbing the coupling dynamics. However, this electric field contribution to the total Hamiltonian has no notable influence on the coupling dynamics if it is switched on and off slowly enough, i.e. it is adiabatic. Here, the criterion for adiabaticity is to avoid off-resonant excitation of the oscillator mode itself. Experimentally, we shape the
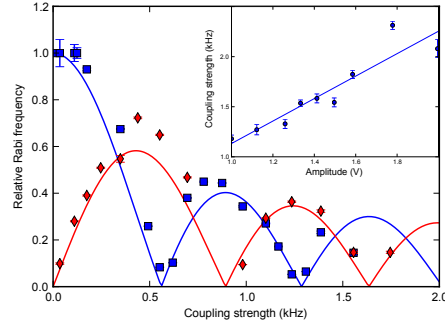
Figure 5.3: Relative Rabi frequency frequency on the carrier (blue squares) and driven motion sideband (red diamonds), compared to the unperturbed Rabi frequency on the unperturbed carrier, as a function of parametric coupling strength in the xz coupling configuration. The solid lines represent fitted Bessel functions of the first kind. The inset illustrates the parametric coupling strength g_{xz} as a function of drive voltage amplitude prior to the in-vacuum low pass filters. Figure first published in [23].

coupling field strength with a Blackman windowing function, which has proven to effectively reduce off-resonant excitation in a two-level system [25, 55]. More precisely, the window for a pulse with duration T is described by

$$B_T(t) = \frac{1 - \alpha}{2} - \frac{1}{2}\cos\left(2\pi\frac{t}{T}\right) + \frac{\alpha}{2}\cos\left(4\pi\frac{t}{T}\right)$$

where $\alpha = 0.16$. In order to facilitate the comparison to rectangular pulses, the coupling duration of a Blackman shaped pulse B_T is defined as the duration of a rectangular pulse T_{rect} with the same pulse area so that $T = T_{\text{rect}}/0.42$. Experimentally, using these pulses for the xz configuration reduces the off-resonant excitation to less than 0.3 quanta for a reasonable coupling strength of several kHz.

5.4 Population swapping

The first analysis in pulsed mode is to demonstrate that population can be exchanged between two motional modes. This will serve as an experimental definition of the exchange operation (SWAP), and form the cornerstone for the cooling and analysis techniques presented later. To facilitate optical analysis of both involved motional modes, we focus here on population swapping in the xz configuration, but note that one can construct a SWAP operation between any two modes and show as an example swapping in the xy configuration.

To demonstrate population swapping, a single mode was sideband cooled close to its ground state. For the xz configuration, the Z-mode was cooled, and for the xy configuration,
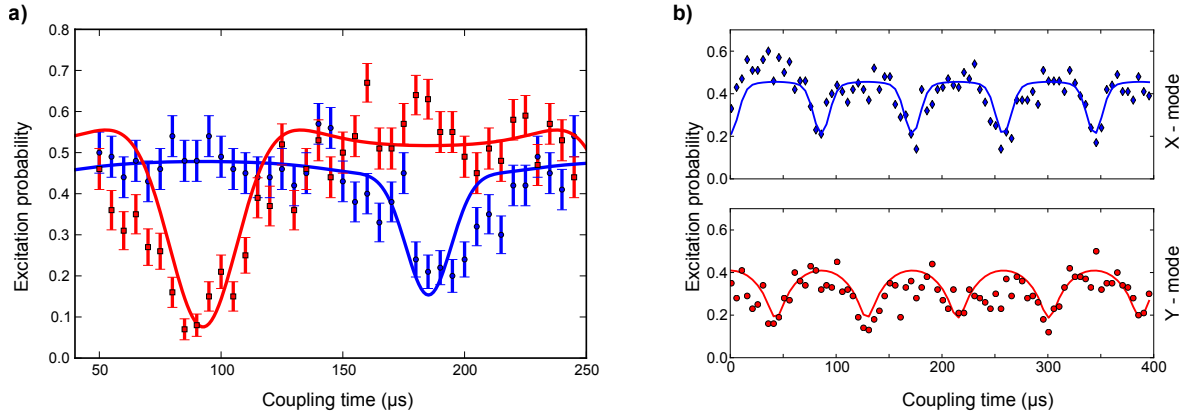
Figure 5.4: (**a**) Time evolution of the coupling dynamics illustrated by the excitation of the red sideband of the Z (blue circles) and X (red rectangles) mode. Initially, the Z mode is cooled close to its ground state at a mean phonon number of $\bar{n}_z \approx 0.2$ while the X mode is left at the Doppler temperature of $\bar{n}_x \approx 6$ quanta. After a coupling time of around 90 μs, the population of the two modes is swapped and thus the X mode is close to its ground state. Solid lines correspond to a numerical solution of the model with no free parameters. Note that the coupling time does not start at zero, because the Blackman shaped pulse is not adiabatic in this regime. (**b**) Red sideband excitation of the X (blue) and Y (red) modes. The X mode is initially cooled to a mean phonon number of $\bar{n}_x \approx 0.3$. The out of phase oscillations between the X and Y red sideband excitations show population oscillating between the two modes. Figures first published in [23]

the X mode was cooled, followed by a mode coupling pulse, applied for a variable time. The motional state after the coupling was probed on the red sideband of either mode on the $|S, -1/2\rangle \rightarrow |D, -1/2\rangle$ transition. As the mean phonon number in a given mode drops significantly below one, the excitation probability is suppressed[73, 43]. The dynamics of the coupled systems are illustrated in Fig. 5.4 where the periodic oscillations of the excitation probability represent a hallmark feature of the coupling. It furthermore allows us to define a SWAP operation where the state of the two modes are completely exchanged at around 90 μs for xz coupling, and 50 μs for xy coupling. For the xz coupling configuration, a Blackman shaped pulse needs to be used whereas for the xy configuration a square pulse is sufficient to suppress off-resonant excitation.

5.5   Cooling without direct optical access

Application: Ground-state cooling

One useful application of this technique is cooling one of the ion's vibrational modes without directly accessing the mode via a laser. The basic principle involves performing laser cooling on a single, laser-accessible mode (the *primary mode*), followed by population swapping to transfer energy from a secondary, non-cooled mode, into the primary mode. One implementation of this technique is to perform several cooling cycles on the primary mode, and to insert a SWAP operation between each cycle. With the parametric interaction operated in this way, the primary mode provides a cold reservoir for the secondary mode. After each cycle of sideband cooling, the populations of the primary and secondary modes are swapped, eventually resulting in a state where both the primary and secondary modes are prepared close to their ground state. We call this method of cooling *interleaved cooling*, allowing us to prepare both modes close to their ground states. Interleaved cooling is particularly elegant for ground state preparation because it is insensitive to errors in the SWAP operation. Even a somewhat imperfect SWAP operation will transfer a large fraction of the population between the two modes mode, where the population in the primary mode is then removed by optical cooling. Repetition of this process several times leads to significant reduction in the secondary mode population.

Interleaved cooling can prepare both modes close to their ground states when the total heating processes on both modes are slower than the cooling rate on the primary mode. However, even if this condition is not satisfied, it is still possible to prepare the secondary mode close to its ground state. Here, we take advantage of the SWAP operations that can be performed much faster than the typical cooling processes on optical transitions, as one is not limited by the relatively weak coupling of the light to the ion's motion. Therefore, one can cool the primary mode and perform a *single SWAP* operation subsequently, resulting in a cool secondary but a hot primary mode. This method is applicable as long as the SWAP operation can be performed faster than any heating process on the secondary mode.

We have tested both of these cooling techniques, using the Z-mode as the primary and the X mode as the secondary mode. In the case of interleaved cooling, we performed eight cycles of sideband cooling with a SWAP operation between each, whereas for the single SWAP cooling, the Z-mode was cooled for 8 ms followed by a single SWAP. We tabulate the results detailed in Table 5.5, showing that both simultaneous ground state cooling by interleaved cooling, as well as single swap cooling are effective techniques for cooling.

Application: Heating rate of an inaccessible mode

A second way to use the parametric interaction is to probe the thermal occupation of an optically inaccessible mode. As a demonstration, we measure the heating rate in a mode nearly orthogonal to the laser propagation direction.

Method	$\bar{n}_z$	$\bar{n}_x$
Interleaved	0.13(2)	0.31(5)
Single SWAP	7(5)	.7(2)

Table 5.1: Cooling results for both interleaved and single SWAP cooling methods. The interleaved method is capable of preparing two motional modes of the ion close to the ground state, provided that the heating rate in both modes is sufficiently low (see text). That the single SWAP method is somewhat less effective than the interleaved method for ground state preparation reflects the method's higher sensitivity to errors in the parametric resonance frequency and mode swapping time as compared to the interleaved scheme.

The heating rate on a single mode can be accurately determined by a process of cooling the mode to an average excitation much smaller than one vibrational quantum, and then probing the red and blue sideband excitation as a function of a variable waiting time after cooling[43]. However, this process relies on the ability to prepare the motional state to small mean phonon numbers, as well as optical access to the secular sidebands to read out the mode occupation.

In our experiment, the Y-mode lies nearly perpendicular to the plane of the trap, such that the projection of the laser onto this mode is about 9°–too small to use sideband cooling directly on the mode. Thus, in order to prepare the mode to small thermal occupation, we performed sideband cooling on the X-mode and then a single SWAP operation to initialize the Y-mode to a mean thermal occupation of less than a single quantum. To determine the heating rate, we analyze the mode temperature as discussed above after a variable waiting time.

As the laser is not completely orthogonal to the Y-mode, the mode temperature can be analyzed directly on the secular sidebands corresponding to the Y secular sideband. However, this requires comparably long (exceeding 500 μs) optical excitation times, during which instabilities in the mode frequency cause systematic errors. Furthermore, the excitation time is not short compared to the heating processes, adding another systematic error. Therefore, a much cleaner approach is to again apply a SWAP operation between the X and Y modes to exchange their population.

In order to verify that the second SWAP operation works as expected, we performed a heating rate experiment using both of the above techniques, with the heating time varied between 0 and 2 ms. The results of these experiments are shown in Fig. 5.5. The measurement using the direct analysis of the sideband infers a heating rate of 650(270) quanta/s whereas the measurement employing two SWAP operations yields 810(80) quanta/s. The smaller uncertainty from temperature of the Y mode via the X mode reflects the fact that the Rabi frequency on the X red sideband is considerably faster than that of the Y mode. This renders the temperature measurement much less sensitive to instabilities in the radial motional frequencies due to the reduced Fourier bandwidth of the applied pulses.
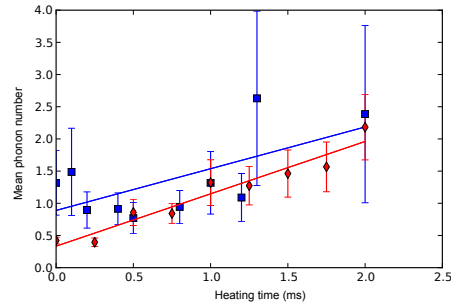
Figure 5.5: Mean phonon number as a function of heating time on the Y mode. The Y mode is prepared close to its ground state by cooling the X mode and swapping the motional states. Analysis of the motional state is either performed directly on the Y mode (blue squares) or by a second coupling operation and subsequent analysis on the X mode (red diamonds). The red line corresponds to a heating rate of $810(80)$ quanta/s, while the blue line corresponds to a heating rate of $650(270)$ quanta/s. Figure first published in [23]

Chapter 6

Surface noise studies

In quantum information processing, the shared motional degrees of freedom in an ion crystal are often used as a bus to facilitate entangling operations between ions. However, decoherence of the ion motion, induced by noisy electric fields at the ion position, limits the fidelity of entangling operations.

These noisy electric fields can result from various sources, separated broadly into "technical noise" and "surface noise". Technical noise, arguably the most prevalent type of electrical noise in ion traps refers to noise generated by electronic sources. For instance, the voltage sources used to apply DC voltages to the trap electrodes have some amount of intrinsic noise. In principle, technical noise can be reduced, for instance by better filtering.

Another noise source is Johnson noise, which is believed to be a fundamental limit to the motional coherence of ion crystals. Johnson noise can result from both the finite resistance of the trap electrodes, as well as any resistance in the filter networks attached to the trap electrodes. Johnson noise arising from the filtering electronics can be reduced by modifying the filter network, for this reason I consider this kind of Johnson noise to be a technical noise source. However, Johnson noise due to the finite resistance of the trap electrodes is an unavoidable and intrinsic property of surface electrode ion traps.

Surface noise, on the other hand, is believed to originate from properties of metallic surfaces near the trapped ion. It has been experimentally shown that treatment of an ion-trap surface by Ar^+-ion bombardment reduces the noise by up to two orders of magnitude [28, 13], strongly implicating the trap surface itself as a prominent noise source. However, the physical mechanism is unknown, and various theoretical models have been proposed in the literature, suggesting fluctuating dipole sources [60, 59], patch potentials [17, 45], or surface diffusion of adatoms [22, 73, 28]. This noise was unexpected in surface-trap experiments and is often known in the literature as "anomalous heating."

All of these noise sources present fundamental challenges to the miniaturization of ion trap technology. If surface-electrode ion traps are to be made smaller, the ions must be trapped closer to the trap electrodes, becoming therefore more sensitive to electrical noise.

On the other hand, trapping an ion near metallic surfaces allows the ion to be used as a noise sensor, perhaps leading to clues about the origin and dynamics of surface noise effects.

In this chapter, I discuss two experiments which studied surface noise effects. In the first, we studied the directional dependence of surface noise and demonstrated an experimental method for distinguishing surface noise from technical noise. In the second experiment, we were able to put a bound on the power spectral density of surface noise at very low frequencies (sub-100 Hz).

6.1   Effects of electrical noise

Before proceeding with a discussion of noise measurements, it is important to establish the mechanisms through which any kind of electric field noise affects trapped ions.

The first order effect of noise is typically *heating*. Heating is the process by which the ion's motion acquires energy due to ambient electric field fluctuations. This process requires the fluctuations to have frequency components near one of the ion's natural vibrational frequencies.

The second order effect is *dephasing*. Dephasing describes the loss of phase coherence of the motional state, and in general does not require the oscillator to acquire energy. Small random fluctuations of the ion's motional frequency will eventually randomize the phase of the motion. I discuss each of these in turn.

Heating

The standard treatment of heating due to electrical noise is given by Turchette, et. al [69]. I summarize their derivation here, with a slight generalization.

In general, a charge harmonically confined in three dimensions will oscillate in three normal modes with frequencies ω_k. Each normal mode of oscillation features excursions along a particular axis $\hat{e}_k$. The *mode vectors* $\hat{e}_k$ are subject to the orthogonality condition $\hat{e}_i^T \cdot \hat{e}_j = \delta_{ij}$. The *heating rate* (defined as $d \langle a^\dagger a \rangle / dt$) is the rate at which the oscillator mode acquires energy from the ambient noise processes. We will find the quite reasonable result that heating rate into the ω_k mode will depend on the power spectrum of electric field fluctuations along the $\hat{e}_k$ axis.

To prove this, it suffices to look at each mode individually. One begins with the assumption that the ion's motion is governed by the following Hamiltonian:

$$H = H_0 - qE_k(t)x_k \tag{6.1}$$

where H_0 is the unperturbed harmonic oscillator Hamiltonian with characteristic frequency ω_k and q is the charge of the ion. x_k is the displacement of the ion along the $\hat{e}_k$ axis, and $E_k(t)$ is a random classical electric field amplitude along the $\hat{e}_k$ direction.

Assuming that the ion is initially prepared in the ground state, the rate of population flow into the first excited state (and therefore the heating rate) is given by first-order perturbation

theory as:

$$\Gamma_k = \frac{1}{\hbar^2} \int d\tau e^{i\omega_k \tau} \langle E_k(t) E_k(t+\tau) \rangle | \langle 0 | q x_k | 1 \rangle^2 \tag{6.2}$$

$$= \frac{q^2 \pi}{m \hbar \omega_k} S_{E_k}(\omega_k). \tag{6.3}$$

Here, $S_{E_k}(\omega) = \frac{1}{2\pi} \int_{-\infty}^{\infty} e^{i\omega t} \langle E_k(t) E_k(0) \rangle$ is the power spectral density of electric field fluctuations. The form for heating rate differs by some constant factors from that given by Ref. [69]. This is due to a difference in the definition of power spectral density so as to make the notation of this chapter internally consistent. This expression tells us that the heating rate will be directly proportional to the noise power at the ion's motional frequencies.

It will be convenient for later purposes to generalize Eq. 6.3 into a more vectorial form. This is rather straightforward:

$$\Gamma_k = \frac{q^2 \pi}{m \hbar \omega_k} \vec{S_E}(\omega_k) \cdot \hat{e}_k. \tag{6.4}$$

Here, $(\vec{S_E})_k = S_{E_k}$ defined above.

Pure dephasing

Dephasing, in contrast to heating, involves the loss of phase information in the ion's motion. In this section, I adapt a treatment from de Sousa [66], in which the response of qubits to magnetic field noise is treated. I follow a semiclassical approach here, and suppose that the ion motion is governed by the following stochastic Hamiltonian:

$$H = \hbar \omega_m a^\dagger a + \hbar \eta(t) a^\dagger a. \tag{6.5}$$

As in the previous subsection, ω_m is unperturbed vibrational frequency of the ion. $\eta(t)$ is a zero-mean, stationary stochastic process. The effect of η is to dephase the oscillatory motion, and can be physically thought of as a small, randomly time-varying curvature added to the ion's trapping potential. The time evolution operator associated with Eq. 6.5 is:

$$U_\eta(t) = e^{-i a^\dagger a (\omega_m t + X_\eta(t))}, \tag{6.6}$$

where $X_\eta(t) = \int_0^t \eta(t')dt'$ represents the total integrated phase acquired by the oscillator due to the noise term. Since the specific noise trajectory η is unknown, the final quantum state of the oscillator is represented by a density operator ρ representing an average over all possible trajectories.

In order to detect these frequency fluctuations, we will consider an experiment first discussed in Sec. 4.7. In this measurement, one vibrational mode of the ion is first coherently
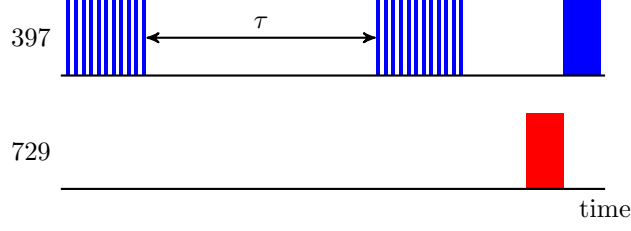
Figure 6.1: Ramsey-style probe for motional coherence. Two pulse trains of 397 nm light, each effecting a coherent motional displacement, are separated by an interrogation time τ. After the two displacement operations, a 729 nm laser pulse is applied to the blue sideband, followed by electron shelving state readout. Reproduced from Sec. 4.7 for convenience.

displaced by an amplitude α. This action is represented quantum-mechanically by the displacement operator [21]:

$$\mathcal{D}(\alpha) = e^{\alpha a^\dagger - \alpha^* a}, \tag{6.7}$$

where a ($a^\dagger$) is the harmonic oscillator annihilation (creation) operator. After a waiting time τ, another displacement operation is performed, attempting to "undo" the first displacement– a procedure very similar to a Ramsey experiment. After the second displacement, the amount of excitation left in the oscillator is probed. If the phase information in the ion's motion would be perfectly preserved, the final displacement amplitude would add coherently to the initial displacement. However, as the phase information is lost, the initial and final displacements partially interfere destructively, resulting in a smaller final displacement amplitude. If α is sufficiently large, the procedure is insensitive to heating processes since the addition of a few vibrational quanta will hardly alter the phase of a large coherent state. The experiment is shown schematically in Fig. 6.1.

The experiment can be modeled by taking the initial quantum state of the mode to be $\rho_0 = |\alpha\rangle\langle\alpha|$, where $|\alpha\rangle = \mathcal{D}(\alpha)|0\rangle$, The ion then evolves under the time evolution in Eq. 6.6. Finally, a coherent displacement operation $\mathcal{D}(\alpha)$ is applied, and the resulting amplitude is measured. This means we have to evaluate the following quantity:

$$\langle a^\dagger a \rangle = \sum_\eta p_\eta \text{Tr} \left(a^\dagger a \mathcal{D}^\dagger(\alpha) U_\eta |\alpha\rangle\langle\alpha| U_\eta^\dagger \mathcal{D}(\alpha) \right) \tag{6.8}$$

$$= \sum_\eta p_\eta \text{Tr} \left(U_\eta^\dagger \mathcal{D}(\alpha) a^\dagger a \mathcal{D}^\dagger(\alpha) U_\eta |\alpha\rangle\langle\alpha| \right) \tag{6.9}$$

$$= \sum_\eta p_\eta \text{Tr} \left((1 + \alpha^2)|\alpha\rangle\langle\alpha| + \alpha U_\eta^\dagger (a + a^\dagger) U_\eta |\alpha\rangle\langle\alpha| \right). \tag{6.10}$$

In the above, the sum is taken over all possible noise trajectories η, and p_η is the probability to take the trajectory. Between the second and third lines, I applied the identity $\mathcal{D}(\alpha) a^\dagger a \mathcal{D}^\dagger(\alpha) = (a^\dagger + \alpha)(a + \alpha)$[21], taking α to be real.

Our goal is to use the time-dependence of $\langle a^\dagger a \rangle (\tau)$ to learn about fluctuations in the resonant frequency of the ion. The first term in Eq. 6.10 is just some constants and so will not contain any time dynamics. If there is any time-dependence to be found, it will occur in the second term. We will ignore the first term and just concentrate on evaluating the second term. We only show explicitly one piece of the second term, as the other part works out analogously.

$$\sum_\eta p_\eta \mathrm{Tr}\left(U_\eta^\dagger a U_\eta\right)|\alpha\rangle\langle\alpha| = \sum_\eta p_\eta \mathrm{Tr}\left(e^{i(\omega_m t + X_\eta(t))}a^\dagger|\alpha\rangle\langle\alpha|\right) \tag{6.11}$$

$$= e^{i\omega_m t}\sum_\eta p_\eta e^{iX_\eta(t)}\mathrm{Tr}\left(a^\dagger|\alpha\rangle\langle\alpha|\right) \tag{6.12}$$

$$= e^{i\omega_m t}\left\langle e^{iX_\eta(t)}\right\rangle \mathrm{Tr}\left(a^\dagger|\alpha\rangle\langle\alpha|\right). \tag{6.13}$$

The result is that the final measurement will be damped by the factor $\left\langle e^{iX_\eta(t)}\right\rangle$. If the noise process η takes Gaussian-distributed amplitudes, Ref. [66] evaluates Eq. 6.13 to

$$\left\langle e^{iX_\eta(t)}\right\rangle = \exp\left(-\int_0^\infty S_\eta(\omega)\frac{\sin^2(\omega t/2)}{(\omega/2)^2}d\omega\right), \tag{6.14}$$

with

$$S_\eta = \frac{1}{2\pi}\int_{-\infty}^\infty e^{i\omega t}\left\langle \eta(t)\eta(0)\right\rangle dt. \tag{6.15}$$

Here, S_η is the power spectrum of for the random variable η.

It is worth pausing a moment to reflect on this result. We have described a simple experiment to probe phase coherence in a mechanical oscillator. Furthermore, in Eq. 6.14 we have related the measurement result to the power spectrum of the noise. In Sec. 6.4, we will use the results of this experiment to study the frequency dynamics of surface noise.

6.2   A simple model of surface noise

A simple model of surface noise effects in planar surface traps may be obtained by considering the surface noise source as a charge trapped to the surface. In the limit where the charge is trapped much closer to the surface than the ion-electrode distance, the charge, combined with its image charge below the metallic surface may be treated as a dipole. The same argument should extend to other "small" noise sources, e.g. fluctuating patch potentials, as long as the ion-electrode distance is large as compared to some characteristic size of the noise source.

Our model relies on two fundamental assumptions: first, that the dipole is oriented normally to the trap surface. This is true in the limit that the trap electrodes are made from a perfect conductor. A second assumption is that the noise sources are uncorrelated.

A third, relatively weak, assumption is that the trap surface may be treated as an infinite plane.

Take the ion to be trapped at $(x, y, z) = (0, d, 0)$. A dipole (magnitude p) located at some point on the surface will produce the electric potential

$$\Phi = \frac{py}{4\pi\epsilon_0((x - x_d)^2 + y^2 + (z - z_d)^2)^{3/2}} \tag{6.16}$$

at the trapping position. Φ is expanded to second order around the trapping position as:

$$\begin{aligned}
\Phi \approx \frac{p}{4\pi\epsilon_0} \Bigg(& \frac{3dx_d}{r_0^5}x + \frac{-2d^2 + x_d^2 + z_d^2}{r_0^5}(y - d) \\
& + \frac{3d(d^2 - 4x_d^2 + z_d^2)}{2r_0^7}x^2 + \frac{3d(2d^2 - 3(x_d^2 + z_d^2))}{2r_0^7}(y - d)^2 \\
& + \frac{3x_d(-4d^2 + x_d^2 + z_d^2)}{r_0^7}x(y - d) \Bigg)
\end{aligned} \tag{6.17}$$

where $r_0 = \sqrt{d^2 + x_d^2 + z_d^2}$ is the ion-dipole distance. To save space, the z^2, xz and yz terms are omitted as they are the same as the analogous terms above due to $x - z$ symmetry.

For later convenience, I will name the various coefficients in the previous equation:

$$\Phi \approx E_x x + E_y y + E_z z + Q_{xx} x^2 + Q_{yy}(y - d)^2 + Q_{xy} x(y - d) + \dots \tag{6.18}$$

The terms linear in space are the electric field components, giving rise to heating processes. The terms quadratic in space modify the curvature of the potential seen by the ion, perturbing the vibrational frequency of the ion.

Electric field fluctuations

The heating rate into a mode is given by the power spectral density of the total electric field fluctuations. The easiest way to get this is to calculate the autocorrelation of the total electric field, given as a sum over dipoles.

We only need to calculate each dipole's autocorrelation as we assume each dipole is uncorrelated with any other dipoles. In the directions parallel to the plane of the trap (x and z):

$$\langle E_x(t)E_x(0) \rangle = \int \left(\frac{3dx_d}{4\pi\epsilon_0 r_0^5} \right)^2 \langle p(t)p(0) \rangle \, dx_d dz_d \tag{6.19}$$

$$= \frac{3}{128d^4\pi\epsilon_0^2} \langle p(t)p(0) \rangle \tag{6.20}$$

$$= \langle E_z(t)E_z(0) \rangle. \tag{6.21}$$

Here $\langle p(t)p(0) \rangle$ is the autocorrelation of the dipole moment magnitude for a single dipole. We expect no spatial dependence in this function so it is not included in the spatial integral.

Likewise, we can calculate this integral for the vertical direction:

$$\langle E_y(t)E_y(0)\rangle = \int \left(\frac{-2d^2 + x_d^2 + z_d^2}{4\pi\epsilon_0 r_0^5}\right)^2 \langle p(t)p(0)\rangle\, dx_d dz_d \tag{6.22}$$

$$= \frac{3}{64 d^4 \pi \epsilon_0^2} \langle p(t)p(0)\rangle \tag{6.23}$$

Putting each of these components into a vector gives:

$$\vec{S}_E = \frac{3}{128\pi\epsilon_0^2 d^4} \langle p(t)p(0)\rangle \begin{pmatrix} 1 \\ 2 \\ 1 \end{pmatrix} \tag{6.24}$$

It is important to note that this model is purely *geometric*, and does not make predictions about the frequency dependence. The model does however make several specific predictions: first that the heating rate due to surface effects should scale as d^{-4} with d being the ion-electrode distance. This distance scaling is suspected from simple models, but not directly confirmed in a planar trap geometry. This also predicts a slight polarization in the electric field fluctuations: the noise *normal* to the trap (y-direction) should be twice as large as the fluctuations *parallel* to the trap. We investigate this polarization experimentally in Sec. 6.3 and Ref. [62].

Quadrupolar fluctuations

Extending the analysis to the second order, we can also make some predictions about "pure dephasing" processes. Quadrupolar fluctuations, or quadratic variations of the potential around the ion position, do not contribute to heating because the *electric field* due to these terms is zero at the trapping location. These second order potentials do, however, change the *curvature* of the trapping potential experienced by the ion. A fluctuating curvature will perturb the ion's oscillation frequency and thus give rise to phase randomization, or dephasing, of the motion over some time.

The dipole model predicts a simple relationship between the power spectrum of quadrupolar potential fluctuations and the power spectrum of electric field fluctuations. The autocorrelation integral works the same way as the electric field in the previous section.

$$S_{Q_{xx}} \equiv \langle Q_{xx}(t)Q_{xx}(0)\rangle = \int \left(\frac{3d(d^2 - 4x_d^2 + z_d^2)}{4\pi\epsilon_0 2 r_0^7}\right)^2 \langle p(t)p(0)\rangle\, dx_d dz_d \tag{6.25}$$

$$= \frac{45}{512\pi\epsilon_0^2 d^6} \langle p(t)p(0)\rangle\,. \tag{6.26}$$

Q_{xx} is defined in Eq. 6.18. Therefore the model predicts $S_{Q_{xx}} = \frac{15}{4d^2} S_{E_x}$. One interesting result of this is that the quadrupolar fluctuations should scale as d^{-6}. This will impose a limit to the miniaturization of ion traps for quantum information processing experiments. In Ref. [67] and Sec. 6.4, we use the relationship between S_E and S_Q to make inferences about the dynamics of surface noise properties.

6.3   Experiment: Electric field noise polarization

This Section describes work first published in [62].

Heating effects in trapped ions are due to the sum of all noise sources, whether the origin is technical in nature or due to material properties of the trap surface. However, technical noise tends to be polarized in a different orientation than surface noise. This provides an experimental method to determine if electric field noise in a surface trap experiment is due to technical sources. For experiments in which a trapped ion is used to study surface noise specifically, ruling out technical noise is an important step. Even in experiments which do not aim to study surface effects, it is useful to know if noise can be reduced by improving electronics.

In this work, we varied the orientation the vibrational modes of a single ion (see Fig. 6.2) to measure different components of the vector quantity $\vec{S_E}$, the power spectrum of electric field fluctuations. In Sec. 6.2, we showed that for a simple phenomenological noise model involving dipole sources on a metallic surface that the magnitude of electric field fluctuations oriented *normally* to the surface are twice as large as fluctuations *parallel* to the plane of the surface.

In fact, this prediction appears in other popular noise models as well. One such model to describe surface noise is fluctuating patch potentials [17]. It is shown that in the limit of small patches [45] that the maximum degree of field noise polarization is also two. In [62], we marginally extend Ref. [17] to show that the polarization $R = 2$ independent of the patch size. We quantify the polarization as $R = \vec{S_E} \cdot \hat{y} / \vec{S_E} \cdot \hat{x}$ where $\hat{y}$ is a unit vector normal to the trap plane and $\hat{x}$ is a unit vector parallel to the trap plane.

Technical noise, by contrast, exhibits a polarization given by the electrode geometry. This is because technical sources by nature cause the voltage on the entire electrode to vary. For each electrode, the direction of the field produced at the ion position is given entirely by the geometry, establishing the polarization.

The exact polarization expected from technical sources depends on how the noise is modeled. For our work, we consider two different, yet reasonable, noise models: *(i)* a voltage independent model where the magnitude of the noise on all electrodes is equal and *(ii)* a voltage dependent model where the noise magnitude is proportional to the applied voltage. Model *(i)* describes Johnson noise originating from the filter electronics, and model *(ii)* could represent, for instance, references of the individual digital to analog converters. For both models, we assume that the noise on different electrodes is uncorrelated, i.e. there are no fixed phase relation between the corresponding voltages.

The contribution of each electrode to the heating of the ion motion can be determined by evaluating the electric field that a voltage on the electrode generates at the ion position. Since the noise is assumed to be uncorrelated between electrodes and the wavelength is much larger than the ion-surface distance, the total noise at the ion position is proportional to the sum of the squares of the electric fields of all electrodes, projected on the respective normal mode direction. For planar trap geometries as shown in Fig. 6.2, the contribution from the
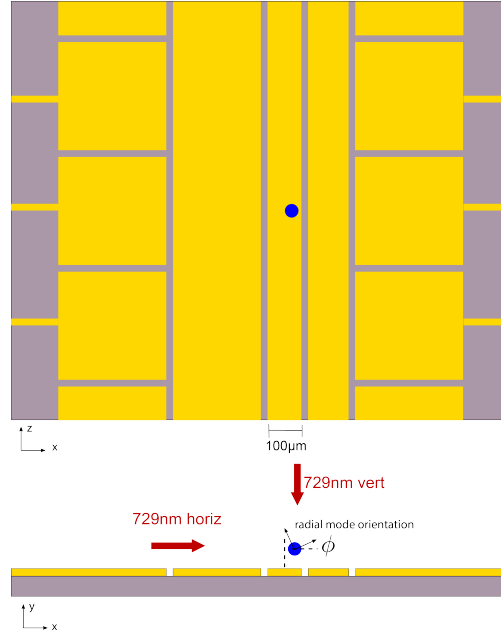
Figure 6.2: Schematic drawing of the asymmetric surface trap used in the experiments. The orientation of the 729 nm laser beams is shown. These beams are oriented so that both radial modes can be sideband cooled close to the motional ground state to enable heating rate measurements. The orientation of the radial modes is shown in the bottom figure. The mode vectors for these modes are rotated by a variable angle ϕ with respect to the trap geometry. The expected trapping height is 107 μm above the surface. This figure is slightly modified from one appearing in Ref. [62]

center electrode, directly below the ion, dominates over all other electrodes. This effect can be exploited to distinguish technical noise from surface noise in a planar ion trap.

This effect is especially striking for the voltage independent noise model *(i)* in an asymmetric trap where the two RF rails have considerably different widths as sketched in Fig. 6.2. This geometry leads to a trapping position which is not centered on the central electrode. Thus, the electric field originating from the central electrode at the trapping position does not point perpendicular to the trap surface but rather at an angle ϕ_g. Since the noise is dominated by the central electrode, the noise is maximal if the mode axis is approximately aligned with ϕ_g. The noise contribution of the central electrode is about a factor of 60 larger than that of the electrode with the second largest contribution. For the voltage dependent noise model *(ii)* the angle of the maximum noise depends on the applied static voltages and needs to be analyzed for each particular set of voltages.

The noise polarization can be determined independently of the absolute noise magnitude by evaluating the ratio of the heating rates in two normal modes. The black solid line in Fig. 6.3 shows the expected ratio of the heating rate of the two radial modes for the voltage independent noise model, leading to a maximum ratio of $R_{\text{indep}} \approx 30.1$, which can
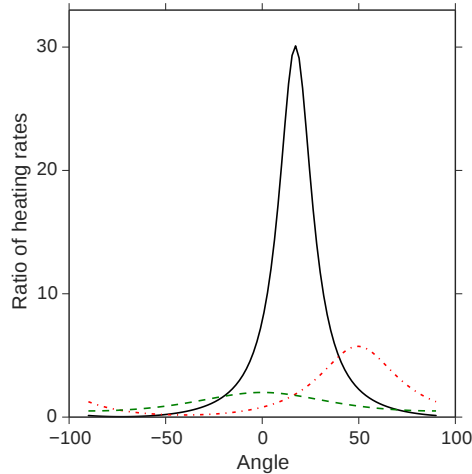
Figure 6.3: Ratio of the predicted heating rates in the two radial modes for various noise models as a function of the radial mode rotation angle ϕ. The green dashed line corresponds to surface noise, the black solid line corresponds to the voltage independent noise model and the red dash-dotted line corresponds to the voltage dependent model.

be observed at an angle of $\phi_{\text{indep}} \approx 17°$. For the voltage dependent noise level and the set of voltages used in our setup, the maximum ratio is $R_{\text{dep}} \approx 5.7$ for an angle $\phi_{\text{dep}} \approx 50°$.

Measurements

The polarization of the noise in an ion trap can be estimated by measuring the heating rates of the normal modes while rotating the mode orientation with respect to the trap surface by an angle ϕ (see Fig. 6.2). Since the noise is also frequency dependent, it is is important to perform all measurements at approximately the same mode frequency. Thus, it is beneficial to use the two radial modes, as their frequencies are similar whereas the axial trap frequency is usually considerably smaller. We denote the two normal radial modes $\updownarrow$ and $\leftrightarrow$, where the mode $\leftrightarrow$ shows an angle ϕ with respect to the trap surface, and the two modes are perpendicular to each other. The heating rates for those two modes are given by

$$S_{\updownarrow} = S_{\text{max}} \cos(\phi - \phi_{\text{max}})^2 + S_{\text{min}} \sin(\phi - \phi_{\text{max}})^2 \tag{6.27}$$
$$S_{\leftrightarrow} = S_{\text{max}} \sin(\phi - \phi_{\text{max}})^2 + S_{\text{min}} \cos(\phi - \phi_{\text{max}})^2 , \tag{6.28}$$

where $S_{\text{max,min}}$ is the maximum (minimum) noise amplitude and ϕ_{max} is the angle where the maximum noise can be observed.

For this method it is required to rotate the radial trap modes without affecting the mode frequency considerably. This can be achieved by altering the static confinement. The voltages

on the trap electrodes are controlled by digital-to-analog converters (DACs) (See Sec. 4.4), and so the confining potential may be modified by adjusting the electrode voltages. We adjust the voltages on the trap electrodes following the procedure described in Sec. 2.2. For these measurements, we generate potentials which are linear combinations of the multipole fields $U_1 = x^2 - y^2$, $U_2 = z^2 - x^2 - y^2$, and $U_3 = x \cdot y$. The terms $U_{1,3}$ allow control over the orientation of the radial trap axes. The multipoles U_1 and U_3 generate potentials with axes parallel to the trap surface or at 45°, respectively. We apply a set of voltages which generate the potential $C_1 U_1 + C_3 U_3$. By choosing the coefficients appropriately, the radial modes may be rotated by an arbitrary angle ϕ:

$$C_1 = C \, \cos(2\phi) \tag{6.29}$$
$$C_3 = C \, \sin(2\phi) \tag{6.30}$$

where C is the overall potential magnitude which has to be large enough to overcome symmetry breaking due to stray fields. The resulting potential including the confinement in the axial direction is then:

$$U = C_2(x^2 + y^2 - 2z^2) + C_1(x^2 - y^2) + C_3(x \cdot y) + U_{\mathrm{RF}}$$

with C_2 determining the strength of the axial confinement. The RF potential U_{RF} and U_2 have rotational symmetry around z and thus do not affect the mode orientation.

In our surface trap, we are also able to rotate the radial trap axes by applying a static negative bias voltage onto the RF drive. This orients the trap axis of the higher frequency mode ($\updownarrow$) to ϕ_g, which corresponds to the orientation where one of the normal modes is aligned with the field from the central electrode and hence close to the orientation of the maximum noise for voltage independent noise.

Experimentally, changing the trap axis by applying a static bias voltage onto the RF electrode is more reliable than controlling the multipoles of the trap potential, as no precise simulation of the trap potential is required and miscalibration of the voltage source does not change the axes orientation

In order to estimate the ratio R, the heating rates of both radial modes need to be measured. First, the radial mode of interest is sideband cooled (See Sec. 3.4) close to the ground state by whichever 729 nm beam has the stronger projection. After this state preparation, a variable waiting time τ_{heat} is applied, during which the mode heats up at some rate. After the waiting time, the thermal occupation n is measured spectroscopically following Sec. 3.4. Fitting n vs. τ_{heat} gives the heating rate.

We measured the heating rates in both modes while keeping the trap frequencies constant at 2.6 ± 0.1 MHz. Figure 6.4 shows the heating rate as a function of the normal mode angle. For all but the angle ϕ_g the axes are rotated by controlling the static multipole confinement of all electrodes. For measuring at trap orientation with angle ϕ_g, a static bias voltage is applied to the rf electrodes.

Applying this bias voltage on the rf electrodes allows for the most reliable trap rotation and thus we will only use this method for quantitative analysis of the noise polarization.
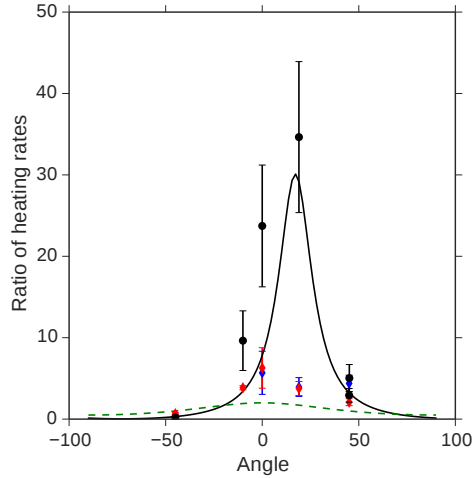
Figure 6.4: Measured ratio of the heating rate in the two radial modes as a function of rotation angle ϕ. Red and blue diamonds are measurements without additional noise taken on different days. Black crosses are measurements with additional noise on the central electrode. The green dashed line corresponds to surface noise whereas the black solid line corresponds to the technical noise model. This image is published in Ref. [62]

It is by coincidence that in our trap geometry, biasing the rf electrodes rotates the normal mode orientation to ϕ_g. For geometries in which this is not the case, care must be taken to ensure that the desired normal mode orientation is achieved. This can involve ensuring the individual DACs are well calibrated, or directly measuring the Lamb-Dicke parameter with a known laser orientation (see Sec. 3.3). We find a ratio of heating rates in the two modes of $R = 4.2(5)$ which is small compared to the ratio predicted by the voltage independent noise model of $R \approx 30.1$. From this we can exclude the voltage independent technical noise model as the dominant noise source in our setup.

In order to exclude the voltage dependent noise model, we measure the heating rate for the $\updownarrow$ mode for two different sets of voltages providing an axial confinement of approximately 1 MHz (for set i) and 707 kHz (for set ii) while keeping the radial trap frequencies constant. The voltages of the sets differ by a factor of two and assuming the voltage noise to be proportional to the voltage, one would expect the heating rates to differ by a factor of four as the heating rate scales with the power spectral density of the noise. We measure a heating rate of $\dot{n} = 0.69(6)$ quanta/ms for set i and $\dot{n} = 0.52(3)$ quanta/ms for set ii, yielding a factor of 1.3(1) between the two heating rates. With this result we can exclude being dominated by noise that scales linearly with the applied voltage, as the model predicts a change in heating rate of a factor of four. A weaker scaling cannot be excluded completely but inferring a scaling factor would give no meaningful results due to large statistical uncertainties.

We further test the method by adding voltage noise to only the central electrode with a white noise generator. This should lead to an increase of the heating rate in the mode parallel to the maximum noise direction, whereas the perpendicular mode should not be affected. The experiments demonstrate this effect: The heating rate in the perpendicular mode without adding noise is $\dot{n}_{\leftrightarrow} = 0.12(3)$ quanta/ms and with added noise $\dot{n}_{\leftrightarrow} = 0.15(3)$ quanta/ms. In contrast, the measured ratios are $R = 4.2(5)$ without adding noise and $R = 34(9)$ with added noise. This indicates that we can align the trap axes with the electric field generated by the center electrode (at angle ϕ_g) with adequate precision.

Conclusions

Because surface noise and technical noise are polarized in different directions, we can use these measurements to estimate the amplitude of surface noise even in the presence of technical noise. First, we assume a surface noise model featuring a ratio of $R_{\text{surf}} = 2$, as well as additional technical noise with an unknown ratio R_{techn}. It is convenient to perform the measurement at angle ϕ_g as this angle can be set with highest precision. Assuming that surface and technical noise are not correlated, the noise power spectral density is additive (the fields add in squares): $S_{\text{tot}} = (S_{\text{surf}} + S_{\text{techn}})$ with S_{techn} originating from voltage independent technical noise. The ratio of the heating rates between both axes is measured and thus it is possible to estimate the magnitude of the surface noise as

$$S_{\text{surf},\leftrightarrow} = S_{\text{tot},\leftrightarrow} \frac{R_{\text{tot}} - R_{\text{techn}}}{R_{\text{surf},\phi} - R_{\text{techn}}} \ . \tag{6.31}$$

For the measured ratio $R_{\text{tot}} = 4.2(5)$ and the expected ratio for patch potentials $R_{\text{surf},\phi} = R_{\text{surf}} \cos^2\phi = 2 \cos^2\phi$, this leads to $S_{\text{surf},\leftrightarrow} = 1.8(2) \times 10^{-12} (\text{V/m})^2/\text{Hz}$. One needs to keep in mind that this noise amplitude is measured at the angle ϕ_g. The surface noise magnitude parallel to the trap surface (along the x-axis) is then

$$S_{\text{surf},x} = \frac{S_{\text{surf},\leftrightarrow}}{R_{\text{surf}} \sin(\phi)^2 + \cos(\phi)^2} = 1.7(2) \times 10^{-12} (\text{V/m})^2/Hz \ . \tag{6.32}$$

It will always be possible to construct technical noise models which explain our results by carefully choosing the amplitudes and correlations of the various voltage supplies. However, those models seem rather contrived. Assuming a simple and realistic technical noise model and a surface noise caused by either surface dipoles or fluctuating patch potentials, we can disentangle the contributions from technical noise and surface noise with high confidence. From this we can conclude that technical noise is irrelevant to the field noise parallel to the trap surface, while its contribution in the vertical direction is comparable to surface noise. Using this method it will be possible to compare heating rates from different traps, allowing a meta-analysis of different experiments.

6.4 Experiment: Motional coherence of trapped ions

It is also possible to use single trapped ions to study dephasing processes (Sec. 6.1). This section concerns work first published in Ref. [67]. For this experiment, theory and analysis was done by the present author, while the measurements were performed by Ishan Taluk-dar. The experiment was performed in a different experimental setup than the work in the previous Section.

The purpose of this experiment was to study the motional coherence of ions as it pertains to quantum information processing experiments in surface traps. In particular, we were concerned by the possibility that low motional coherence times may limit the fidelity of two-qubit entangling gates even when heating rates are quite low. Indeed, the simple noise model in Sec. 6.2 suggests that the heating rate should scale as d^{-4}, while the rate of dephasing should scale as d^{-6}, where d is, as usual, the ion-electrode distance. Thus, for traps sufficiently small, we expect the dephasing time to be much faster than the heating rate.

Motional dephasing results from low-frequency fluctuations in the trapping potential as seen by the ion. Many theoretical models of surface noise predict that the power spectrum should change from spectrally flat white noise below a cutoff frequency ω_{ir} into $1/\omega^{\beta}$-noise above the cutoff. The frequency of this cutoff may help discriminate between physical noise models and provide insight into the physical processes giving rise to surface noise effects.

In this Section, we use a single ion as a noise sensor for the low-frequency behavior of surface noise. Experimentally, we apply the Ramsey-style interrogation of the ion motion discussed in Sec. 4.7 and Sec. 6.1. A schematic of the experimental pulse sequence is given in Fig. 6.1. Briefly, the axial mode of a single ion is Doppler cooled, and then coherently displaced by a train of 397 nm laser pulses, generating a displacement $|\alpha|^2 \approx 50$. The repetition rate of the train is detuned from the trap frequency by the small amount δ_m. After an interrogation time τ, the displacement is applied again, wherein the relative phase between the pulse train and the ion's motion has evolved by $\delta_m\tau$. The final displacement amplitude $|\alpha|^2$ is determined by a short 729 nm laser pulse applied to the blue axial sideband and the D-state occupation probability is measured by electron shelving. The displacement amplitude is measured by determining the Rabi frequency on the sideband transition, as discussed in Ref. [52].

Without dephasing, the final displacement amplitude evolves periodically with frequency δ_m, oscillating between 0 and 2α. Additional dephasing due to perturbations of the motional frequency leads to a random phase evolution, reducing the contrast of the oscillations (Fig. 6.5(a)).

Spectral model

The inferences in this experiment rely on two main assumptions: First, we assume a simplified form for the noise power spectrum, shown in Fig. 6.5(b). That is, we assume that above some frequency ω_{ir}, the noise scales as $\omega^{-\beta}$ for some $\beta > 0$. To prevent an infrared divergence
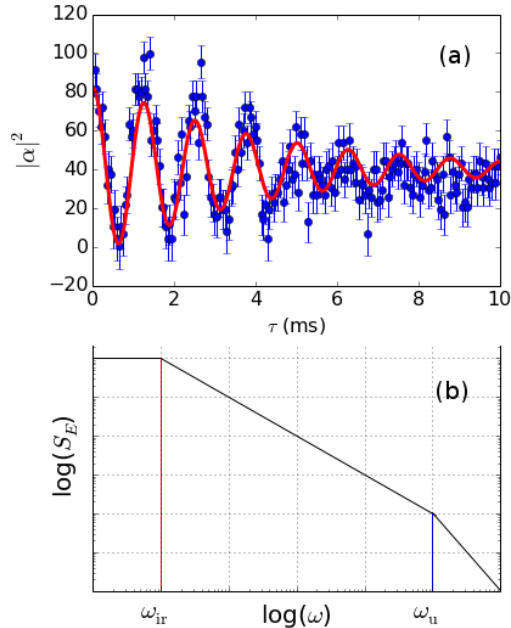
Figure 6.5: (a) Displacement amplitude $|\alpha|^2$ vs interrogation time τ in ms. The solid red line is a fit to a model which depends on the overall amplitude of the noise as well as its spectral features. (b) The noise power spectrum assumed in the analysis. It is believed that the noise goes as $\omega^{-\beta}$ over some range $(\omega_{\mathrm{ir}}, \omega_{\mathrm{u}})$. We assume that the power spectrum rolls off to $\sim \omega^0$ below the low-frequency cutoff ω_{ir}. If $\beta \leq 1$, the power spectrum is required to have a high-frequency cutoff at ω_{u} so that the total noise power is finite. Such a high-frequency cutoff would be significantly higher frequency than our measurements are sensitive to, and thus does not enter the analysis. This figure was originally published in Ref. [67].

in the total noise power, we impose a roll-off at ω_{ir}, below which frequency the noise scales as ω^0. The experiment is not sensitive to frequencies much faster than $1/\tau \sim$ kHz, where τ is the interrogation time between displacement operations, so the high-frequency form of the spectrum is irrelevant. The second assumption is that the spectrum of quadrupolar fluctuations is related to the spectrum of electric field fluctuations in the way discussed in Sec. 6.2:

$$S_{Q_{xx}} = \frac{15}{4d^2} S_{E_x}, \tag{6.33}$$

where d is the ion-trap distance (50 μm, in this case).

The electric field fluctuations, S_E have been measured in this trap over a range of frequencies (see Fig. 6.6) from 350 kHz to 1.3 MHz. Such a measurement is performed by adjusting the electrode voltages to achieve the desired trap frequency and measuring the heating rate in this configuration. The measurements here yield a scaling factor $\beta = 0.9(0.2)$. In the literature, other values of β are found, ranging from (-1) - (+7) [9].
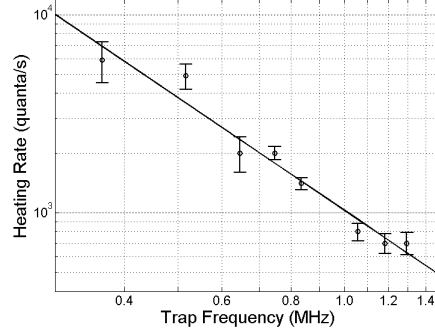
Figure 6.6: Heating rate vs. trap frequency for the trap discussed in this experiment. The heating rate shows a scaling of $\omega^{-1.9(0.2)}$, implying $S_E \sim \omega^{-0.9(0.2)}$. This figure was originally published in Ref. [67].

Heating rate measurements probe the spectral noise density at a specific frequency–i.e., the motional frequency of the ion. However, heating rate measurements cannot probe the noise spectrum at very low frequencies due to ion loss. As the trap frequency is relaxed, the trap depth also decreases, reducing ion lifetime in the trap until it is infeasible to continue with experiments. The reduced ion lifetime is probably due to collisions with background gases which can eject the ion from the trap if the depth is small enough. Nevertheless, we attempt to make inferences about the low-frequency noise characteristics based on measurements of the dephasing noise.

Given the frequency scaling β, the low-frequency roll-off ω_{ir}, and the heating rate at a particular trap frequency ω_0, the noise spectrum may be extrapolated down to zero frequency as:

$$S_E(\omega) = \begin{cases} S_E(\omega_0)\left(\frac{\omega_0}{\omega}\right)^{\beta} & \text{if } \omega > \omega_{\mathrm{ir}} \\ S_E(\omega_0)\left(\frac{\omega_0}{\omega_{\mathrm{ir}}}\right)^{\beta} & \text{if } \omega < \omega_{\mathrm{ir}}. \end{cases} \tag{6.34}$$

In order to make use of our results from Sec. 6.1, we need to put our quadrupolar fluctuations in the form of Eq. 6.5. The noise enters the Hamiltonian via the random electric potential

$$q\Phi(t) = qQ_{xx}(t)x^2 \tag{6.35}$$

$$= qQ_{xx}(t)\frac{\hbar}{2m\omega_{\mathrm{ax}}}\left(a^2 + \left(a^\dagger\right)^2 + a^\dagger a + a a^\dagger\right) \tag{6.36}$$

$$\approx qQ_{xx}(t)\frac{\hbar}{m\omega_{\mathrm{ax}}}a^\dagger a, \tag{6.37}$$

where ω_{ax} is the axial trap frequency, m the ion mass, and a and $a^\dagger$ the harmonic oscillator creation and annihilation operators respectively. I neglect a^2 and $(a^\dagger)^2$ due to the rotating

wave approximation and neglect the commutator $[a, a^\dagger] = 1$ because the quantum state of the ion is assumed to be a large coherent state. Thus, to go into the notation of Sec. 6.1,

$$\eta(t) = \frac{q}{m\omega_{\text{ax}}} Q(t), \tag{6.38}$$

and therefore

$$S_\eta(\omega) = \left(\frac{q}{m\omega_{\text{ax}}}\right)^2 S_{Q_{xx}}(\omega). \tag{6.39}$$

To relate all of this back to the heating rate measurements, we have:

$$S_\eta(\omega) = \left(\frac{q}{m\omega_{\text{ax}}}\right)^2 \left(\frac{15}{4d^2}\right) S_E(\omega_0) \times \begin{cases} \left(\frac{\omega_0}{\omega}\right)^\beta & \text{if } \omega > \omega_{\text{ir}} \\ \left(\frac{\omega_0}{\omega_{\text{ir}}}\right)^\beta & \text{if } \omega < \omega_{\text{ir}}. \end{cases} \tag{6.40}$$

The electric field noise spectral density can be determined from Eq. 6.3:

$$S_E(\omega_0) = \frac{m\hbar\omega_0}{q^2\pi} \Gamma_0, \tag{6.41}$$

where Γ_0 is the heating rate when $\omega_{\text{ax}} = \omega_0$.

Analysis

In Eq. 6.14, I claimed that the Ramsey-style fringes in this experiment (Fig. 6.5(a)) should be damped by an exponential factor involving the power spectrum of frequency fluctuations.

The primary goal of the analysis was to estimate the roll-off frequency ω_{ir}. Because the noise at low-frequency is extrapolated from high-frequency measurements, the estimate will depend on the factor β which determines how the noise scales with frequency in the high frequency regime. As different measurements have found conflicting values of β [9], we run the analysis for several different values of β ranging from 1 to 2.

With the parameter β fixed, the fringes in Fig. 6.5(a) were fit to the following form

$$|\alpha|^2(\tau) = A\cos(\delta_m\tau)\exp\left(-\int_0^\infty S_\eta(\omega)\frac{\sin^2(\omega\tau/2)}{(\omega/2)^2}d\omega\right). \tag{6.42}$$

where S_η is given in Eq. 6.40. In the fit, β is taken fixed, and fit is performed over the overall amplitude A and the cutoff frequency ω_{ir}. The filter function $\frac{\sin^2(\omega\tau/2)}{(\omega/2)^2}$ drops quickly to zero as $\omega \gg 1/\tau$. This means that the experiment is sensitive only to low-frequency noise. Furthermore, it means that we do not need to make any assumptions about the behavior of $S_\eta(\omega)$ above the trap frequency. The results are shown in Fig. 6.7. The low-frequency cutoff estimate depends strongly on the choice of scaling exponent. On the low end, we find a cutoff estimate of 10^{-4} Hz if $\beta = 1$, as compared to about 1 kHz if $\beta = 2$. The error
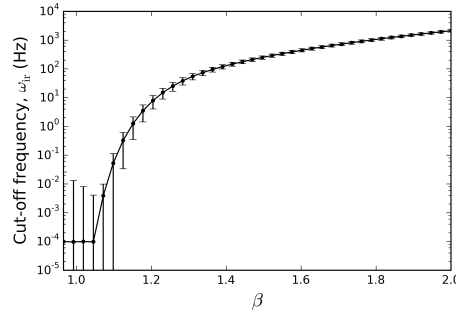
Figure 6.7: Cutoff frequency ω_{ir} as a function of the assumed scaling law β. Error bars are the standard errors from the fit.

bars in that plot are the standard errors resulting from the numerical fitting procedure. An entire experimental run, varying the Ramsey duration from 0 to 10 ms, can take up to about 10 minutes to complete. This time sets the minimum frequency to which the experiment is sensitive. To enforce this in the analysis, we enforce a minimum $\omega_{\mathrm{ir}} \geq 10^{-4}$ Hz. For this reason, the smallest four cutoff estimates around $\beta = 1$ all lie on a line.

We can compare these findings to certain theoretical results. For example, the surface diffusion model [22, 73] predicts a exponent of $\beta \simeq 1.5$ with an estimated low frequency cut-off on the order of 10^{-7} Hz. Assuming $\beta = 1.5$ in the frequency regime below 100 kHz, we extract from our data a cut-off of ~ 300 Hz, much higher than the cut-off estimated by the same model. Thus the surface diffusion model does not provide a consistent description of the noise for the surface studied here. Another model suggests adatoms of high molecular mass bound to the surface as the source for noise[60]. The cut-off in this model scales inversely with the atomic mass of the adatom. The adatom model would require unreasonably large ($m \sim$ several thousand a.u.) weakly bound atomic masses adsorbed to the surface to explain the observed dephasing in Fig. 6.5(a). In that model, realistic cut-off frequencies are in the range of one to hundreds of MHz. Thus, we conclude that some other noise process either of technical or physical nature is responsible for the dephasing. The voltage stability of the dc voltage sources supplying the trap electrodes was analyzed with a measurement bandwidth of 10 mHz to 100 kHz. The rms voltage fluctuations on the dc electrodes was found to be 10 μV. Electrostatic simulations of the trap geometry imply that this level of voltage fluctuation would lead to a dephasing time of 36 ms, significantly longer than the dephasing time observed in Fig. 6.5(a). However, technical noise sources cannot be excluded with certainty. Thus, it will be valuable in the future to perform these measurements in conjunction with surface-cleaning techniques [28, 13] to prove that the observed dephasing is due to surface effects.

Chapter 7

Quantum simulation of energy transfer

7.1   Introduction

At press time, the results of this section were not published, but a manuscript is in preparation for submission to the peer-reviewed literature.

Analog quantum simulation refers to the notion that a controllable quantum system–e.g., a chain of trapped ions–can be made to mimic (or *simulate*) the dynamics of a theoretical model system. This is particularly interesting when the model is believed to describe some process in nature, but the model is challenging to study numerically. It is hoped that *quantum simulators* can faithfully emulate models in a lab setting–thereby allowing experimental study when analytical and numerical methods are unavailable. Ideally, the experiment permits tuning the model parameters, allowing physical insight to be gained.

Since trapped ions may be used as qubits–controllable, two-level systems– it is quite natural to use them to emulate coupled-spin systems [49]. As shown in Sec. 3.6 and Refs. [65, 57], the interaction between ion-qubits can mimic magnetically-coupled spins. For instance, ion systems have simulated frustrated magnetism [39], and the transition of spin chains from paramagnetic to ferromagnetic order [31], to cite two examples. The Hilbert space to describe an N-spin system is of dimension 2^N, meaning that simulation of a system as small as "a few tens of spins" would challenge classical computational resources [7, 68].

In addition to the qubit degree-of-freedom, ion chains also possess a set of normal vibrational modes. These modes are well-described by uncoupled quantum harmonic oscillators, and can also be used as a resource for quantum simulation. The simplest example of this is the Jaynes-Cummings model. By inspection of Eq. 3.17, it can be seen that the dynamics of a single ion irradiated on the red sideband is described by the Jaynes-Cummings model [7, 34], where the electronic state of the ion corresponds to a two-level atom, and the vibrational mode corresponds to an optical cavity mode. In a more complicated example, large Coulomb crystals have also been suggested [50] to simulate the spin-boson model [42]. In that case, a
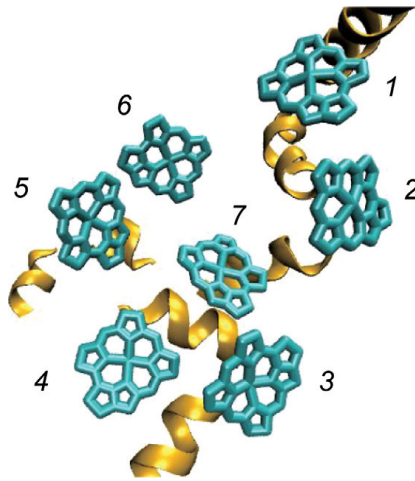
Figure 7.1: Image taken from Ref. [30]. One subunit of a Fenna-Matthews-Olson (FMO) pigment-protein complex, found in green sulfur bacteria. The seven numbered objects are bacteriochlorophyll molecules, each one modeled as a two-level energy site. Excitations can tunnel between sites, and the sites are coupled to molecular vibrations.

set of vibrational modes of the ion crystal may be used simulate a bosonic environment with many degrees of freedom. By coupling a single ion-qubit to the simulated bath, quantum decoherence effects may be experimentally studied in a controlled way.

This Chapter discusses quantum simulation of energy transfer problems using ion chains. In this class of simulations, the qubit states of the ions and the vibrational modes of the crystal are all used as resources. In particular, we study energy transfer between quantum two-level systems which are coupled to each other as well as to a vibrational environment.

This is motivated by considering energy transfer problems in biochemical systems. One canonical example is energy transfer through photosynthetic light-harvesting complexes [30, 1, 10]. In this process, photons are absorbed and converted into molecular excitations. In order to be used as chemical energy in the cell, this excitation must be transferred to a cellular reaction center through a pigment-protein complex (Fig. 7.1). The pigment-protein complex is a collection of pigment molecules typically modeled as two-level systems where the excited state corresponds to energy localized to one particular pigment. The pigments are coupled to each other, as well as to a structured vibrational environment provided by vibrational modes of the molecules. Differences in the site energies of each pigment, as well as the presence of the vibrational environment would intuitively seem to reduce energy transfer efficiency, and so it is surprising to find that the process occurs with near-unity efficiency [30]. It is now believed that the molecular vibrations actually *assist* in the transfer process, providing a source of energy to overcome site energy differences between pigments. This assistance is a rather general phenomenon known as vibrationally assisted energy transfer (VAET).

Owing to the large Hilbert space under consideration, models of these protein-pigment

complexes are difficult to study theoretically. The subunit shown in Fig. 7.1 requires an excitonic Hilbert space of dimension 2^7. The vibrational Hilbert space is in principle infinite because it is described by harmonic oscillators, though in numerical simulations the Hilbert space is truncated. In order to avoid brute-force simulation of the full model, approximation techniques are often applied which rest on various assumptions about the site-site couplings, the site-bath couplings, or relaxation time of the bath [54, 19, 30]. However, these assumptions are not universally valid, and exact numerical treatments of small pigment-protein complex models seem to differ qualitatively from the standard approximation methods [71]. Exact numerical solutions suffer from the exponential scaling problem of classically simulating quantum systems, suggesting a useful role for quantum simulators.

It is not our intention to specifically encode the dynamics of a particular light-harvesting molecule in an ion chain. Rather, we aim to implement the basic models describing the transfer process and study these models in a well-controlled setting. This allows us to gain intuition for what the models predict in various parameter regimes, and in the future to study the validity of approximation schemes. In this work, we focus on vibrationally-assisted energy transfer, and demonstrate the emergence of this phenomenon in a simple two-site system. We show that a quantum environment, represented by a single thermalized harmonic oscillator, can assist in energy transfer between two sites even when the sites exhibit different local energies. We explore this phenomenon by varying the strength of the site-bath coupling, the quantum state of the bath, and the relative detuning between the sites. We find a rich phenomenology even for this simple system, and discuss avenues for extending the experiment to feature more complicated dynamics.

7.2 Model

In particular, we implement VAET through the following Hamiltonian ($\hbar = 1$):

$$H = \frac{\Delta}{2}\sigma_z^{(d)} + \frac{J}{2}\sigma_x^{(d)}\sigma_x^{(a)} + \frac{\kappa}{2}\sigma_z^{(d)}(a + a^\dagger) + \nu_{\text{eff}}a^\dagger a. \tag{7.1}$$

This Hamiltonian describes two-level energy sites, designated donor (d) and acceptor (a), coupled with strength J (see Fig. 7.2(a)). In the absence of additional interactions, this coupling will cause a single excitation to oscillate between the sites with frequency J. A relative energy detuning Δ imposes an energy cost to move excitation between the sites, therefore inhibiting complete transfer of the excitation between sites. Under certain circumstances, the addition of a bosonic environment can aid in the energy transfer process, even when Δ is so large that the transfer would otherwise be almost completely turned off.

The environment is modeled as a harmonic oscillator with frequency ν_{eff} and is coupled to the sites with strength κ. In a semi-classical picture, a site-bath coupling of the form $\frac{\kappa}{2}\sigma_z(a + a^\dagger) + \nu_{\text{eff}}a^\dagger a$ modulates the energy of one site at the vibrational frequency of the environment. κ functions as a modulation index, parametrically moving energy between the sites. In the quantum regime, the role of the environment may be understood as providing an
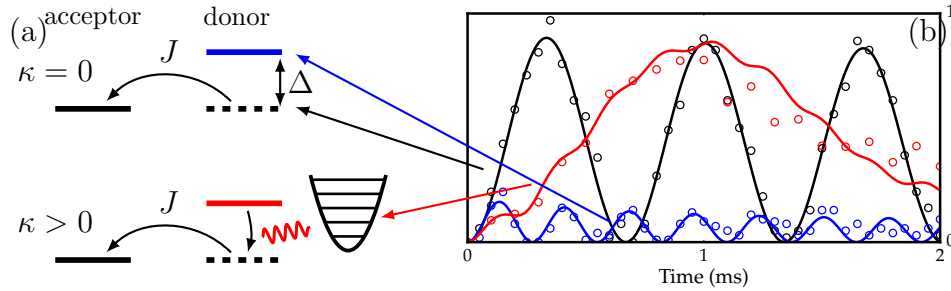
Figure 7.2: **(a)** Schematic illustration of the VAET process. When $\kappa = 0$ (top drawing), the transition probability from the donor state (black line), to the acceptor state (blue line), is attenuated in the presence of an energy barrier Δ between the states. When $\kappa > 0$ (bottom drawing), the system can move between the donor state (solid black line) and the acceptor state (red line), by exchanging energy with a phononic environment. **(b)** Time dynamics of the acceptor state population in three situations illustrated in (a). Black line (theory) and data points: $\Delta = 0$, where coherent energy transfer occurs with frequency J. Blue line (theory) and data points: $\Delta > J$, but without assistance of the phononic environment, reducing transfer efficiency. Red line (theory) and data points: $\Delta > J$, but the environment assists in the transfer process. The process is slower than the resonant coupling, but occurs with high efficiency.

extra degree of freedom which makes the energy transfer process energetically allowed. For instance, if $\nu_{\text{eff}} \approx \sqrt{\Delta^2 + J^2}$, inter-site transfer can occur provided the environment changes its vibrational quantum number by one (see Fig. 7.2(a) and (b)). Higher-order processes also occur: if $\nu_{\text{eff}} \approx \sqrt{\Delta^2 + J^2}/k$, inter-site transfer is allowed when the environment changes by k vibrational quanta.

7.3 Experimental implementation

Our simulator consists of two trapped Ca^+ ions confined in a radio-frequency (RF) Paul trap (Fig. 7.3). In this simulation, we encode the energy sites in the internal electronic state of the ions. The internal structure of Ca^+ is discussed in Sec. 3.1. In particular, the magnetic substates $|S\rangle (m_j = 1/2)$ and $|D\rangle (m_j = 1/2)$ form a qubit, addressed by an optical transition at 729 nm. The combined state $|DS\rangle$ corresponds to a single excitation localized to the donor site, and $|SD\rangle$ corresponds to an excitation localized to the acceptor site. The two-ion crystal contains six normal vibrational modes, only two of which are relevant to implement the Hamiltonian in Equation 7.1: the axial stretch mode with $\omega_{ax} = 2\pi \times 1.3$ MHz, and the radial rocking mode at $\omega_r = 2\pi \times 2.1$ MHz. The axial stretch mode provides a bus to transfer excitation between the two sites via a two-qubit Mølmer-Sørensen quantum interaction [65]. The rocking mode serves as the thermally occupied bosonic environment in the simulation. These modes are defined in Sec. 2.3.
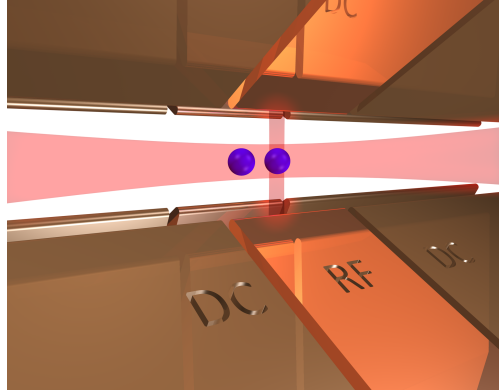
Figure 7.3: Schematic drawing of the 3D trap and laser beams used in this experiment. Two Ca$^+$ ions are confined in the trap. A global 729 nm laser beam along the axis of the trap generates the Mølmer-Sørensen interaction which produces the site-site coupling. A tightly focused laser beam is localized to the donor ion and is used for single ion rotations and generating the site-bath coupling.

We have chosen to use the axial stretch mode and the radial rocking mode (as opposed to the center of mass modes) because of heating rate considerations. The center of mass modes have a heating rate of around 0.1-0.2 quanta/ms. Since the entire simulation takes 2-3 ms to complete, there is a substantial probability to experience heating in the simulation during the interaction time, which would need to be included in the model dynamics. The stretch and rocking modes, however, have a measured heating rate which is smaller by about an order of magnitude, and so we neglect this effect in the simulation dynamics.

The simulation relies on two engineered interactions applied at the same time. The $\sigma_x^{(d)}\sigma_x^{(a)}$ term in Eq. 7.1 is due to a global Mølmer-Sørensen interaction, discussed in Sec. 3.6. This is accomplished via a bichromatic 729 nm laser beam along the axis of the trap. The second engineered interaction is the site-bath coupling, of the form $\sigma_z(a + a^\dagger)$. This is accomplished via a tightly focused laser beam localized to the donor ion. This interaction is discussed in Sec. 3.6. The local beam also contains two laser tones, which are separated in frequency by $\omega_r + \nu_{\text{eff}}$. The laser tone frequencies are shown in Fig. 7.4. The model parameters J and κ are adjusted by controlling the powers of the global and local beams, respectively.

The laser beams are made bichromatic by applying two rf-tones to a single pass acousto-optic modulator (AOM). This is done by combining two frequency sources on a power combiner. Each laser beam can be switched between bichromatic and monochromatic operation by a TTL signal. The electrical and optical layout is discussed in Sec. 4.2 and Fig. 4.9.

The site energy of the donor ion is shifted by Δ relative to the acceptor ion by an AC Stark shift. Currently, this is implemented by adjusting the relative powers of the two tones in the localized beam. It would also be possible to introduce a third tone to the local beam to generate the AC Stark shift. This would have the advantage of allowing the AC Stark
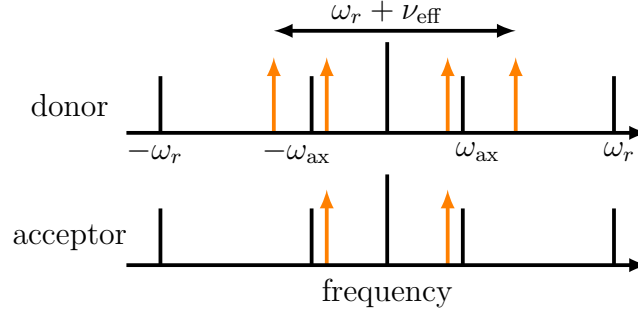
Figure 7.4: Schematic drawing of the laser tone frequencies used to generate the Hamiltonian in Eq. 7.1. The tall black line denotes the optical transition from $|S\rangle \to |D\rangle$. Shorter black lines denote the relevant motional sidebands for the axial and radial modes. Both ions are equally illuminated with the Mølmer-Sørensen laser beam, which contains tones near the red and blue axial sidebands. In addition to this, the acceptor ion has two more tones, detuned from the carrier transition by about $\omega_r/2$, to generate the site-bath coupling.

shift to be tuned independently of κ.

Before each experiment, both the axial center-of-mass and stretch modes are sideband cooled to a mean thermal occupation less than one quantum. The axial center-of-mass mode does not serve a role in the simulation. However, nonzero temperature in this mode causes Doppler broadening of the carrier transition as seen by the Mølmer-Sørensen beam, dephasing the energy transfer between resonant sites. For similar reasons, we also perform sideband cooling of the radial center-of-mass mode, to improve the fidelity of the $\sigma_z(a+a^\dagger)$ interaction. As noted above, the radial rocking mode serves as the environment in the simulation. We control the temperature of this mode by adjusting the duration of sideband cooling (Sec. 3.4). By this method, the mean thermal occupation $\bar{n}$ may be adjusted in the range from $0.04 < \bar{n} < 12$. The Doppler limit for this mode is $\bar{n} = 6$, but by choosing somewhat sub-optimal Doppler cooling parameters, it is possible to prepare the environmental mode above the Doppler limit.

The experimental procedure is as follows: initially, both ions are optically pumped into the state $|SS\rangle$. The assisting mode is then thermalized via sideband cooling as discussed above. The experiment begins by exciting the donor via a local rotation of the donor ion, leading to the combined electronic state $|DS\rangle$. Then, the local and global laser beams generating the model Hamiltonian are applied for a variable time τ_{sim}. Finally, the combined electronic state of both ions is read out on a charged-coupled device (CCD) camera by an electron shelving measurement (Sec. 3.5). For each parameter setting $\{J, \kappa, \Delta, \nu_{\text{eff}}\}$, the simulation is run 100-500 times, and the population in each electronic state is constructed by averaging the results. The probability that the excitation has transferred to the acceptor is the $|SD\rangle$ state population. For the time dynamics data, we report the conditional probability P that the system has undergone state transfer, i.e. $P = P_{DS}/(P_{SD} + P_{DS})$. T

his accounts for population loss in the simulation subspace (primarily due to infidelities in state preparation and off-resonant excitations from the local beam), but does not change the qualitative features of the dynamics.
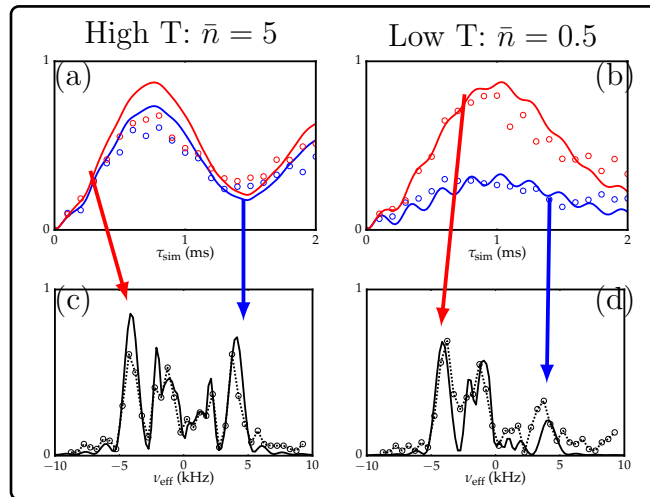
7.4   Results

Figure 7.5: Probability P to find the system to undergo energy transfer to the target state as a function of simulation time τ_{sim} and vibrational frequency ν_{eff}. The upper plots show the time dynamics $P(t)$ with $\nu_{\text{eff}} \approx +4$ kHz (blue points) and $\nu_{\text{eff}} \approx -4$ kHz (red points) for a mean thermal occupation of **(a)** $\bar{n} = 5$ and **(b)** $\bar{n} = 0.5$. The lower plots show P as a function of ν_{eff}, where the simulation time is fixed to 0.7 ms for a mean thermal occupation **(c)** $\bar{n} = 5$ and **(d)** $\bar{n} = 0.5$. For all cases, $(J, \kappa, \Delta) = 2\pi \times (1.30(1), 1.40(4), 4.00(2))$ kHz In the time traces, the solid lines are a numerical simulation of the system dynamics where all parameters were determined through independent calibration measurements. The solid lines in the spectral plots are also a numerical solution where a small overall shift to the frequencies is adjusted to correct a systematic measurement offset in the ion's vibrational frequencies. The measured data points in the spectral plots are connected with a dashed line to guide the eye

We probe the VAET phenomenon through spectroscopy as well as study its time dynamics. For the spectroscopic measurements, we fix particular values of J, κ, Δ, and simulation time τ_{sim}. We vary the frequency ν_{eff} and measure the probability to find the ions in the acceptor state $|SD\rangle$. VAET is most clearly illustrated in the regime $\Delta \gg J$, such that inter-site energy transfer does not occur without the assistance of the environment. This situation is shown in Fig. 7.5, where significant energy transfer occurs within 1 ms, with the appropriate environmental frequency.
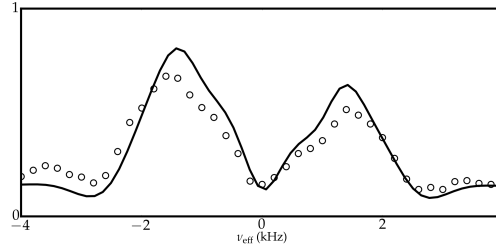
Figure 7.6: Acceptor state population vs ν_{eff}. A typical detuning scan in the small Δ regime, showing only two peaks. In this case, $\tau_{\text{sim}} = 0.7$ ms and $\bar{n} = 2.7$. The other parameters are: $(J, \kappa, \Delta) = 2\pi \times (1.22(3), 0.63(2), 1.226(3))$ kHz. system for independently measured parameters.

In the spectral scans, (Fig. 7.5(c) and (d)), several peaks are visible. The first peak, at around $\nu_{\text{eff}} = -2\pi \times 4$ kHz, corresponds to a process wherein the system goes from $|DS, n\rangle \to |SD, n+1\rangle$, where n indexes the vibrational quantum number of the environment. The next set of peaks, not fully resolved, correspond to processes where the environment gains $k > 1$ vibrational quanta, $|DS, n\rangle \to |SD, n+k\rangle$.

As ν_{eff} crosses zero, the environment goes from *gaining* energy to *losing* energy in the transfer process. The peaks at $\nu_{\text{eff}} > 0$ correspond to processes $|SD, n\rangle \to |DS, n-k\rangle, k \geq 1$. The height asymmetry between the $\nu_{\text{eff}} < 0$ and $\nu_{\text{eff}} > 0$ peaks is a signature of the quantum nature of the environment. The asymmetry emerges when the environment has significant population in the $n = 0$ ground state. In that case, inter-site transfer is suppressed because the environment cannot provide the necessary energy. The peak height asymmetry begins to disappear as the thermal occupation of the environment is increased. This is seen experimentally by comparing Fig. 7.5(c), where the environment contains an average of 5 vibrational quanta, to Fig. 7.5(d), where the environment has mean thermal occupation of 0.5 quanta. The asymmetry is much more pronounced in the lower temperature data. Correspondingly, for the high temperature data, the time dynamics of the process is nearly identical for either sign of ν_{eff} (Fig. 7.5(a)). Meanwhile, at low temperature, the transfer efficiency is much lower for positive ν_{eff}.

For Δ sufficiently large, each process $|SD, n\rangle \to |DS, n+k\rangle$ is resolved and occurs at a different frequency, as shown in Fig. 7.5 (b) and (d). However, when Δ becomes comparable to J, these processes all occur simultaneously, and numerical methods are then required to study the dynamics. In this case, as shown in Fig. 7.6, the peaks corresponding to changes in the environmental quantum number are no longer spectrally resolved.

In the small Δ configuration, the dynamics of the process changes appreciably as the environmental coupling κ and the temperature are varied. These changes are most apparent when the system is prepared near the motional ground state (Fig. 7.7). For comparison, we run the simulation for three different values of κ. For small κ, the excitation transfer is modulated by the environmental coupling, as can be seen in the time dynamics. As κ is increased, the transfer speed increases but also changes qualitatively. In contrast to the pure
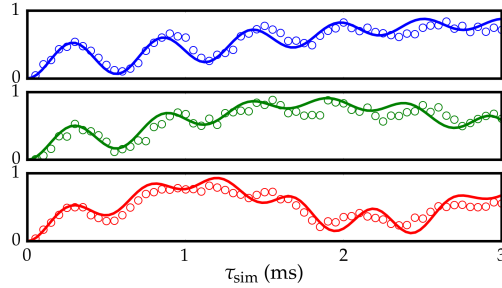
Figure 7.7: Probability P for energy transfer vs simulation time for different values of κ, with the environmental mode prepared to a mean thermal occupation $\bar{n} = 0.04$ vibrational quanta. In all three scans, all parameters except κ are approximately constant. Ordered from top to bottom: $J = 2\pi \times (1.27(3), 1.22(3), 1.32(3))$ kHz $\Delta = 2\pi \times (1.22(3), 1.24(3), 1.36(4))$ kHz, $\nu_{\text{eff}} = -2\pi \times (1.71(5), 1.69(5), 1.77(6))$ kHz. κ increases from top to bottom, taking the respective values $2\pi \times (0.229(6), 0.37(1), 0.64(2))$ kHz. In all plots, the solid traces are the predicted dynamics with no free parameters.
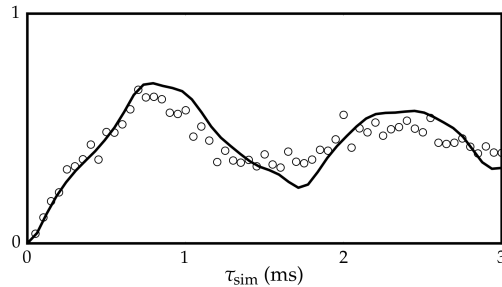

Figure 7.8: Probability P for energy transfer vs. τ_{sim} in the high temperature ($\bar{n} = 12$) regime. Simulation parameters: $(J, \kappa, \Delta, \nu_{\text{eff}}) = 2\pi \times (1.17(3), 0.63(2), 1.59(3), -1.72(6))$ kHz

state dynamics of the system, finite temperature both increases transfer speed and damps the oscillatory behavior of the dynamics (Fig. 7.8).

7.5 Calibration of parameters

An important component of a quantum simulator is the ability to independently measure the model parameters. In Eq. 7.1 the parameters which must be determined are J, κ, Δ, and ν_{eff}. In addition, the initial thermal population of the environment must be measured.

Measuring J

The easiest parameter to measure is J. This is done by turning the local beam off during the simulation, effectively setting $\Delta = \kappa = 0$. The two-ion system is then prepared in the combined state $|DS\rangle$ via a local rotation of the donor ion, and the electronic populations are measured on a CCD camera (see Fig. 3.8). The data are fit by a least- squares method to extract J.

Measuring κ

κ is somewhat more difficult to measure than J, especially for small values. In principle, it would suffice to measure κ with the Ramsey method discussed in Sec. 3.6. In that discussion, a $\pi/2$ pulse prepares a single ion in the state $|S\rangle + |D\rangle$. After this, the bichromatic beams are turned on for some time, and a second $\pi/2$ pulse is applied, followed by state measurement in the $|S\rangle$, $|D\rangle$ basis. The decay of the Ramsey fringe contrast in this measurement in principle measures κ, but this effect must be disentangled from other decoherence sources such as magnetic field fluctuations which occur on the same timescale. In our case, the electronic state coherence is around 2 ms [51].

To avoid this complication, we instead use Eq. 3.38, making the association

$$\kappa = \eta_r \frac{\Omega_1 \Omega_2}{2\omega_r}, \tag{7.2}$$

where η_r is the Lamb-Dicke parameter for the local beam onto the radial rocking mode, and $\Omega_{(1,2)}$ are the Rabi frequencies of the two laser fields in the local beam.

η_r is measured by sideband cooling the ω_r mode near the ground state, and then measuring the frequency of Rabi oscillations on the blue sideband. For the geometry in this experiment, we find $\eta_r = 0.039(1)$.

Once η_r is known, the Rabi frequencies of each tone must be measured. It is helpful at this point to recall Fig. 4.9. Each 729 nm laser path goes first through a double pass AOM setup, and then through a single pass AOM before arriving at the trap. The double pass AOM provides wide band frequency control of the beam, while the single pass AOM is used to make the laser beam bichromatic. To measure the Rabi frequencies in each tone, the ω_r mode is first sideband cooled. Following this preparation step, the local beam is switched to bichromatic mode, but the double pass AOM driving frequency is shifted by $+\omega_r/2$, such that one tone of the bichromatic beam is resonant to the carrier transition, and the frequency of Rabi oscillations is Ω_1. Then, the process is repeated, but the double pass AOM driving frequency is shifted by $-\omega_r/2$, and then the frequency of carrier Rabi oscillations is Ω_2. In each of these measurements, one tone of the bichromatic beam is resonant to the carrier, and the other is resonant to either the blue or red sideband. The presence of the tone driving the sideband affects the dynamics only slightly because the sideband Rabi frequency is less than 4% that of the carrier with the mode in the ground state. In addition, a small shift of the double pass frequency by a few kHz will greatly reduce
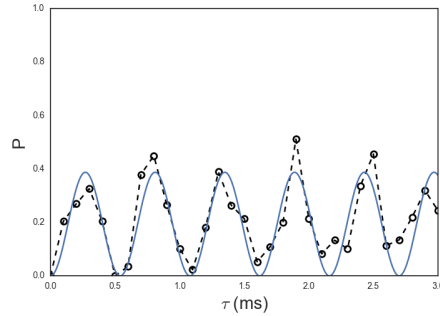
Figure 7.9: Energy transfer probability P vs. simulation time for the small Δ regime, and $\nu_{\text{eff}} = 2\pi \times 30$ kHz. In this case, $J = 2\pi \times 1.4$ kHz, $\Delta = 2\pi \times 1.1$ kHz. The line is a fit to the model in Eq. 7.3.

the driving of the sideband while hardly affecting the rate of carrier Rabi oscillations. One remaining systematic effect is the change in double pass diffraction efficiency as a function of the driving frequency. In the calibration measurements, the double pass frequency is shifted $\pm \omega_r/2$ relative to its frequency when the simulation is run. The intensity change is measured on a photodiode to be around 5%, and is introduced as a correction factor in determining $\Omega_{(1,2)}$. These measurements are sufficient to determine κ, which may be tuned from 0 up to around 1.5 kHz. The measurement errors in κ (listed in Sec. 7.4) arise from the uncertainty in η, as well as the error in fitting Rabi oscillations from $\Omega_{(1,2)}$. The primary factor limiting κ is that the Rabi frequencies of the individual tones must be small as compared to their detuning from the carrier transition ($2\pi \times$ MHz) so as not to induce off-resonant excitations. For the largest values ($\kappa = 2\pi \times 1.7$ kHz), $\Omega_{(1,2)} \approx 2\pi \times 300$ kHz.

Measuring Δ

Δ is measured in two different ways. For Δ not too large as compared to J, it can be measured by the following procedure. First, one tone of the $\sigma_z(a + a^\dagger)$ interaction is shifted by $+2\pi \times 30$ kHz from $\omega_r/2$. This has the effect of setting $\nu_{\text{eff}} = 2\pi \times 30$ kHz–much larger than Δ. We thus expect that κ does not contribute to the dynamics, and the model Hamiltonian reduces to

$$H = \frac{J}{2}\sigma_x^{(d)}\sigma_x^{(a)} + \frac{\Delta}{2}\sigma_z^{(d)}. \tag{7.3}$$

The ions are first prepared into the state $|DS\rangle$, and then both the global and local beams are turned on. The population in the acceptor state $|SD\rangle$ is measured as a function of time. The acceptor state population is modeled using a quantum dynamics solver [36] for the Hamiltonian in Eq. 7.3. The model is then fit by least-squares to find Δ (see Fig. 7.9).

This method introduces a systematic error which must be accounted for, however. The shift of one laser tone by about 30 kHz relative to its frequency during the actual simulation
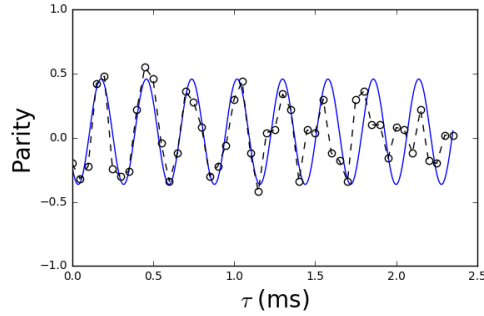
Figure 7.10: Parity oscillations of the two-ion electronic state. The local beam is on, but the global beam, generating the Mølmer-Sørensen coupling is left off so as not to interfere with the parity oscillations. The solid line is a fit to determine $\Delta = 2\pi \times 3.6$ kHz.

introduces an additional AC Stark shift of up to 200 Hz which is not present when the simulation is actually run. At present, this is corrected in an analytic way. The residual Stark shift Δ_r is calculated using a two-level atom approximation (Eq. 3.28):

$$\Delta_r = \frac{\Omega_1^2}{2}\left(\frac{1}{\omega_r/2} - \frac{1}{\omega_r/2 + 2\pi \times 30 \text{ kHz}}\right). \tag{7.4}$$

Ω_1 is assumed to have already been measured in the previous section. A better method would be to repeat the measurement but in the second iteration, shift the frequency by -30 kHz, and take the average of the measured detunings.

When $\Delta \gg J$, the population transfer is too small to fit for the detuning. In that case, Δ must be measured directly via parity oscillations [11]. First, a global $\pi/2$ pulse is applied to both ions. Then the bichromatic local beam is turned on, generating detuning Δ, but the global beam (which does not generate local Stark shifts) is left off. After an interrogation time τ, a second $\pi/2$ pulse is applied, and the resulting combined electronic state is measured, and the parity P is recorded. The operator P is defined as $P(|SS\rangle) = P(|DD\rangle) = 1$. $P(|SD\rangle) = P(|DS\rangle) = -1$. The parity $P(\tau)$ oscillates with frequency Δ, and so the parity oscillations are used to extract this parameter (Fig. 7.10). Coupling to the environmental mode does not cause phase contrast loss of the parity oscillations because $\nu_{\text{eff}} = 2\pi \times 30$ kHz is much larger than the other relevant parameters (J, Δ). Therefore, contributions from this coupling quickly average to zero in the dynamics.

Remaining parameters

The only parameters left to determine are the thermal occupation of the environmental mode, and the effective mode frequency ν_{eff}. The thermal occupation is extracted from sideband spectroscopy (see Sec. 3.4) when the thermal excitation is low (less than 2 quanta). Otherwise, the temperature is measured by comparing Rabi oscillations on the carrier and blue sideband at the same laser power.

The environmental simulated frequency ν_{eff} is defined in an interaction picture rotating with frequency $\omega_r + \nu_{\text{eff}}$. In this interaction picture, the Hamiltonian takes the form of Eq. 7.1. The parameter ν_{eff} is then given by ω_r minus the frequency splitting of the two tones in the localized beam. In principle, it is therefore possible to determine this parameter just by measuring ω_r to high precision. In the experiment, the spectral scans are performed by varying a frequency source around $\omega_r/2$. However, over the course of taking a full set of data over several hours, ω_r may change by up to 2 kHz. In order to avoid the additional measurement overhead of tracking this parameter closely, the x-axis in the spectral scans is adjusted so that the peak locations are symmetric about zero. The time scans are taken by setting ν_{eff} to the outermost peaks.

7.6 Conclusions and future work

We have implemented an analog quantum simulation of vibrationally-assisted energy transfer using trapped calcium ions, and studied dynamics across a range of parameter regimes, including non-perturbative and non-Markovian dynamics. Our experimental results show good agreement with brute-force numerical solution of the model. This experiment is a building block towards a device for studying charge and energy transfer dynamics in more complex models relevant to chemistry and biology. There are a number of directions in which to extend this experiment. First, one can increase the complexity of the environment in order to more closely mimic biochemical vibrational environments. The single quantized harmonic mode implemented here models a long-lived resonant vibrational mode; it is possible to couple the vibrational mode to a thermal bath via laser cooling, thus allowing one to tailor the relaxation dynamics of the mode, and tune the system-environment dynamics continuously from a non-Markovian to a Markovian regime. This would require embedding the simulation in a large string of ions, where sideband cooling of the environmental modes is applied to ancillary ions which do not participate in the simulation [27]. The use of ancillary ions allows the explicit introduction of dissipation into the simulation without affecting the electronic coherences of the simulation ions.

Also, by coupling to other vibrational modes in the ion crystal, one can add additional long-lived vibrational modes to the structured environment. Finally, one can engineer additional dephasing dynamics due to coupling to a high-temperature structureless bath by adding fluctuations to the laser tone implementing the energy shift (Δ) using a fast arbitrary waveform generator. Another direction for extending the simulation model is to add more ions to mimic energy transfer in larger networks; understanding energy transfer in large networks of varying morphology and energetic structure is critical to understanding non-trivial transport behavior such as "quantum ratcheting" [29, 47], and designing excitonic materials and devices [3]. In larger networks it may also be possible to simulate the dynamics and propagation of multiple excitations (this depends on the complexity of the exciton-exciton interaction one requires).

Overall, all of these extensions are achievable with current experimental technology. Each

additional site in the network requires exactly one additional trapped ion. The coupling to an additional vibrational mode requires two additional localized 729 nm laser tones, necessitating an approximately linear increase in total laser power for constant couplings. The required single-ion addressability with individual beams has been demonstrated, even for a large chain of ions [15].

We thus believe that with moderate experimental improvements our approach can be used to study models of energy transfer in physics, chemistry and biology, where analytical and numerical treatments fail. This regime will be particularly interesting since the lack of a theoretical prediction will not allow for an independent confirmation of the experimental results.

Chapter 8

Conclusions

This document began this work with a general overview of ion trapping technology (**Chapter 2**). That Chapter discussed two types of rf Paul traps: the microfabricated surface trap and the macroscopic, 3-dimensional Paul trap. We discussed how the dc potential near the trapping region may be controlled, and slightly generalized the treatment to consider the case of two ions in the same trap.

In **Chapter 3**, we explored the interaction of laser light with trapped ions. Lasers are a primary toolbox for controlling the quantum states of ions. In the experiments, we use basic light-matter interactions for Doppler cooling, sideband cooling nearly to the ground state of motion, and projective measurement of the electronic state. We can also do coherent operations on the narrow $|S\rangle \to |D\rangle$ transition, in which the ion can be rotated into a coherent superposition of $|S\rangle$ and $|D\rangle$. At a somewhat more complicated level, we create entangled states of two ions by applying bichromatic laser beams. The experimental hardware to do all of these manipulations is described in **Chapter 4**.

We extend the optical toolbox in **Chapter 5**, in which we parametrically couple two vibrational modes of a single ion. This extends on laser-based control of the ion motion by creating a completely electronic means of manipulating the motional quantum state. The coupling is accomplished by applying a time-varying voltage with frequency $\omega_p = \omega_i - \omega_j$, where $\omega_{(i,j)}$ are the frequencies of two arbitrarily chosen vibrational modes.

With a single ion, this parameteric technique is useful for cooling modes which have only a small projection onto the wave-vector of the cooling laser. In addition, it can be used to measure the quantum state of an optically inaccessible mode by first swapping the state of the inaccessible mode with an optically accessible mode and then performing standard optical analysis of the accessible mode. As an example of this, we use this technique to measure a heating rate in an inaccessible mode. In principle, the technique can be extended to couple arbitrary normal modes of a Coulomb crystal, although this would require that the potential created by the coupling electrode has substantial variation on the scale of the ion-ion separation–an engineering challenge. However, microfabricated traps have been used to split ion strings with dc potentials [5], proving that it is possible to make electrodes featuring the required spatial potential variation. Another extension of the work is in the generation

of non-classical states of motion. By setting the driving frequency $\omega_p = \omega_i + \omega_j$, the sum frequency between two modes, the interaction generates two-mode squeezing.

Two experiments studying surface noise effects were shown in **Chapter 6**. In the first experiment, we showed that technical noise, for instance arising from noisy voltage sources, can be experimentally differentiated from surface noise sources. This allows the experimenter to know whether the electrical noise observed in the experiment is most likely due to technical sources, and therefore whether more work should be done to improve the electronics. It will be valuable to perform this test in experiments which aim to study surface noise so that technical noise can be ruled out.

In the second experiment, we studied dephasing of the ion motion. We found that the motional phase coherence is lost after about 5 ms. We believe that this is due to surface effects, as technical noise measurements did not seem sufficient to explain the observed dephasing. Whereas heating rate measurements probe electrical noise at frequencies resonant to the ion motion, our measurements probe noise at very low frequencies (sub-Hz to kHz). Many theoretical noise models predict a power-law scaling of the surface noise which rolls off to a flat frequency spectrum below a certain cutoff frequency. In the models the cutoff frequency depends on the noise dynamics and therefore our measurements help discriminate between competing theoretical models. However, our measurements are difficult to explain by common physical models such as surface adsorption of atomic contaminants.

It will be useful to combine the experiment with surface-cleaning methods to see how the dephasing time changes with surface treatment, thereby proving that surface noise is indeed primarily responsible for the dephasing. In addition, it may also be interesting perform these measurements while the trap surface is heated, as the surface adsorbate model contains a temperature-dependent low-frequency cut-off. Regardless of the physical origin, we believe that these effects will pose a strong challenge to the miniaturization of surface trap technology for quantum information processing experiments. This is due to to the expected d^{-6} scaling of the dephasing noise. Our measurements were conducted in a trap where the ion was located $d = 50$ μm above the trap surface. With a 25 μm trapping height, we expect the dephasing time to be 64 times smaller. Thus, an analogous experiment in a 25 μm trap would be expected to show a dephasing time of less than 100 μs–comparable to the time required to perform two-qubit quantum gates.

The final experiment in this work is documented in **Chapter 7**. In this experiment, we implemented vibrationally assisted energy transfer in a two-ion system. The electronic levels of the ions were used to simulate energy sites. The state $|DS\rangle$ corresponded to an excitation localized to one ion (called the donor), and $|SD\rangle$ corresponded to an excitation localized on the other ion (called the acceptor). The two energy sites were coupled together by a Mølmer-Sørensen interaction, and an ac Stark shift detuned the $|SD\rangle$ level from the $|DS\rangle$ level, inhibiting transfer between the sites. By coupling the energy sites to a vibrational mode of the ion crystal with an interaction of the form $\sigma_z(a + a^\dagger)$, we showed that energy transfer can be enhanced if the vibrational mode is resonant to the energy gap between donor and acceptor sites.

The system mimics aspects of energy transfer processes in biochemical systems such as

pigment-protein complexes. In this analogy, a vibrational mode of the ion crystal mimics the effect of a molecular vibration on energy transport through the pigment-protein complex. We explore how the dynamics changes as a result of the model parameters. For instance, we show results for both large and small site detunings (as compared with the site-site coupling). We showed a dependence of the transport dynamics as the temperature of the vibrational mode is varied.

This experiment should be thought of as a proof-of-principle experiment, showing that it is experimentally viable to use trapped ions to emulate energy transfer in the presence of a thermalized vibrational environment. It will be interesting to extend the simulation along several different directions. For instance, by applying amplitude noise to the ac Stark shifting laser, it will be possible to explicitly introduce decoherence to the system in a controlled way. The dynamics must then be treated in an open quantum system formalism, and the crossover from Markovian dynamics (where quantum correlations in the environmental mode are long lived) to non-Markovian dynamics (where the environment has no memory time) can be explored experimentally. To be of more scientific value, it will be important to make the system more complex than can be simulated with classical computational resources. In this way, energy transfer dynamics can be controllably studied in a system which cannot be simulated by other means, potentially leading to new insights. This is primarily accomplished by adding more ions and more vibrational modes. Extending the simulation to include extra vibrational modes involves adding one additional localized bichromatic laser beam per mode, generating the appropriate vibrational couplings. With more ions, it may be possible to new qualitative effects such as "quantum ratcheting," in which the energy only flows in one direction along the ion string [47, 29]. We believe it will be possible for our simulation to approach the limits of classical supercomputers with reasonable experimental improvements. For instance, a five site model where each site is coupled to two harmonic modes may already be beyond classical resources. If each of the harmonic modes is thermalized to a mean thermal occupation $\bar{n} \sim 5$, then a Hilbert space of about 15 states is required to simulate each harmonic oscillator. In that case, the Hilbert space required to simulate the entire system is $2^5 \times 15^{10} \approx 2 \times 10^{13}$. By incrementally increasing the simulation complexity, and verifying at each level that the experiment performs as expected, it may be possible to construct a quantum simulator which truly probes previously unknown physics.

Bibliography

[1] Julia Adolphs and Thomas Renger. "How Proteins Trigger Excitation Energy Transfer in the FMO Complex of Green Sulfur Bacteria". In: *Biophysical Journal* 91.8 (Oct. 2006), pp. 2778–2797. ISSN: 00063495. DOI: 10.1529/biophysj.105.079483.

[2] Nitzan Akerman et al. "Universal gate-set for trapped-ion qubits using a narrow linewidth diode laser". In: *New Journal of Physics* 17.11 (2015). ISSN: 13672630. DOI: 10.1088/1367-2630/17/11/113060. arXiv: 1505.02503.

[3] Gleb M Akselrod et al. "Probing the mechanisms of large Purcell enhancement in plasmonic nanoantennas". In: (2014). DOI: 10.1038/NPHOTON.2014.228.

[4] D T C Allcock et al. "Heating rate and electrode charging measurements in a scalable, microfabricated, surface-electrode ion trap". In: *Applied Physics B* 107.4 (2012), pp. 913–919. ISSN: 0946-2171. DOI: 10.1007/s00340-011-4788-5.

[5] M D Barrett et al. "Deterministic quantum teleportation of atomic qubits." In: *Nature* 429 (2004), pp. 737–739. DOI: 10.1038/nature02608.

[6] DJ Berkeland et al. "Minimization of ion micromotion in a Paul trap". In: *Journal of Applied Physics* 83.10 (1998), p. 5025.

[7] R. Blatt and C. F. Roos. "Quantum simulations with trapped ions". In: *Nature Physics* 8.4 (Apr. 2012), pp. 277–284. ISSN: 1745-2473. DOI: 10.1038/nphys2252.

[8] B. H. Bransden and C. J. Joachain. *Quantum Mechanics*. 2nd Editio. Addison-Wesley, 2000.

[9] M Brownnutt et al. "Ion-trap measurements of electric-field noise near surfaces". In: *Reviews of Modern Physics* 87.4 (2015), pp. 1419–1482. ISSN: 0034-6861. DOI: 10.1103/RevModPhys.87.1419.

[10] A W Chin et al. "The role of non-equilibrium vibrational structures in electronic coherence and recoherence in pigment-protein complexes". In: *Nature Physics* 9.2 (Feb. 2013), pp. 113–118.

[11] M. Chwalla et al. "Precision spectroscopy with two correlated atoms". In: *Appl. ˜Phys. ˜B* 89.4 (Nov. 2007), p. 483. ISSN: 0946-2171. DOI: 10.1007/s00340-007-2867-4.

[12]   Eric A Cornell et al. "Mode coupling in a Penning trap: π pulses and a classical avoided crossing". In: *Physical Review A* 41.1 (Jan. 1990), pp. 312–315. ISSN: 1050-2947. DOI: 10.1103/PhysRevA.41.312.

[13]   N. Daniilidis et al. "Surface noise analysis using a single-ion sensor". In: *Physical Review B* 89.24 (June 2014), p. 245435. ISSN: 1098-0121. DOI: 10.1103/PhysRevB.89.245435.

[14]   N Daniilidis et al. "Wiring up trapped ions to study aspects of quantum information". In: *J. Phys. B* 42.15 (2009), p. 154012. ISSN: 0953-4075. DOI: 10.1088/0953-4075/42/15/154012.

[15]   S. Debnath et al. "Demonstration of a small programmable quantum computer with atomic qubits". In: *Nature* 536.7614 (Aug. 2016), pp. 63–66. ISSN: 0028-0836. DOI: 10.1038/nature18648.

[16]   H G Dehmelt. "Proposed $10^{14}\Delta\nu > \nu$ Laser Fluorescence Spectroscopy on Tl$^+$ Mono-Ion Oscillator II". In: *Bull. Am. Phys. Soc.* 20.5 (1975), p. 60.

[17]   R. Dubessy, T. Coudreau, and L. Guidoni. "Electric field noise above surfaces: A model for heating-rate scaling law in ion traps". In: *Physical Review A* 80.3 (Sept. 2009), p. 031402. ISSN: 1050-2947. DOI: 10.1103/PhysRevA.80.031402.

[18]   C. J. Foot. *Atomic Physics*. Oxford Univ. Press, 2005.

[19]   Th. Förster. "Zwischenmolekulare Energiewanderung und Fluoreszenz". In: *Annalen der Physik* 437.1-2 (1948), pp. 55–75. ISSN: 00033804. DOI: 10.1002/andp.19484370105.

[20]   Alexander Franzen. *ComponentLibrary*. http://www.gwoptics.org/ComponentLibrary/.

[21]   C. C. (Christopher C.) Gerry and Peter (Peter L.) Knight. *Introductory quantum optics*. Cambridge University Press, 2005, p. 317. ISBN: 052152735X.

[22]   M. A. Gesley and L. W. Swanson. "Spectral analysis of adsorbate induced field-emission flicker noise". In: *Phys Rev B* 32.12 (1985), pp. 7703–7712.

[23]   Dylan J Gorman et al. "Two-mode coupling in a single-ion oscillator via parametric resonance". In: *Physical Review A* 89.6 (June 2014), p. 062332. ISSN: 1050-2947. DOI: 10.1103/PhysRevA.89.062332.

[24]   H. Häffner et al. "Precision measurement and compensation of optical Stark shifts for an ion-trap quantum processor." In: *Phys. Rev. Lett.* 90 (2003), p. 143602.

[25]   Fredric J Harris. "On the use of windows for harmonic analysis with the discrete Fourier transform". In: *Proc. IEEE* 66 (1978), pp. 51–83.

[26]   D J Heinzen and D J Wineland. "Quantum-limited Cooling and Detection of Radio-Frequency Oscillations by Laser-cooled Ions". In: *Phys. Rev. A* 42 (1990), p. 2977.

[27]   M. Herrmann et al. "Frequency Metrology on Single Trapped Ions in the Weak Binding Limit: The $3s_{1/2} - 3p_{3/2}$ Transition in ^{24}Mg$^+$". In: *Phys. Rev. Lett.* 102 (1 Jan. 2009), p. 013006. DOI: 10.1103/PhysRevLett.102.013006.

[28]   D A Hite et al. "100-Fold Reduction of Electric-Field Noise in an Ion Trap Cleaned with In Situ Argon-Ion-Beam Bombardment". In: *Phys Rev Lett* 109 (2012), p. 103001. arXiv: `arXiv:1112.5419v1`.

[29]   Stephan Hoyer, Akihito Ishizaki, and K Birgitta Whaley. "Spatial propagation of excitonic coherence enables ratcheted energy transfer". In: *PHYSICAL REVIEW E* 86 (2012). DOI: `10.1103/PhysRevE.86.041911`.

[30]   Akihito Ishizaki and Graham R Fleming. "Theoretical examination of quantum coherence in a photosynthetic system at physiological temperature." In: *Proceedings of the National Academy of Sciences of the United States of America* 106.41 (2009), pp. 17255–17260. ISSN: 0027-8424. DOI: `10.1073/pnas.0908989106`. arXiv: `arXiv:1408.1149`.

[31]   R Islam et al. "Onset of a quantum phase transition with a trapped ion quantum simulator." In: *Nature communications* 2 (Jan. 2011), p. 377. ISSN: 2041-1723. DOI: `10.1038/ncomms1374`. arXiv: `1103.2400`.

[32]   J D Jackson. *Classical Electrodynamics*. 3rd editio. John Wiley \& Sons, New York, 1998.

[33]   D.F.V. James. "Quantum dynamics of cold trapped ions with application to quantum computation". In: *Applied Physics B: Lasers and Optics* 66.2 (Feb. 1998), pp. 181–190. ISSN: 0946-2171. DOI: `10.1007/s003400050373`.

[34]   E. T. Jaynes and F. W. Cummings. "Comparison of Quantum and Semiclassical Radiation Theories with Application to the Beam Maser". In: *Proceedings of the IEEE* 51.1 (1963), pp. 89–109. ISSN: 15582256. DOI: `10.1109/PROC.1963.1664`.

[35]   Jian Jin and D. Church. "Precision lifetimes for the Ca$^+$ 4p 2P levels: Experiment challenges theory at the 1\% level". In: *Physical Review Letters* 70.21 (May 1993), pp. 3213–3216. ISSN: 0031-9007. DOI: `10.1103/PhysRevLett.70.3213`.

[36]   J.R. R Johansson, P.D. D Nation, and Franco Nori. "QuTiP: An open-source Python framework for the dynamics of open quantum systems". In: *Computer Physics Communications* 183.4 (Apr. 2013), pp. 1760–1772. ISSN: 00104655. DOI: `10.1016/j.cpc.2012.02.021`. arXiv: `arXiv:1110.0573v2`.

[37]   K G Johnson et al. "Active stabilization of ion trap radiofrequency potentials". In: *Review of Scientific Instruments* 87.5 (May 2016), p. 53110. DOI: `10.1063/1.4948734`.

[38]   K Kim et al. "Geometric phase gate on an optical transition for ion trap quantum computation". In: *Phys.˜Rev.˜A* 77 (2008), p. 50303.

[39]   K Kim et al. "Quantum simulation of frustrated Ising spins with trapped ions". In: *Nature* 465.7298 (2010), pp. 590–593.

[40]   G Kirchmair et al. "Deterministic entanglement of ions in thermal states of motion". In: *New J. Phys.* 11 (2009), p. 23002.

[41]   A Kreuter et al. "Experimental and theoretical study of the 3d^{2}D level lifetimes of ^{40}Ca^{+}". In: *Physical Review A* 71.3 (Mar. 2005), p. 32504. ISSN: 1050-2947. DOI: 10.1103/PhysRevA.71.032504.

[42]   A. J. Leggett et al. "Dynamics of the dissipative two-state system". In: *Rev. Mod. Phys.* 59.1 (Jan. 1987), pp. 1–85. ISSN: 0034-6861. DOI: 10.1103/RevModPhys.59.1.

[43]   D. Leibfried et al. "Quantum dynamics of single trapped ions". In: *Reviews of Modern Physics* 75.1 (Mar. 2003), pp. 281–324. ISSN: 0034-6861. DOI: 10.1103/RevModPhys.75.281.

[44]   Gebhard Littich. "Electrostatic Control and Transport of Ions on a Planar Trap for Quantum Information Processing". In: (2011).

[45]   Guang Hao Low, Peter Herskind, and Isaac Chuang. "Finite-geometry models of electric field noise from patch potentials in ion traps". In: *Physical Review A* 84.5 (Nov. 2011), p. 053425. ISSN: 1050-2947. DOI: 10.1103/PhysRevA.84.053425.

[46]   D M Meekhof et al. "Generation of nonclassical motional states of a trapped atom." In: *Phys. Rev. Lett.* 76 (1996), pp. 1796–1799.

[47]   C R Myers, G J Milburn, and J Twamley. "Vibrationally assisted quantum energy pumps". In: *New Journal of Physics* 17.9 (Sept. 2015), p. 093030. ISSN: 1367-2630. DOI: 10.1088/1367-2630/17/9/093030.

[48]   Wolfgang Paul. "Electromagnetic traps for charged and neutral particles". In: *Reviews of Modern Physics* 62.3 (July 1990), pp. 531–540. ISSN: 0034-6861. DOI: 10.1103/RevModPhys.62.531.

[49]   D. Porras and J. I. Cirac. "Effective Quantum Spin Systems with Trapped Ions". In: *Physical Review Letters* 92.20 (May 2004), p. 207901. ISSN: 0031-9007. DOI: 10.1103/PhysRevLett.92.207901.

[50]   D. Porras et al. "Mesoscopic spin-boson model of trapped ions". In: *Phys Rev A* 78 (2008), p. 10101.

[51]   Thaned Pruttivarasin. "Spectroscopy , fundamental symmetry tests and quantum simulation with trapped ions". PhD thesis. University of California, Berkeley, 2014, p. 141.

[52]   Michael Ramm. "Quantum Correlations and Energy Transport in Trapped Ions". PhD thesis. University of California, Berkeley, 2014.

[53]   Michael Ramm et al. "Precision Measurement Method for Branching Fractions of Excited P$_{1/2}$ States Applied to ^{40}Ca^{+}". In: *Physical Review Letters* 111.2 (July 2013), p. 023004. ISSN: 0031-9007. DOI: 10.1103/PhysRevLett.111.023004.

[54]   A G Redfield. "On the Theory of Relaxation Processes". In: *IBM Journal of Research and Development* 1.1 (1957), pp. 19–31. ISSN: 0018-8646. DOI: 10.1147/rd.11.0019.

[55]   M Riebe et al. "Process tomography of ion trap quantum gates". In: *Phys. Rev. Lett.* 97 (2006), p. 220407.

[56] Christian Roos. "Controlling the quantum state of trapped ions". PhD thesis. University of Innsbruck.

[57] Christian F Roos. "Ion trap quantum gates with amplitude-modulated laser beams". In: *New Journal of Physics* 10.1 (Jan. 2008), p. 013002. ISSN: 1367-2630. DOI: 10. 1088/1367-2630/10/1/013002.

[58] C A Sackett et al. "Experimental entanglement of four particles". In: *Nature* 404 (2000), pp. 256–259.

[59] A. Safavi-Naini et al. "Influence of monolayer contamination on electric-field-noise heating in ion traps". In: *Physical Review A* 87.2 (Feb. 2013), p. 023421. ISSN: 1050-2947. DOI: 10.1103/PhysRevA.87.023421.

[60] A. Safavi-Naini et al. "Microscopic model of electric-field-noise heating in ion traps". In: *Physical Review A* 84.2 (Aug. 2011), p. 023412. ISSN: 1050-2947. DOI: 10.1103/PhysRevA.84.023412.

[61] Philipp Schindler et al. "A quantum information processor with trapped ions". In: *New Journal of Physics* 15 (2013). ISSN: 13672630. DOI: 10.1088/1367-2630/15/12/123012. arXiv: 1308.3096.

[62] Philipp Schindler et al. "Polarization of electric-field noise near metallic surfaces". In: *Physical Review A* 92.1 (2015), p. 13414. ISSN: 1050-2947. DOI: 10.1103/PhysRevA.92.013414.

[63] Kilian Singer et al. "¡i¿Colloquium¡/i¿ : Trapped ions as quantum bits: Essential numerical tools". In: *Reviews of Modern Physics* 82.3 (Sept. 2010), pp. 2609–2632. ISSN: 0034-6861. DOI: 10.1103/RevModPhys.82.2609.

[64] J. D. Siverns et al. "On the application of radio frequency voltages to ion traps via helical resonators". In: *Applied Physics B: Lasers and Optics* 107.4 (2012), pp. 921–934. ISSN: 09462171. DOI: 10.1007/s00340-011-4837-0. arXiv: 1106.5013.

[65] A Sørensen and K Mølmer. "Quantum Computation with Ions in Thermal Motion". In: *Phys. Rev. Lett.* 82 (1999), p. 1971. DOI: 10.1103/PhysRevLett.82.1971.

[66] Rogerio de Sousa. "Electron Spin as a Spectrometer of Nuclear-Spin Noise and Other Fluctuations". In: Springer Berlin Heidelberg, 2009, pp. 183–220. DOI: 10.1007/978-3-540-79365-6_10.

[67] I. Talukdar et al. "Implications of surface noise for the motional coherence of trapped ions". In: *Physical Review A* 93.4 (Apr. 2016), p. 043415. ISSN: 2469-9926. DOI: 10.1103/PhysRevA.93.043415.

[68] Matthias Troyer and Uwe-Jens Wiese. "Computational Complexity and Fundamental Limitations to Fermionic Quantum Monte Carlo Simulations". In: *Physical Review Letters* 94.17 (2005), p. 170201. ISSN: 0031-9007. DOI: 10.1103/PhysRevLett.94.170201.

[69]   Q A Turchette et al. "Heating of trapped ions from the quantum ground state". In: *Physical Review A* 61 (2000), p. 63418. DOI: 10.1103/PhysRevA.61.063418.

[70]   J. Wesenberg. "Electrostatics of surface-electrode ion traps". In: *Physical Review A* 78.6 (Dec. 2008), pp. 1–12. ISSN: 1050-2947. DOI: 10.1103/PhysRevA.78.063410.

[71]   David M. Wilkins and Nikesh S. Dattani. "Why Quantum Coherence Is Not Important in the Fenna-Matthews-Olsen-Complex". In: *Journal of Chemical Theory and Computation* 11.7 (July 2015), pp. 3411–3419. ISSN: 1549-9618. DOI: 10.1021/ct501066k.

[72]   D J Wineland and H G Dehmelt. "Principles of the stored ion calorimeter". In: *J. App. Phys.* 46 (1975), p. 919.

[73]   D J Wineland et al. "Experimental Issues in Coherent Quantum-State Manipulation of Trapped Atomic Ions". In: *Journal of Research of the National Institute for Standards and Technology* 103 (1998), pp. 259–328.